

Exploring the Limits of Boiling and Evaporative Heat Transfer Using Micro/Nano Structures

by

Ming-Chang Lu

A dissertation submitted in partial satisfaction of the

requirements for the degree of

Doctor of Philosophy

in

Engineering-Mechanical Engineering

in the

Graduate Division

of the

University of California, Berkeley

Committee in charge:

Professor Van P. Carey, Chair

Professor Liwei Lin

Professor Joel Moore

Fall 2010

Exploring the Limits of Boiling and Evaporative Heat Transfer
Using Micro/Nano Structures

Copyright 2010

by

Ming-Chang Lu

Abstract

Exploring the Limits of Boiling and Evaporative Heat Transfer Using Micro/Nano Structures

by

Ming-Chang Lu

Doctor of Philosophy in Engineering – Mechanical Engineering

University of California, Berkeley

Professor Van P. Carey, Chair

This dissertation presents a study exploring the limits of phase-change heat transfer with the aim of enhancing critical heat flux (CHF) in pool boiling and enhancing thermal conductance in heat pipes. The state-of-the-art values of the CHF in pool boiling and the thermal conductance in heat pipes are about two orders of magnitudes smaller than the limits predicted by kinetic theory. Consequently, there seems to be plenty of room for improvement.

Pool boiling refers to boiling at a surface immersed in an extensive motionless pool of liquid. Its process includes heterogeneous nucleation, growth, mergence and detachment of vapor bubbles on a heating surface. It is generally agreed that the high heat transfer coefficient of boiling could be explained by the concept of single-phase forced convection, i.e., the motion of bubbles agitating surrounding liquid is similar to the process in single-phase forced convection. The occurrence of CHF results from a formation of a vapor film on the heater surface, which reduces the thermal conductance drastically and causes a huge temperature rise on the surface. Over the past few decades, researchers were struggling to identify the exact mechanism causing CHF. General observations are that both surface properties and pool hydrodynamics could affect the values of CHF.

Nanowire array-coated surfaces having a large capillary force are employed to enhance the CHF. It has been shown that CHF on the nanowire array-coated surface could be doubled compared to the values on a plain surface. The obtained CHF of $224 \pm 6.60 \text{ W/cm}^2$ on the nanowire-array coated surface is one of the highest values reported in the boiling heat transfer. To further enhance CHF, the mechanisms that govern CHF have been systematically explored. Experimental results show that the CHF on the nanowire array-coated surface are not limited by the capillary force. Instead, the CHF are dependent on the heater size. Corresponding experiments on plain surfaces with various heater sizes also exhibits similar heater-size dependence. The CHF on nanowire array-coated surfaces and plain surfaces are consistent with the predictions of the hydrodynamic theory while a higher CHF is obtained on the nanowire array-coated surface as compared to the plain Si surface. This suggests that the CHF are a result of the pool hydrodynamics while surface properties modify the corresponding hydrodynamic limits.

A heat pipe is a device that transports thermal energy in a very small temperature difference and thereby producing a very large thermal conductance. It relies on evaporation of liquid at the heated end of the pipe, flow of vapor between the heated and cooled end, condensation at the other end, and capillary-driven liquid flow through a porous wick between the condenser and the evaporation. The large latent heat involved in evaporation and condensation leads to very large heat flows for a small temperature drop along the heat pipe. Despite the large thermal conductance, their operation is limited by such factors as capillary limit, boiling limit, sonic limit and entrainment limit, etc. Among these operational limits, capillary and boiling limits are most frequently encountered. The capillary limit determines the maximum flow rate provided by the capillary force of the wick structure whereas boiling limit is referred to a condition that liquid supply is blocked by vapor bubbles in the wick. Consequently, the wick structure is the key component in a heat pipe, which determines the maximum capillary force and the dominant thermal resistance. In a heat pipe using evaporation as the dominant heat transfer mechanism, a thin liquid film (\sim a few microns) extended from the solid structure in the wick causes the dominant thermal resistance. Therefore, if one reduces the pore size of a porous media, the thermal conductance could be enhanced by increasing the surface area of the thin liquid film. On the other hand, the classical thermodynamics depicts that the superheat required for evaporation is inversely proportional to the equilibrium radius of the meniscus. Consequently, enhancing thermal conductance via increasing the thin film area is contradictory to the effect of evaporation suppression for small pores.

A hierarchical wick structure with multiple length scales that enhances dry-out heat flux and thermal conductance simultaneously in heat pipes was demonstrated. This hierarchical wick structure is composed of a large microchannel array to reduce flow resistance and small pin-fin arrays to provide a large capillary force. The enhancement of thermal conductance is achieved via a large number of pin-fins for increasing the total thin film area. A thermal conductance defined by the slope of the curve of $\sim 16.28 \pm 1.33 \text{ W/cm}^2\text{K}$ and a dry-out heat flux of $228.85 \pm 10.73 \text{ W/cm}^2$ were achieved by this design. Further, vapor transport resistance is minimized within the aligned-multi-scale wick structure. As a result, this wick does not pose a boiling limit. Artificial cavities were created in the wick structure to take the advantage of the high heat transfer coefficient of boiling heat transfer. The wick with artificial cavities successfully triggers boiling at a lower wall temperature resulting in a conductance of $9.02 \pm 0.04 \text{ W/cm}^2\text{K}$ compared to an evaporation mode of $3.54 \pm 0.01 \text{ W/cm}^2\text{K}$. For a given heat flux, the wick with cavities effectively reduce wall temperature compared to a wick without cavities. Our experimental results display an enhancement of thermal conductance by using boiling heat transfer. This opens up a new direction for further enhancing thermal conductance in heat pipes by circumventing the limit in the evaporative heat transfer regime, in which further increase in surface area will eventually result in evaporation suppression in small pores.

Table of Contents

Table of Contents	i
List of Figures	iii
List of Tables	vii
List of Tables	vii
Acknowledgements	viii
Acknowledgements	viii
Nomenclature	xi
Chapter 1 Introduction	1
1.1 Pool boiling	1
1.2 Heat Pipe	4
1.3 Organization of the Thesis	7
Chapter 2 Fundamentals of Pool Boiling	8
2.1 Homogeneous Nucleation	8
2.1.1 Maximum Superheat (Spinodal Point)	10
2.1.2 Stability at Equilibrium	12
2.2 Heterogeneous Nucleation	14
2.2.1 Active Cavity Sizes	15
2.3 Heat Transfer Coefficient of Pool Boiling	17
2.3.1 Rohsenow's Model	18
2.3.2 Microconvection Model	20
2.3.3 Vapor-Liquid Exchange Model	21
2.3.4 Comparison of Various Models	22
2.4 Summary	23
Chapter 3 Fundamentals of Heat Pipes	25
3.1 Operation Limits	25
3.1.1 Capillary Limit	25
3.1.2 Boiling Limit	27
3.1.3 Sonic Limit	28
3.1.4 Entrainment Limit	28
3.2 Thermal Resistances in Heat Pipes	29
3.3 Summary	32
Chapter 4 Enhancing Critical Heat Flux in Pool Boiling	34
4.1 Introduction	34

4.1.1	Far-field CHF Mechanism	34
4.1.2	Near-field CHF Mechanisms	35
4.1.3	Heater Size Effect	38
4.2	Nanowires for Enhancing Boiling Heat Transfer	39
4.2.1	Experimental Approach	39
4.2.2	Test Section and Experimental Setup	42
4.2.3	Results and Discussion	44
4.3	CHF Mechanisms on Si Nanowire Array-coated and Plain Si Surfaces	47
4.3.1	Test Section.....	47
4.3.2	Results and Discussion	48
4.4	Conclusion	53
Chapter 5	Enhancing Thermal Conductance in Heat Pipes.....	55
5.1	Introduction.....	55
5.2	Experimental Approach	62
5.3	Experimental Setup.....	64
5.4	Results and Discussion	66
5.5	Conclusion	72
Chapter 6	Conclusion and Future Work	74
6.1	Conclusion	74
6.2	Future Work.....	74
6.2.1	Enhancing Thermal Conductance in Heat Pipes.....	74
6.2.2	Verify the Hydrodynamic Theory.....	77
6.2.3	Comparison of Pool Boiling and Thin Film Boiling	79
References	80
Appendix: Heat Loss Estimate for the Evaporation Experiment.....		87
Appendix: Uncertainty Analysis.....		87
Uncertainty in Heat Flux Measurement.....		88
Uncertainty in Temperature Measurement		88
Uncertainty in the Heat Transfer Coefficients of Pool Boiling		89
Uncertainty in the Thermal Conductances of Evaporative Heat Transfer.....		89

List of Figures

Fig. 1.1 A representative boiling curve qualitatively showing heat flux versus wall superheat $T_w - T_{sat}$ (after [15]).....	2
Fig. 1.2 Power density trend predicted by ITRS 2008 [42].....	4
Fig. 1.3 A schematic of a thermal architecture consisting of a substrate, a DIE, a thermal interface material (TIM), a heat pipe/vapor chamber and a heat sink	5
Fig. 1.4 A Schematic of a Heat Pipe.....	5
Fig. 2.1 Formation of a vapor bubble inside a liquid pool (a) initial state (b) equilibrium state (after [16])	9
Fig. 2.2 A P - v diagram including the metastable regions, spinodal lines and an isotherm with a temperature smaller than the critical temperature (after [16])	10
Fig. 2.3 Chemical potential versus pressure along an isotherm (after [16]).....	12
Fig. 2.4 Variation of the change of system Gibbs free energy with bubble radius for a vapor bubble spontaneously formed in a superheated liquid (after [16])	14
Fig. 2.5 A schematic of heterogeneous nucleation	14
Fig. 2.6 A schematic of vapor bubble formation at the cavity on a heating surface.....	15
Fig. 2.7 The temperature profile inside the thermal boundary layer where the dark straight line is the steady state solution of Eq. (2.30) and the pink solid curve is the superheat required as a function of distance from Eq. (2.35).....	16
Fig. 2.8 Activated cavity size versus wall superheat for water at one atmosphere, The blue and red curves are minimum and maximum sizes of active cavities at a given wall superheat, respectively.	17
Fig. 2.9 The convective heat transfer induced by departing vapor bubbles	18
Fig. 2.10 Comparison of various heat transfer coefficient models in pool boiling	23
Fig. 3.1 Three commonly used commercially available wick structures.....	25
Fig. 3.2 A schematic showing meniscus profiles at the evaporator and condenser sections.....	26
Fig. 3.3 A schematic of the boiling Limit of heat pipe operation.....	27
Fig. 3.4 (a) a schematic of a heat pipe and (b) its corresponding thermal resistance network	29
Fig. 3.5 Mass flux at a liquid-vapor interface.....	30

Fig. 4.1 A schematic of the macrolayer	36
Fig. 4.2 Copper nanowire synthesis and bonding: (a) alumina membrane used as the template for Cu nanowire electroplating, (b) Cu deposition by sputtering on the backside of the membrane, (c) Thickening the backside Cu by electroplating, (d) Cu electroplating through the front side of the membrane to form nanowires, (e) Bonding the membrane onto a Si substrate, (f) Removing alumina by etching in NaOH.	40
Fig. 4.3 Scanning Electron Microscopy (SEM) graphs of: (a) top view of Cu Nanowires; (b) Cross-section of Cu Nanowires (c) top view of Si Nanowires; (d) Cross-section of Si Nanowires	41
Fig. 4.4 Si nanowire synthesis (a) a redox reaction happens on the surface of Si substrate where Si is oxidized to SiO ₂ and Ag ⁺ is reduced to Ag, (b) HF solution continuous etches the SiO ₂ area surrounding by the Ag particles-deposited sites and a dendrite structure of Ag formed on the surface, (c) the dendrite structure is removed by HNO ₃ solution and a free standing Si nanowire array forms on the surface.	41
Fig. 4.5 A schematic consisting of ITO heater, two Cu electrodes and thermocouples (TCs).....	42
Fig. 4.6 A schematic of the boiling experimental setup, including the test sample, PDMS and Teflon thermal insulators, data acquisition and visualization systems.	44
Fig. 4.7 boiling curves for Plain Si surface, Si nanowires and Cu nanowires	44
Fig. 4.8 Bubble images: (a) Si Nanowires: 18 W/cm ² (b) Si Nanowires: 177 W/cm ² (c) Si: 20 W/cm ² (d) Si: 93 W/cm ²	45
Fig. 4.9 Static contact angles of a water droplet on surfaces of Si, SiO ₂ , and Si and Cu nanowires.	46
Fig. 4.10 Dependence of CHF on contact angle. CHF of plain Si (blue triangle) and SiO ₂ (blue rectangle) observed in the present study follows the theoretical models given by Dhir and Liaw [20] (red solid line) and Zuber [17] (red dashed line) and experimental data of Dhir and Liaw [20] (black circles). However, CHF for Cu and Si nanowires (blue and red circles, respectively) are significantly higher than the theoretical prediction, indicating mechanism besides contact angle dependence is also involved.....	46
Fig. 4.11 Schematics of (a) original test section and (b) modified test section for minimizing thermal spreading.....	48
Fig. 4.12 SEM images of a SiNW array with different heights: (a) 16 μm (b) 32 μm (c) 59 μm (d) 122 μm.....	48
Fig. 4.13 Boiling curves on SiNW array-coated surfaces for different heights of NWs	49
Fig. 4.14 Boiling curves on SiNW array coated-surfaces for different sizes of the heaters.....	50

Fig. 4.15 Boiling images at CHF condition for different sizes of heaters (a) 0.5 x 0.5 cm ² (b) 1 x 1 cm ² (c) 1.5 x 1.5 cm ² and (d) 2 x 2 cm ² . Note that the edges of heaters are outlined.	51
Fig. 4.16 CHF versus heater length where the red open triangle marks are experiment results of SiNW array-coated surfaces of four different sizes of heaters and the red solid curve is the theoretical prediction of Eq. (4.1) using the Helmholtz wavelength as a control variable assuming an area ratio (A_v/A) of 0.15 and the dark cross points and are the results of plain Si surface and the dark solid curve is the theoretical prediction of Eq. (4.1) assuming an area ratio (A_v/A) of 0.0055.	51
Fig. 4.17 Boiling curves on plain Si surfaces for different sizes of heaters	52
Fig. 5.1 SEM image of cross-section of the evaporator geometry, showing array of pin-fins with periodic microchannels.	56
Fig. 5.2 (a) The micro pin-fin wick structure and (b) its corresponding resistance network.....	57
Fig. 5.3 A schematic of a thin liquid film near a wall	58
Fig. 5.4 The meniscus at the interline region.....	59
Fig. 5.5 Superheat versus pore size according to Eq. (5.15) for water at one atmosphere under saturation condition with $A_c = 2 \times 10^{-6} \text{ m}^2$, $l = 1 \text{ cm}$, $\phi = 0.75$	60
Fig. 5.6 The extended meniscus on a flat surface.....	61
Fig. 5.7 Variation of contact angles corresponds to two different heat loads.....	62
Fig. 5.8 Confinement of the apparent contact angle by the walls of micro pin-fins.....	62
Fig. 5.9 Sketch of fabrication process used to generate the wick with microchannels and micro pin fins.....	63
Fig. 5.10 A schematic of fabrication process used to generate a wick with pin fins and cavities	64
Fig. 5.11 Comparison of a wick having cavities and pin fins (a) top view (b) cross-sectional view, and a wick with only pin fins (c) top view (d) cross-sectional view.....	64
Fig. 5.12 Experimental apparatus used to measure evaporative heat transfer	65
Fig. 5.13 Repeatability of data for two samples for $d = 16 \text{ }\mu\text{m}$, $H = 150 \text{ }\mu\text{m}$, $L_{wicking} = 0.5 \text{ cm}$. ..	67
Fig. 5.14 Variation of dryout flux as a result of increase in wicking height ($d = 16 \text{ }\mu\text{m}$, $H = 150 \text{ }\mu\text{m}$).	68
Fig. 5.15 Comparison of performance of evaporator geometries of different microchannel depths ($d = 8 \text{ }\mu\text{m}$, $L_{wicking} = 0.5 \text{ cm}$).	69

Fig. 5.16 Effect of pore size on evaporation curves ($H = 150 \mu\text{m}$, $L_{wicking} = 0.5 \text{ cm}$).....	70
Fig. 5.17 Comparison of (a) evaporative and (b) boiling heat transfer in a micro pin fin array wick.....	72
Fig. 5.18 Experimental results of a wick with pin-fins along (blue solid circle) and a wick with pin-fins and cavities (red solid triangle).....	72
Fig. 6.1 A schematic of a wick with re-entrant cavities.....	76
Fig. 6.2 Fabrication procedure for a re-entrant cavity array wick	76
Fig. 6.3 Preliminary result of the fabrication of a re-entrant cavity array wick	77
Fig. 6.4 Microwire array with different patch sizes.....	78
Fig. 6.5 CHF vs. heater size on microwire, nanowire and plain Si surfaces	78
Fig. 6.6 A schematic comparing (a) pool boiling versus (b) thin film boiling	79

List of Tables

Table 2.1 Values of C_{sf} in Eq. (2.42) from [56-60].....	19
Table 3.1 Typical orders of magnitudes of thermal resistances in a heat pipe	32
Table 4.1 Summary of Experimental Results	53
Table 5.1 Various dimensions defining the wick geometry	66
Table 5.2 Performance of evaporator geometries as a function of pore size (for $H = 150 \mu\text{m}$, $L_{wicking} = 0.5\text{cm}$)	70
Table A.1 Conduction Loss of the Evaporation Experiment.....	87

Acknowledgements

I am most grateful to Yu-Ting, who takes care of Yaoan and my father when I am absent. The time that we are able to stay together is always so short. I cherish the moment that we are together. With your support and love, I can overcome all the challenges along the way to my PhD degree. Thank you, Yu-Ting. I love you.

My father always worries about me. I was never a good student before serving in the army but he never gave up of me. When I think now he will be proud of me, he is not even able to get up from a bed. My mother always loves me. Sometimes she just calls me randomly to make sure that I am fine being alone abroad. She takes care of the business and the whole family since my father was sick. I always think that she is so great for handling all these things together especially when all the children are abroad. My sisters take care of our father and shear my responsibility at home when I am studying abroad. It is this endless support and love from my family makes it possible for me to finish my graduate school. I would like to express my sincere gratitude to my family.

At Berkeley, I am very fortunate to work with a group of smart and brilliant people. Without their support, encouragement and help, I will never be able to finish this dissertation. I would like to acknowledge all of them.

First of all, I would like to thank Dr. Arun Majumdar. Arun made it possible for me to study and work in his group. Arun gives me a great freedom to pursue my intellectual goal. Without his encouragement and advises, it will not be possible for me to achieve my goal. His deep insight and wide vision really open my mind in doing research. The thing that I have learnt from him will be with me along my academic career in the future. Arun is truly a wonderful advisor and I consider myself very fortunate to be one of his students.

I would also like to thank Dr. Renkun Chen and Dr. Vinod Srinivasan who were my collaborators, coworkers and mentors. Renkun taught me a lot about fabrication when I started to work on the HATS project. Vinod and I work together for a long time and I have learnt a lot from him about the experimental and analytical techniques. Without all the spirited discussions that I had with Renkun and Vinod, it would not have been possible to make progress with our experiments. I would also like to thank my other coworkers Dusan Coso in the HATS project and Dr. Baoling Huang and Kedar Hippalgaonkar in the nanowire project.

I also want to express my heartfelt thanks to Prof. Van P. Carey, for valuable discussions and insightful advices on the phase change heat transfer and his service as my qualify exam and dissertation committee, especially for his generosity for willing to sever as my advisor after Arun resigned. I also want to thank Prof. Liwei Lin and Prof. Joel Moore for their valuable comments on my research work and for their service in my qualify exam and dissertation committee. I would also like to thank Dr. Ravi Prasher and Dr. Je-Young Chang for the frequent and valuable discussions on the HATS project supported by Intel.

I would also like to give a special thank to Dr. Chuanhua Duan for all the supports he gave me in Berkeley and all I have learnt from him about fabrication techniques in general. I would like to

thank all other lab members for the accompany in Berkeley- Yang Zhao, Donyan Xu, Yusra Satoglu, Joe Feser, Chris Zueger, Jayakanth Ravichandran, Rong-Shiuan Chu, Shannon Yee and Cheng Zheng.

Finally, I would like to thank the Microlab where I spent a lot of time fabricating devices. I also would to like to thank all the funding sources- Industrial Technology Research Institute from Taiwan, Intel, National Science Foundation and UC Discovery Program for supporting my research work at Berkeley.

Dedicated
to
Yu-Ting Liu and Yaoan Lu
and
To my parents and sisters for their love and support

Nomenclature

a	Van der Wall constant
A	Heater area
A^*	$=0.1011 P_c^{0.69}$
A_c	Cross-sectional area
A_v	Area covered by vapor
A_w	Wick area
b	Van der Wall constant
B	A constant used in Nusselt number in the convection model
c	Sound velocity
C_1	A constant used in Stephan and Abdelsalam' model
C_2	A constant used in Stephan and Abdelsalam' model
C_3	A constant used in Stephan and Abdelsalam' model
C_4	A constant used in Stephan and Abdelsalam' model
C_b	A constant used in Rohsenow's model
C_p	Specific heat
C_{pl}	Specific heat of liquid
C_{sf}	A constant used in Rohsenow's model
d	Pore size and pin size in a micro pin-fin wick
d	Characteristic length scale in a wick
d_d	Bubble departure diameter
D	Width of the microchannel
D_i	Heat pipe inner diameter
D_o	Heat pipe outer diameter
D_v	Vapor core diameter
e	Effusivity
f	Frequency
g	Gravity
\hat{g}_l	Molar specific Gibbs free energy of liquid
\hat{g}_v	Molar specific Gibbs free energy of vapor
G	Gibbs free energy
G_0	Gibbs free energy at initial condition
ΔG	Change of Gibbs free energy
ΔG_e	Change of Gibbs free energy at equilibrium condition
h	Thermal conductance
h_i	Interfacial thermal conductance
h_{lv}	Latent heat of vaporization
H	Wick height
Ja	Jacob number
K	Proportional constant in the hydrodynamic theory of the CHF model
k	Thermal conductivity
k_B	Boltzmann's constant
k_l	Thermal conductivity of liquid
k_s	Thermal conductivity of solid structure

k_{wall}	Thermal conductivity of heat pipe wall
k_{wick}	Thermal conductivity of a wick
l	Liquid flow distance
L'	Non-dimensional heater length
L	Heater length
L	Width of pin-fin array
L_{film}	Extension of a thin liquid film near the solid wall
L_{eff}	Effective length of vapor flow in a heat pipe
L_b	Length scale of vapor bubble used to calculate heat transfer coefficient
L_c	Capillary length
L_a	Length of the adiabatic section in a heat pipe
L_e	Length of the evaporator section in a heat pipe
L_c	Length of the condenser section in a heat pipe
$L_{wicking}$	Wicking height
\dot{m}_l	Liquid mass flow rate
m_v''	Vapor mass flux
m_l''	Liquid mass flux
m_i''	Interfacial mass flux
\bar{M}	Molecular mass
n	Number density
n_a	Nucleation site density
\hat{N}_v	Number of moles of vapor molecules
N	Number of pins
N_j	Number of vapor columns on a heater
Nu_b	Nusselt number of a vapor bubble
P	Pressure
P_1	Pressure at the vapor side at the evaporator section in a heat pipe
P_2	Pressure at the vapor side at the condenser section in a heat pipe
P_3	Pressure at the liquid side at the condenser section in a heat pipe
P_4	Pressure at the liquid side at the evaporator section in a heat pipe
P_A	Pressure at point A
P_c	Capillary pressure
P_c	Critical pressure
P_d	Disjoining pressure
P_l	Liquid pressure
P_r	Reduced pressure
P_{ve}	Equilibrium vapor pressure
P_v	Vapor pressure
P_{sat}	Saturation pressure
Pr_l	Prandtl number of liquid
ΔP	Pressure difference
ΔP_c	Difference in capillary pressure
q_s	Heat transfer rate per nucleation site

q''	Heat flux
q_i''	Interfacial heat flux
q_{CHF}	Critical heat flux
$q_{CHF,max}$	Critical heat flux without heater size effect
$q_{CHF,Z}$	Critical heat flux predicted by Zuber
q_{cond}	Heat spread by conduction through substrate
Q_{max}	Maximum heat transfer rate
Q	Applied power
r_c	Critical radius of curvature
r_c	Month radius of surface cavities
$r_{c,min}$	Minimum activated month radius of cavities
$r_{c,max}$	Maximum activated month radius of cavities
r_e	equilibrium radius
r_v	Vapor core radius
R	Gas constant
R	Radius of a vapor column/bubble
\dot{R}	Bubble interface velocity
\bar{R}	Universal gas constant
R_c	Constant in the convection model
R_i	Interfacial thermal resistance
R_{film}	Thin film thermal resistance
R_{max}	Maximum radius of a vapor bubble in the convection model
R_s	Solid structure thermal resistance
R_{vc}	Thermal resistance in the vapor-core region
R_{wall}	Thermal resistance of heat pipe wall
R_{wick}	Wick thermal resistance
Re_b	Reynold's number of a vapor bubble
Re_v	Reynold's number of vapor flow
s	mass specific entropy
S	Equals to heater thickness times the effusivity
t	time
T	Temperature
T_c	Critical Temperature
T_{edge}	Temperature at the edge of the heater
T_l	Liquid temperature
T_{le}	Equilibrium liquid temperature
T_r	Reduced temperature
T_{ref}	Temperature at the point 2 mm away from the heater edge
T_{sat}	Saturation temperature
T_v	Vapor temperature
T_w	Wall temperature
ΔT	Temperature difference
u_{av}	Average vapor velocity
u_b	Bubble velocity
u_c	Critical velocity
u_v	Vapor velocity

v	Mass specific volume
v_c	Specific volume at critical condition
v_l	Mass specific volume of liquid
v_{lv}	Difference of the mass specific volume between liquid and vapor
v_r	Reduced volume
\hat{v}_v	Molar specific volume of vapor
W	Channel width
We	Weber's number
x	Distance away from the heater edge (equals to 2 mm)
y	Coordinate in the thermal boundary layer in heterogeneous nucleation

Greek

α	Accommodation coefficient
α	Thermal diffusivity
α_l	Thermal diffusivity of liquid
δ	Heater thickness
δ	Film thickness
δ_C	Macrolayer thickness
δ_t	Thermal boundary layer thickness
θ	Contact angle
θ	$T - T_{\text{sat}}$
θ_a	Apparent contact angle
θ_μ	Microscopic contact angle
κ	Porous media permeability
λ_C	Critical Taylor wavelength
λ_D	Most dangerous Taylor wavelength
λ_H	Helmholtz wavelength
μ	Chemical potential
μ_A	Chemical potential at point A
μ_v	Chemical potential of vapor
$\mu_{\text{sat},v}$	Chemical potential of vapor at saturation condition
μ_l	Chemical potential of liquid
$\mu_{\text{sat},l}$	Chemical potential of liquid at saturation condition
μ	Dynamic viscosity
μ_v	Dynamic viscosity of vapor
μ_l	Dynamic viscosity of liquid
ρ	Density
ρ_b	Density of a vapor bubble
ρ_l	Liquid density
ρ_v	Vapor density
σ	Surface tension of liquid
σ_i	Interfacial Surface tension
τ_d	Hovering time of the vapor mushroom
ϕ	Porosity

Ω Angle relative to horizontal

Subscript

b Bubble
CHF Critical heat flux
CHF,max Critical heat flux without heater effect
CHF,Z Critical heat flux proposed by Zuber's model
i Interface
l Liquid
v Vapor
sat Saturation condition
w Wall

Superscript

[^] Molar specific
· First order derivative

Chapter 1 Introduction

The current demand of the world's total power is about 13 Terra-Watt (TW) and is expected to reach 30 TW by 2050 [1]. Thermal energy plays a primary role in the world's total energy: More than 90 % of world's total power is generated by heat engines. Phase change heat transfer is the dominant component of thermal transport. The large change in enthalpy, entropy and volume in phase change allowing a great amount of energy transferred within a small difference of temperature enables an efficient thermal energy conversion. It has applications in many fields including power plants [2, 3], air conditioning and refrigeration and compact heat exchangers [4], chemical processes [5] and electronic cooling [6-13] comprising heat pipes [9-13] in particular, etc. Enhancing phase change heat transfer would improve the efficiency of thermal energy transport and conversion in these processes; thereby increases the overall energy efficiency. Among these fields, I am mainly working on enhancing performances in the boiling heat transfer and heat pipes. While the state-of-the-art values of the maximum heat flux and the maximum thermal conductance of about 100 W/cm^2 and $10 \text{ W/cm}^2\text{K}$, respectively, they are not physical limits. The physical limits of the maximum heat flux and the maximum thermal conductance of a phase-change process are depicted by kinetic theory. The maximum heat flux according to kinetic theory is equal to sound velocity (c) multiplied by density (ρ_v) and latent heat (h_{lv}), i.e., $q'' = c\rho_v h_{lv}$, which is on the order of 10^4 W/cm^2 for water under saturation condition at one atmosphere. A more rigorous analysis developed by Schrage [14] suggests a proportionality constant of 0.741 placed in front of the right side of the above equation, accounting for the fact of non-equilibrium condition associated with net mass flux. For water at atmospheric pressure, q_{\max} is calculated to be $1.65 \times 10^4 \text{ W/cm}^2$ according to Schrage's analysis [14]. Meanwhile, the maximum thermal conductance depicted by kinetic theory is the interfacial thermal conductance between liquid and vapor with a perfect accommodation, which results in $h \sim 1500 \text{ W/cm}^2\text{K}$ for water at one atmosphere. Consequently, there is plenty of room for improving phase change heat transfer.

1.1 Pool boiling

Boiling is widely used as a liquid-vapor phase transition mechanism in the industry and is also a common phenomenon observed in our daily lives. [15, 16] Boiling involves heterogeneous nucleation and growth of vapor bubbles on a heated surface and subsequent departure of these bubbles from the heated surface. Pool boiling refers to boiling under natural convection conditions, where the heating surface is submerged in a large body of stagnant liquid and the relative motion of vapor bubble and its surrounding liquid is primarily due to the buoyancy effect of the vapor [15, 16].

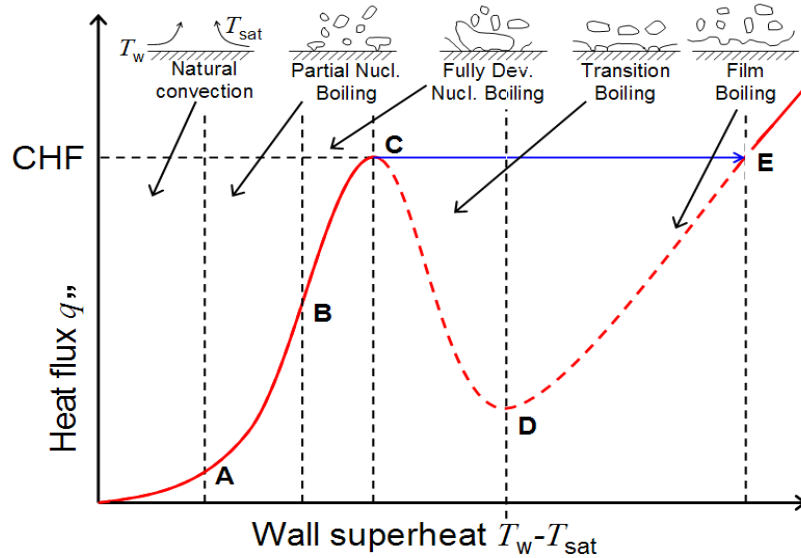


Fig. 1.1 A representative boiling curve qualitatively showing heat flux versus wall superheat $T_w - T_{sat}$ (after [15]).

Fig. 1.1 qualitatively shows the boiling curve, i.e., the dependence of heat flux, q'' , on wall superheat, $\Delta T = T_w - T_{sat}$, the temperature difference between the heated surface and the saturation temperature of the liquid (e.g., for water under atmospheric pressure, $T_{sat} = 100\text{ }^\circ\text{C}$). Up to the point A, heat transfer is dominant by natural convection and no bubbles are formed. Point A denotes the onset of nucleate boiling whereby vapor bubbles are nucleated at the heated surface. Heat transfer starts to be dominated by partial nucleate boiling (curve A-B), where the wall superheat is sufficiently high to activate discrete bubbles. Beyond point B, nucleate boiling becomes fully developed (curve B-C) as bubbles begin to merge to form columns. At point C, the heat flux reaches its maximum value usually referred to as critical heat flux (CHF). At this point, the bubbles are large enough to merge and form a continuous vapor film between the liquid and the heated surface. Due to lower thermal conductivity of the vapor compared to the liquid, the thermal resistance increases sharply due to the presence of the vapor film, leading to a large increase in wall superheat from about 20 K at point C to about 1000 K at point E. The other important factor of the boiling heat transfer is the heat transfer coefficient (HTC) which is defined as the CHF divided by the corresponded superheat.

While more than 90 % of the world's total energy is generated by heat engines, 40 % of the heat engines are running through Rankine cycles. The CHF of boiling sets an upper limit for safe operation of the maximum power generation of these heat engines. Consequently, enhancing CHF will have a great impact on world's total energy. The current values of CHF of water at one atmosphere under saturation condition is about 100 W/cm^2 , which is far below the maximum limit predicted by kinetic theory of about 10^4 W/cm^2 . The most well known CHF mechanisms are based on the hydrodynamic theory, which depicts that the occurrence of CHF is due to the pool hydrodynamics. The models [17, 18] based on the hydrodynamic theory predict the value of CHF of about 100 W/cm^2 for water under saturation condition at one atmosphere. Although, these models can agree well with some of experimental results [19], they can not explain the experimentally observed surface properties dependence of CHF, for example, surface wettability

[20-27], surface capillarity [27-29], nucleation site density [30-34], thermal fin area on the heater surface [32-34], and substrate effusivity [35-37], etc. A recent comprehensive review of boiling enhancement has been given by Piro et al. [38]. The methods for boiling enhancement are summarized as follows:

One approach to enhance the CHF is to modify surface properties to increase surface wettability as suggested by the models proposed by Dhir and Liaw [20] and Kandlikar [39]. The experimental results of Dhir and Liaw [20] and Wang and Dhir [21] had showed that CHF increases as the contact angle reduces. Takata et al. [22] displayed an increase of CHF on a superhydrophilic surface of TiO₂ after ultraviolet (UV) light exposure compared to the TiO₂ surface without UV exposure. Recent studies using nanofluids to enhance boiling heat transfer also fall into this category [23-27]. It was demonstrated that the significant CHF enhancement is due to the nanoparticle deposition on the boiling surface, which causes enhanced surface wettability [23-27]. For example, You et al. [23] showed that the CHF of pool boiling with nanofluid was increased by nearly 200 % compared to that of pure water at a saturated temperature of 60 °C.

Another approach is to use a wicking structure to enhance the capillary force on the surface and delay the CHF. Kim et al. [27] has shown that a greater CHF is achieved for fully wetting surfaces with a larger capillary height where the height refers to the liquid column that can be sustained against gravity. Liter and Kaviany [28] employed a modulated porous-layer coating made of Cu micro-particles to study the mechanism of CHF enhancement. Li and Peterson [29] used highly conductive microporous coated surfaces made of Cu wire meshes to increase the capillary force, which results in a higher CHF. The above studies suggest that the capillary force plays a significant role in enhancing the CHF.

Another method is to increase the number of microscale cavities, which serves as the starting sites for heterogeneous nucleation of liquid for bubble formation. Chang and You [30] had shown an enhanced CHF on a surface coating with diamond particles. The sizes of the particles are in the range of a few to tens of microns. The enhancement of CHF is attributed to an increase of nucleation site density on the coating surface. Theofanous et al. [40] found that the CHF is directly related to the nucleation site density, i.e., a higher CHF is observed on a surface with a larger nucleation site density.

Honda and co-workers [32-34] had shown that using micro pin-fins to enhance the CHF. The enhancement is attributed to an increase of nucleation site density and an increase of heat transfer surface area by the thermal fin effect.

Li and Peterson [41] recently used a Cu nanorod array surface to enhance boiling heat transfer. These nano-rods are made of oblique angle deposition and have diameter of ~50 nm and length of ~0.5 μm. Boiling on the Cu nanorod array had been shown a 200 % increase in HTC compared to a plain Cu surface, while CHF remains about the same. The HTC enhancement can be explained by the increased nucleate site density due to the presence of the short Cu nano-rods, which can be viewed as an extremely rough surface.

In the past five decades, researches were struggling to find the exact mechanism causing CHF. General observations based on experiments are that pool hydrodynamics [19] and surface

properties [20-37] can both affect the values of CHF. The purpose of this study is to enhance the CHF and identify the mechanism of CHF.

1.2 Heat Pipe

Thermal management is one of the most critical issues in microelectronic devices. The continuing increase in functionality and power per unit area poses severe challenges in thermal management. The International Technology Roadmap of Semiconductors 2008 (ITRS 2008 [42]) shown in Fig. 1.2 indicates that the power density of semiconductors could be as high as 100 W/cm² after 2008. And this trend of increment levels off afterwards due to a transition from single-core to multi-core chips. Nevertheless, due to the complexity of today's chip designs, there are local hot-spots which might have local heat flux of 300 W/cm² [8] formed on a chip. Therefore, reducing of the impact of these hot-spots and diminishing the overall heat flux by spreading the heat to the heat spreader becomes crucial issues for thermal engineers. A heat pipe/vapor chamber (vapor chamber refers to a flat-plate heat pipe) having high effective thermal conductivity is an attractive candidate of the thermal spreaders because of its light weight and a comparable thermal resistance compared with copper block [7, 9, 43].

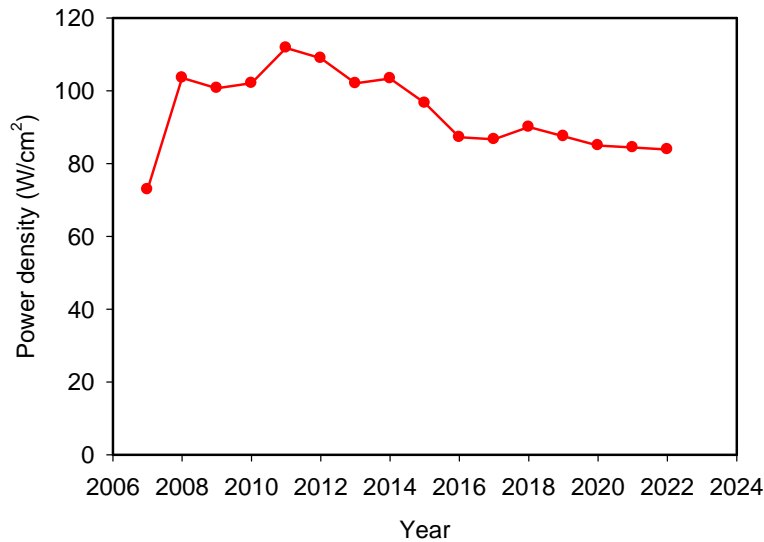


Fig. 1.2 Power density trend predicted by ITRS 2008 [42]

A schematic of a thermal architecture of the semiconductor electronics using a heat pipe as a thermal spreader is shown in Fig. 1.3. It consists of a substrate, a DIE, a thermal interface material (TIM), a heat pipe/vapor chamber and a heat sink. The temperature effect on the performance of the semiconductor electronics was illustrated by Kirschman [44]. In general, high temperature can cause malfunction of the semiconductor electronics due to the following reasons: (1) reliability: degradation caused by electron migration and thermal diffusion is thermally activated and depends exponentially on temperature. (2) thermal expansion mismatch:

Stress and strain built in the materials during the thermal cycles with a large temperature difference could cause serious thermal expansion mismatch.

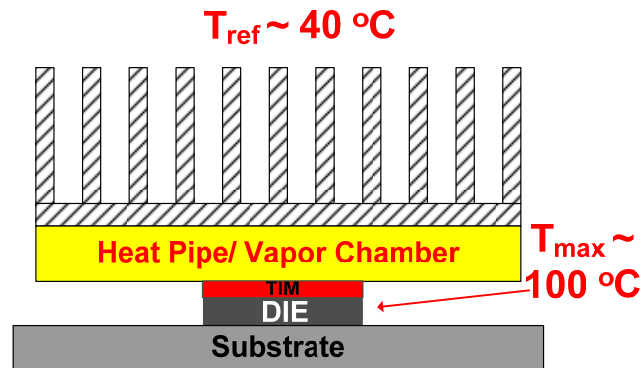


Fig. 1.3 A schematic of a thermal architecture consisting of a substrate, a DIE, a thermal interface material (TIM), a heat pipe/vapor chamber and a heat sink

Therefore, maintaining at a low acceptable operation temperature of these semiconductor electronics is necessary for appropriate functioning. Due to the relatively high reference temperature at the working environment ($\sim 40\text{ }^{\circ}\text{C}$) and the limiting maximum operation temperature ($\sim 100\text{ }^{\circ}\text{C}$) of these semiconductor electronics, not large temperature difference could be explored for heat pipes. As a result, the thermal conductance in heat pipes is a critical parameter.

A schematic of a heat pipe is shown in Fig. 1.4. The heat pipe can be divided into three regions: An evaporator section, an adiabatic section and a condenser section. The cross-section of the heat pipe consists of a container wall, a wick structure and a vapor-core region. Heat pipe is considered as a device having very high thermal conductance. This is mainly resulted from the large latent heat accompanied with the phase change process.

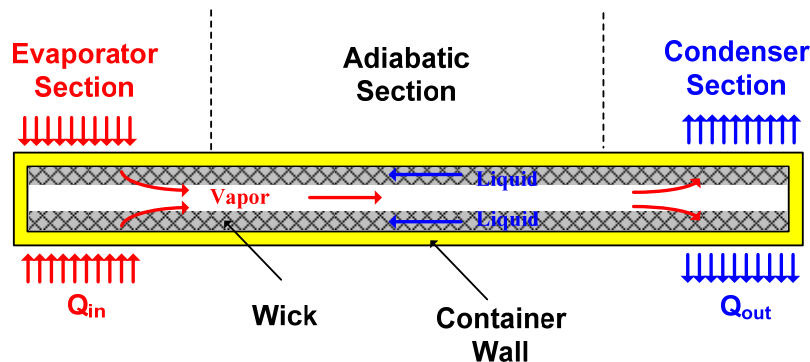


Fig. 1.4 A Schematic of a Heat Pipe

In operation, heat is applied at the evaporator section, heating liquid into vapor. The resultant high pressure at the evaporator section drives vapor flow to the condenser section. The latent heat of evaporation is carried and transferred by the vapor to the condenser section. The latent heat is dissipated into the environment at the condenser section and vapor is condensed into

liquid. The condensed liquid flows back to the evaporator section via the capillary pressure provided by the wick structure at the evaporator section. It is noted that the high thermal conductance of heat pipe is a result of large latent heat of liquid-vapor transition and only happens in the vapor-core region. In a heat pipe, the wick structure causes dominant thermal resistance. Consequently, the wick structure which determines the capillary force and dominant thermal resistance is the key component in a heat pipe.

In principle, a variety of morphologies (arteries, screens and sintered particles) can be used for the wick structure. Early work related to electronics cooling concentrated on microchannel arrays of triangular, square or trapezoidal cross-section [10]; however, thermal conductance for these geometries are typically low ($\sim 1 \text{ W/cm}^2\text{K}$). Gupta and Upadhyaya [13] analyzed wicks made of sintered metal particles, wrapped wire screens and square axial grooves with pore sizes in the range 100-200 μm and found the highest power dissipation for sintered particle wicks; conductance was not addressed. Wicks with sintered particles in the range 40-400 μm and typically of 1-4 mm thickness have been tested by several researchers [12, 45-50]. These wicks show thermal conductance in the range 1-10 $\text{W/cm}^2\text{K}$, depending on the particle size distribution and wick thickness. Thermal conductance is observed to increase as the applied power increases, reaching a peak near wick dry-out. The highest observed conductance using sintered particle wicks is 12.8 $\text{W/cm}^2\text{K}$ at an applied flux of 35 W/cm^2 [50] for a single sample; all other wicks in the literature using evaporation as the dominant heat transfer mechanism show values in the range 1-10 $\text{W/cm}^2\text{K}$.

Recently, several researchers [13, 45-47] have used bi-porous media, made of small particles forming large clusters and large pores, or particles with a bimodal size distribution, to enhance mass flux. The large pores formed due to particle clustering reduce the liquid flow drag, and increase maximum heat flux. While there is agreement on the resulting increase in mass flux, thermal conductance has been observed to increase by up to 100 % to about 10 $\text{W/cm}^2\text{K}$ in one instance [47] and by only 10 % in another [48]. Nucleate boiling is observed in some studies [46, 48, 50]; presumably the large pores formed due to non-uniform clustering of small particles reduce the superheat necessary for nucleate boiling. The effective conductivity of the wick appears to have no influence in this regime; Semenic et al. [48] observe similar conductance ($\sim 10 \text{ W/cm}^2\text{K}$) for wicks of conductivity 22.7 W/m-K (bi-porous) and 173 W/m-K (uni-porous). The boiling limit is reached when the escaping vapor blocks the liquid supply channels and causes dry-out, analogous to the CHF in pool boiling. While the majority of studies using bi-porous wicks report peak conductance of about 10 $\text{W/cm}^2\text{K}$, two studies using wicks of copper mesh [46] and sintered copper powder patterned into microchannels [50] report conductances of $\sim 25 \text{ W/cm}^2\text{K}$. While Li et al [46] attribute the enhancement to the wick thickness being less than the bubble departure diameter ($\sim 1 \text{ mm}$), Zhao and Chen [50] explain the enhancement in terms of improved vapor transport through the porous sidewalls of microchannels in their wick.

The available data display considerable variation in the value of thermal conductance, as well as particle size and wick thickness at which the best performance is achieved. The purpose of the study is to identify the dominate factors affecting the thermal conductance in a wick and thus enhances the thermal conductance in heat pipes.

1.3 Organization of the Thesis

In this thesis, I will present a study on exploring the limits of phase change heat transfer focusing on enhancing CHF in pool boiling and enhancing the thermal conductance in heat pipes. The organization of this thesis is as follows: In chapter 2, the fundamental concepts in pool boiling will be illustrated including: (1) homogeneous nucleation which describes a condition where bubble vapor formation happened in a liquid pool, (2) heterogeneous nucleation which is referred to as vapor bubble formed on surface cavities and (3) the heat transfer coefficient in pool boiling. In chapter 3, the background in heat pipes will be introduced. First, the operational limits of heat pipes will be illustrated. Second, the thermal resistances in a heat pipe will be analyzed. In chapter 4, I will present my approach to enhance CHF and explore the limit causing CHF. In chapter 5, I will present a detailed study on an evaporator wick of a heat pipe. Finally, conclusions and future work will be described in chapter 6.

Chapter 2 Fundamentals of Pool Boiling

To initiate boiling, nucleation of vapor bubbles in liquid is required. There are two kinds of nucleation: homogeneous nucleation and heterogeneous nucleation. Homogeneous nucleation is referred to as vapor bubble formation inside a liquid pool whereas heterogeneous nucleation is referred to as bubbles formed from the cavities on the heating surface immersed in a liquid pool.

2.1 Homogeneous Nucleation

For a vapor bubble formed inside a liquid pool as shown in Fig. 2.1, the equilibrium condition requires that the temperature of vapor must be equal to the temperature of liquid

$$T_v = T_l \quad (2.1)$$

and the chemical potentials of vapor (μ_v) and liquid (μ_l) must be the same

$$\mu_v = \mu_l \quad (2.2)$$

Further, the vapor pressure at equilibrium must be larger than the liquid pressure to accommodate the surface curvature

$$P_{ve} = P_l + \frac{2\sigma}{r_e} \quad (2.3)$$

where P_{ve} , P_l , σ , and r_e denote the equilibrium pressure of vapor, liquid pressure, surface tension of liquid and the equilibrium radius of the vapor bubble, respectively. Integrating the Gibbs-Duhem equation,

$$d\mu = -sdT + vdP \quad (2.4)$$

from a saturation state to an arbitrary equilibrium state, one obtains

$$\mu - \mu_{sat} = \int_{P_{sat}(T_l)}^P vdP \quad (2.5)$$

Using the ideal gas law ($v=RT_l/P$) for the vapor phase, one obtains

$$\mu_v = \mu_{sat,v} + RT_l \ln \left[\frac{P_{ve}}{P_{sat}(T_l)} \right] \quad (2.6)$$

where R is the gas constant. For the liquid phase, because it is nearly incompressible, one obtains

$$\mu_l = \mu_{sat,l} + v_l [P_l - P_{sat}(T_l)] \quad (2.7)$$

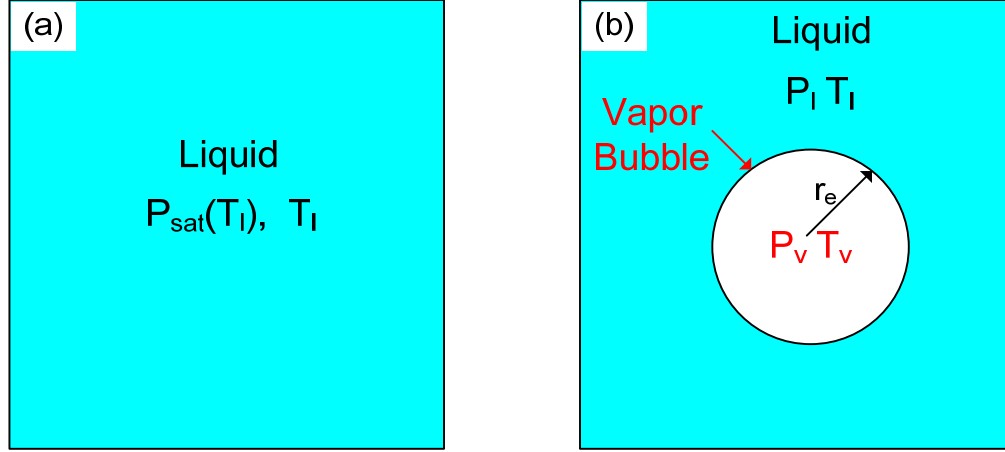


Fig. 2.1 Formation of a vapor bubble inside a liquid pool (a) initial state (b) equilibrium state (after [16])

Because chemical potentials of vapor and liquid phases at the saturation state and the equilibrium state should be the same, equating Eq. (2.6) and Eq. (2.7), one obtains

$$P_{ve} = P_{sat}(T_l) \exp \left[\frac{v_l [P_l - P_{sat}(T_l)]}{RT_l} \right] \quad (2.8)$$

Substituting Eq. (2.3) into Eq. (2.8) to replace P_l , the following equation is obtained.

$$P_{ve} = P_{sat}(T_l) \exp \left[\frac{v_l [P_{ve} - 2\sigma / r_e - P_{sat}(T_l)]}{RT_l} \right] \quad (2.9)$$

In most cases P_{ve} is close to $P_{sat}(T_l)$; therefore, Eq. (1.9) can be further simplified as

$$P_{ve} = P_{sat}(T_l) \exp \left[\frac{-2\sigma / r_e}{\rho_l RT_l} \right] \quad (2.10)$$

Eq. (2.10) is referred to as the Kelvin's equation [51]. It illustrates that under a constant temperature condition, the vapor pressure at equilibrium is smaller than its saturation pressure due to the curvature effect. As a result, for a condition operated at constant pressure, the equilibrium condition dictates that liquid and vapor must be superheated. The amount of superheat required for equilibrium can be obtained from the linearized Clausius equation:

$$\frac{P_l - P_{sat}(T_l)}{T_{sat}(P_l) - T_l} = \frac{h_{lv}}{T_{sat}(P_l) v_{lv}} \quad (2.11)$$

Substituting Eq. (2.3) into Eq. (2.11) to replace P_l , one obtains

$$\frac{P_{ve} - 2\sigma / r_e - P_{sat}(T_l)}{T_{sat}(P_l) - T_l} = \frac{h_{lv}}{T_{sat}(P_l)v_{lv}} \quad (2.12)$$

Since P_{ve} is close to $P_{sat}(T_l)$ and v_{lv} is close to v_v , Eq. (2.12) can be further simplified as

$$T_l - T_{sat}(P_l) = \frac{2\sigma T_{sat}(P_l)}{\rho_v h_{lv} r_e} \quad (2.13)$$

Eq. (2.13) dictates that the amount of superheat at equilibrium is inversely proportional to the equilibrium radius of a vapor bubble ($\Delta T \propto 1/r_e$) given that a higher amount of superheat is required for a smaller vapor bubble.

2.1.1 Maximum Superheat (Spinodal Point)

Fig. 2.2 shows a P - v diagram including metastable regions, spinodal lines and an isotherm with a temperature smaller than the critical temperature.

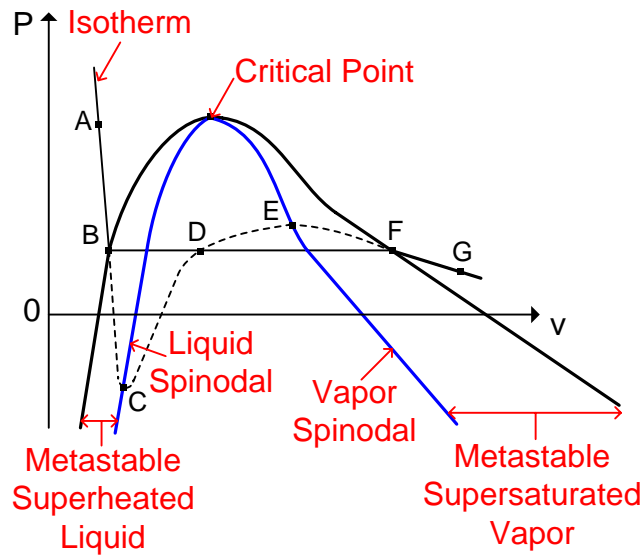


Fig. 2.2 A P - v diagram including the metastable regions, spinodal lines and an isotherm with a temperature smaller than the critical temperature (after [16])

States from point A to point B are in a stable liquid region, from point B to point C are in a metastable superheated liquid region, from point C to point E are in a unstable region where $(\partial P / \partial v)_T > 0$, from point E to point F are in a metastable supersaturated vapor region, and from point F to point G are in a stable vapor region. Point C and E distinguishing a stable region from an unstable region are denoted as the spinodal limits. Point C in Fig. 2.2 corresponds to the maximum superheat required for vapor bubble formation. The states in the metastable and unstable regions can be modeled by the van der Waals equation,

$$P = \frac{(\bar{R}/\bar{M})T}{v-b} - \frac{a}{v^2} \quad (2.14)$$

where \bar{R} and \bar{M} are the universal gas constant and the molecular mass, respectively. In Eq. (2.14), a and b are the mass-based van der Waals constants [16], which accounts the effects of intermolecular force and finite molecular volume, respectively. These van der Waals constants are related to the critical pressure (P_c) and temperature (T_c) because of the consistency of the thermodynamic properties with the critical point conditions as:

$$a = \frac{27(\bar{R}/\bar{M})^2 T_c^2}{64P_c} \quad (2.15)$$

$$b = \frac{(\bar{R}/\bar{M})T_c}{8P_c} \quad (2.16)$$

The van der Waals equation can be non-dimensionalized as:

$$P_r = \frac{8T_r}{3v_r - 1} - \frac{3}{v_r^2} \quad (2.17)$$

where $T_r = T/T_c$, $P_r = P/P_c$ and $v_r = v/v_c$. The spinodal points can be obtained by differentiating the van der Waals equation (Eq. (2.17)) with respect to v_r and setting $(\partial P_r / \partial v_r)_{T_r} = 0$.

The stability of a phase can be deduced from the chemical potential variation along the isotherm. By integrating the Gibbs-Duhem equation from point A to an arbitrary point,

$$\mu - \mu_A = \int_{P_A}^P v dP \quad (2.18)$$

and using the van der Waals equation (2.17) to evaluate the integral in Eq. (2.18), one can obtain the chemical potential versus pressure diagram as shown in Fig. 2.3. The regions from point A to point C and from point E to point G in Fig. 2.3, chemical potential reduces as the process evolves; therefore, the states in these regions are stable. However, chemical potential increase when the states move from point C to point E as shown in Fig. 2.3; therefore, the region from point C to point E is an unstable region.

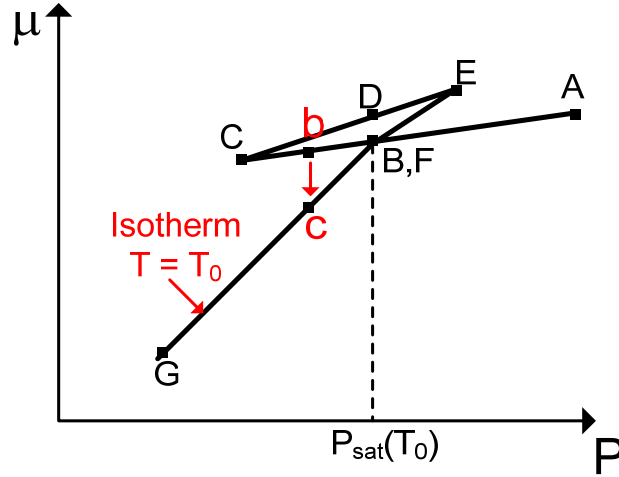


Fig. 2.3 Chemical potential versus pressure along an isotherm (after [16])

2.1.2 Stability at Equilibrium

The stability of the system after a vapor bubble formed inside a liquid pool with an equilibrium radius r_e (see Fig. 2.1(b)) is evaluated. The resultant change in Gibbs free energy after bubble formation is [16]:

$$\Delta G = \hat{N}_v (\hat{g}_v - \hat{g}_l) + 4\pi r^2 \sigma_i - \hat{N}_v \hat{v}_v (P_v - P_l) \quad (2.19)$$

where $\Delta G = G - G_0$, \hat{N}_v is number of moles of vapor molecules, \hat{g}_v and \hat{g}_l are the molar specific Gibbs free energies for liquid and vapor respectively, σ_i is the surface energy per unit area and \hat{v}_v is the molar specific volume of vapor.

For a pure fluid, the specific Gibbs free energy is equal to the chemical potential ($g = \mu$). In addition, mechanical equilibrium requires that $P_v = P_l + 2\sigma/r_e$ and the total volume of the bubble, $\hat{N}_v \hat{v}_v$, is equal to

$$\hat{N}_v \hat{v}_v = (4/3)\pi R^3 \quad (2.20)$$

It follows that at equilibrium condition Eq. (2.19) is reduced as

$$\Delta G_e = (4/3)\pi r_e^2 \sigma_i \quad (2.21)$$

Substituting Eq. (2.20) into Eq. (2.19), we obtain

$$\Delta G = \hat{N}_v (\hat{g}_v - \hat{g}_l) + 4\pi r^2 \sigma_i - (4/3)\pi r^3 (P_v - P_l) \quad (2.22)$$

The change in Gibbs free energy of Eq. (2.22) could be Taylor expanded as:

$$\Delta G = \Delta G_e + \left(\frac{d\Delta G}{dr} \right)_{r=r_e} (r - r_e) + \frac{1}{2} \left(\frac{d^2\Delta G}{dr^2} \right)_{r=r_e} (r - r_e)^2 + \dots \quad (2.23)$$

Also, from the Gibbs-Duhem's equation, we obtain

$$\left(\frac{\partial \hat{g}_v}{\partial P_v} \right)_T = \hat{v}_v \quad (2.24)$$

Further, the equilibrium condition at $r = r_e$ gives us:

$$\left(\frac{d\Delta G}{dr} \right)_{r=r_e} = 0 \quad (2.25)$$

Using Eq. (2.24) and the ideal gas law of $v = \frac{RT}{P}$, the second order derivative of ΔG respect to r at $r = r_e$ gives us:

$$\left(\frac{d^2\Delta G}{dr^2} \right)_{r=r_e} = -\frac{8\pi\sigma_i}{3} \left[2 + \frac{1}{1 + (2\sigma_i/r_e)P_l} \right] \quad (2.26)$$

Substituting Eq. (2.25), Eq. (2.26) and Eq. (2.21) into Eq. (2.23), we obtain

$$\Delta G = \frac{4}{3} \pi\sigma_i r_e^2 - \frac{4\pi\sigma_i}{3} \left[2 + \frac{1}{1 + (2\sigma_i/r_e)P_l} \right] (r - r_e)^2 + \dots \quad (2.27)$$

Dividing Eq. (2.27) with respect to Eq. (2.21), we obtain

$$\frac{\Delta G}{\Delta G_e} = \frac{\Delta G}{(4/3)\pi\sigma_i r_e^2} = 1 - \left[2 + \frac{1}{1 + (2\sigma_i/r_e)P_l} \right] \left(\frac{r}{r_e} - 1 \right)^2 + \dots \quad (2.28)$$

where the term $(2\sigma_i/r_e)P_l \gg 1$. As a result, Eq. (2.28) can be further simplified as:

$$\frac{\Delta G}{\Delta G_e} = 1 - 2 \left(\frac{r}{r_e} - 1 \right)^2 + \dots \quad (2.29)$$

This equation has a maximum at $r = r_e$. In addition, at the condition $r \rightarrow \infty$, the metastable superheated liquid must turn into a superheated vapor. This evolution is indicated as the transition from point b to point c in Fig. 2.3. The decrease in chemical potential (μ) implies a

decrease in the specific Gibbs free energy and a negative value of the change of Gibbs free energy (ΔG). Therefore, at $r \rightarrow \infty$, ΔG must be negative. At the same time, at $r \rightarrow 0$, ΔG must be zero. As a result, the change of Gibbs free energy (ΔG) versus bubble radius (r) must have the trend shown in Fig. 2.4.

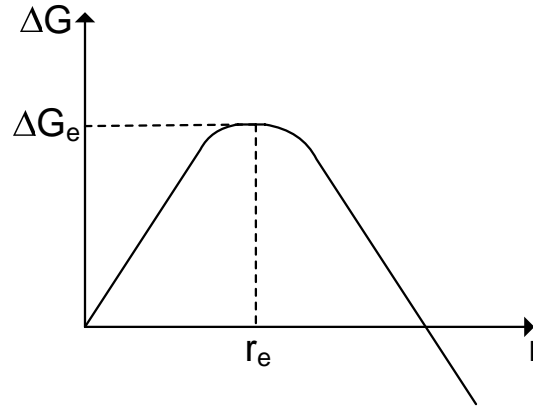


Fig. 2.4 Variation of the change of system Gibbs free energy with bubble radius for a vapor bubble spontaneously formed in a superheated liquid (after [16])

It indicates that the equilibrium state is an unstable equilibrium condition since the resultant change of Gibbs free energy has a maximum value at equilibrium radius. It also suggests that a vapor bubble having a radius smaller than the equilibrium radius will spontaneously disappear whereas it will spontaneously grow when its radius is larger than the equilibrium radius.

2.2 Heterogeneous Nucleation

Heterogeneous nucleation is referred to as vapor bubble formation from the cavities on the heating surface as shown in Fig. 2.5. The superheat required for homogeneous nucleation could be as high as that the temperature of liquid reaches the spinodal limit. For water at one atmosphere, this temperature is about 200 °C [16]. It is noted that the superheat for heterogeneous nucleation is much less than it for homogeneous nucleation. In general, boiling could happen at a superheat below than 10 °C because of the presence of trapped vapor/gas in the cavities on the heating surface. The exact value of the required superheat varies, which is dependent on surface morphology and liquid properties.

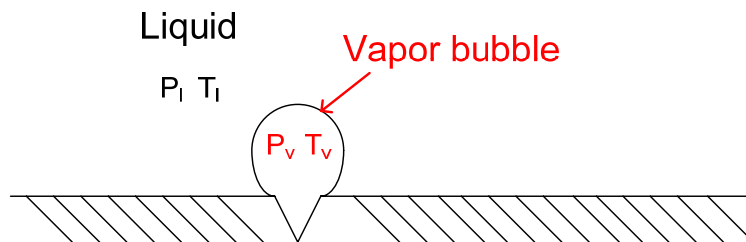


Fig. 2.5 A schematic of heterogeneous nucleation

From previous section, we know that the equilibrium radius of vapor bubble is inversely proportional to the liquid superheat. In addition, this equilibrium condition is an unstable condition and only the bubbles having a radius larger than the equilibrium radius at the given temperature can grow. Since the formed vapor bubbles on the cavities have values of the radii directly related to the sizes of the cavities, it follows that at a particular temperature only certain sizes of the cavities on the surface can be activated.

2.2.1 Active Cavity Sizes

Hsu [52] had evaluated the relationship between the active cavity size and the required superheat on a heating surface. As the wall is heated, there is a thermal boundary layer built up near the heating wall in which the liquid temperature is higher than the saturation temperature as shown in Fig. 2.6. The temperature profile of the liquid inside the thermal boundary layer can be modeled by a one-dimensional transient conduction equation:

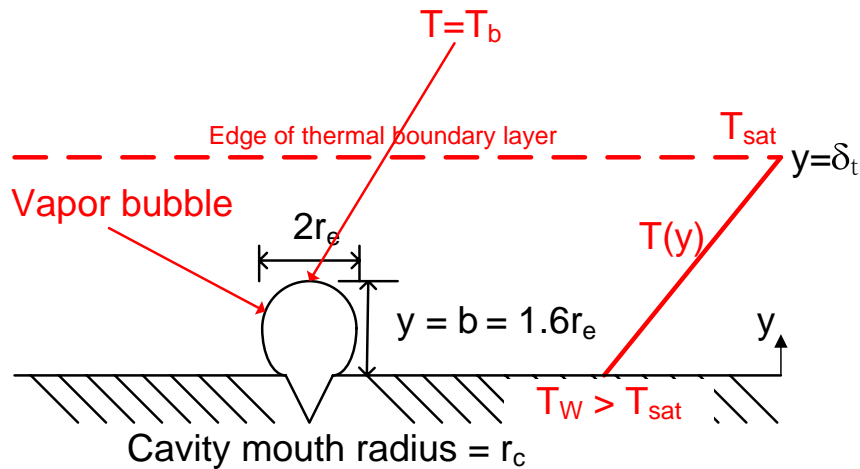


Fig. 2.6 A schematic of vapor bubble formation at the cavity on a heating surface

$$\frac{\partial \theta}{\partial t} = \alpha \left(\frac{\partial^2 \theta}{\partial y^2} \right) \quad (2.30)$$

where $\theta = T - T_{sat}$ and α is the thermal diffusivity. The initial and boundary conditions are:

$$\theta = 0 \text{ at } t = 0 \quad (2.31)$$

for $t > 0$

$$\theta = \theta_w = T_w - T_{sat} \quad \text{at } y = 0 \quad (2.32)$$

$$\theta = 0 \quad \text{at } y = \delta_t \quad (2.33)$$

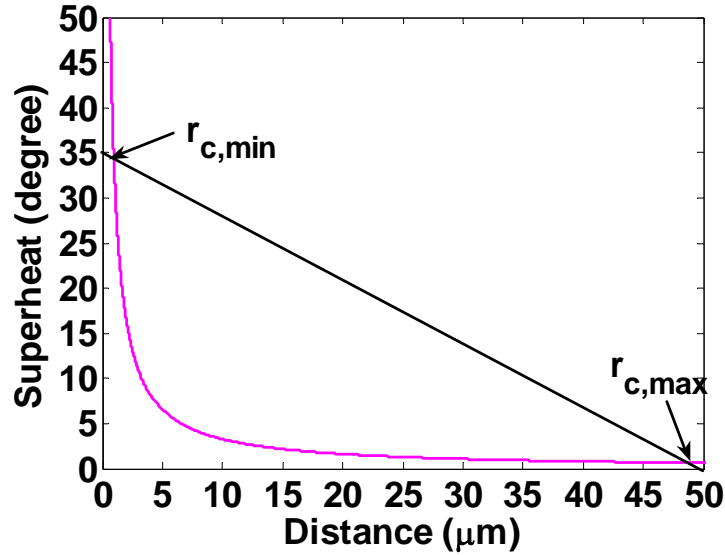


Fig. 2.7 The temperature profile inside the thermal boundary layer where the dark straight line is the steady state solution of Eq. (2.30) and the pink solid curve is the superheat required as a function of distance from Eq. (2.35)

The solution of Eq. (2.30) for $t \rightarrow \infty$ is the dark straight line shown in Fig. 2.7. Hsu [52] had postulated a simple relationship among the height of the bubble (b) the radius of the bubble (r_e) and the mouth radius of the cavity (r_c) as

$$b = 2r_c = 1.6r_e \quad (2.34)$$

It is argued that vapor bubble can only grow when the temperature at $y = b$ (the farthest point on the bubble from the heating wall) is greater than the required equilibrium superheat T_l at $y = b = 1.6 r_e$ in Eq. (2.13). Replacing r_e with y into Eq. (2.13), we obtain

$$T_l - T_{sat}(P_l) = \frac{3.2\sigma T_{sat}(P_l)}{\rho_v h_{lv} y} \quad (2.35)$$

The result of Eq. (2.35) is plotted in Fig. 2.7 as the pink solid curve. It can be seen from Fig. 2.7 that only at the region between $r_{c,max}$ and $r_{c,min}$ the liquid temperature in the thermal boundary layer is larger than the required superheat of Eq. (2.35). As a result, only the cavities having sizes in this range could be activated at this applied wall temperature T_w . After some manipulation, the minimum cavity radius ($r_{c,max}$) and the maximum cavity radius ($r_{c,min}$) can be expressed as the following equation [52].

$$\begin{cases} r_{c,\min} \\ r_{c,\max} \end{cases} = \frac{\delta_t}{4} \left[1 \begin{cases} - \\ + \end{cases} \right] \sqrt{1 - \frac{12.8\sigma T_{sat}(P_l)}{\rho_v h_v \delta_t \theta_w}} \quad (2.36)$$

Where the thickness of the thermal boundary layer (δ_t) is an unknown parameter, but is corresponding to the incipient wall superheat of boiling [52], at which $r_{c,\min} = r_{c,\max}$, i.e., there is no active cavities for nucleation. For a given incipient temperature of nucleation (θ_w), equating $r_{c,\min}$ and $r_{c,\max}$ in Eq. (2.36), the value of δ_t can be obtained. As an example for water at one atmosphere under saturation condition, for a given incipient wall superheat of 15 K, the thermal boundary layer of 14 μm is obtained. The activated cavity radius versus wall superheats at this incipience temperature according to Eq. (2.36) is plotted in Fig. 2.8.

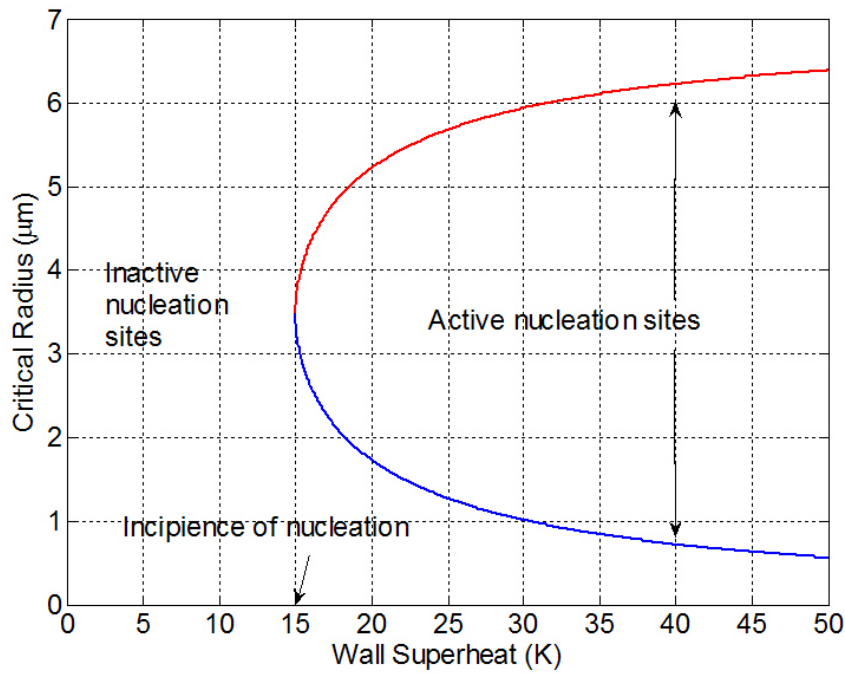


Fig. 2.8 Activated cavity size versus wall superheat for water at one atmosphere, The blue and red curves are minimum and maximum sizes of active cavities at a given wall superheat, respectively.

It illustrates a few important points: (1) there is a minimum superheat required for heterogeneous nucleation. (2) There is a finite range of activated cavities for a given wall superheat. This range is dependent on fluid properties, thermal boundary layer thickness, etc.

2.3 Heat Transfer Coefficient of Pool Boiling

It has been demonstrated that the single-phase forced convection heat transfer concept can be extended to explain the high heat transfer coefficient of nucleate boiling [16, 53-55]. The high

temperature liquid nearby the heating wall is transferred away by the convection induced by vapor bubbles. The schematic of the convective heat transfer induced by departing vapor bubbles is shown in Fig. 2.9.

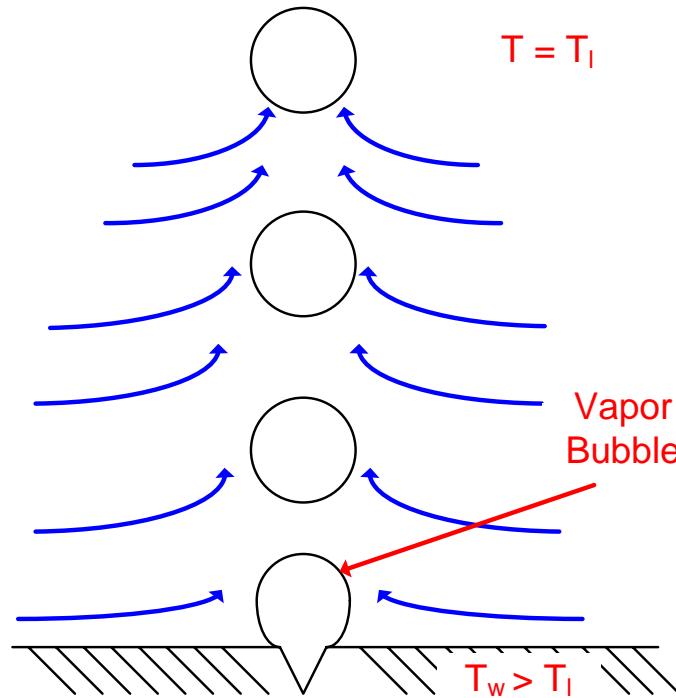


Fig. 2.9 The convective heat transfer induced by departing vapor bubbles

2.3.1 Rohsenow's Model

Rohsenow [53] postulated that the high heat transfer coefficient associated with nucleate boiling is a result of local agitation due to liquid flowing behind the wake of departing bubbles. As a result, if we could find appropriate length and velocity scales associated with the convection process, the heat transfer coefficient of nucleate boiling could be correlated by forced convection heat transfer as

$$Nu_b = \frac{hL_b}{k_l} = B Re_b^{(1-r)} Pr_l^{(1-s)} \quad (2.37)$$

where L_b is the appropriate bubble length scale and Pr_l is the Prandtl number of the liquid. The Reynolds number Re_b is expressed as

$$Re_b = \frac{\rho_b u_b L_b}{\mu_l} \quad (2.38)$$

where u_b and L_b are appropriated velocity and length scales, respectively, and can be expressed as

$$u_b = \frac{q''}{\rho_v h_{lv}} \quad (2.39)$$

$$L_b = d_d = C_b \theta \left[\frac{2\sigma}{g(\rho_l - \rho_v)} \right]^{1/2} \quad (2.40)$$

Where $L_b=d_d$ is the bubble departure diameter and C_b is a constant specific to the system. The bubble Reynolds number defined in Eq. (2.38) using vapor density and vapor superficial velocity in the numerator could be interpreted as a ratio of vapor inertia to liquid viscous force. The heat transfer coefficient is defined as

$$h = \frac{q''}{T_w - T_{sat}(P_l)} \quad (2.41)$$

Substituting equations from (2.38) to (2.41) into Eq. (2.37) and after some rearrangement yields

$$\frac{q''}{\mu_l h_{lv}} \left[\frac{\sigma}{g(\rho_l - \rho_v)} \right]^{1/2} = \left(\frac{1}{C_{sf}} \right)^{1/r} \text{Pr}_l^{-s/r} \left[\frac{C_{pl} [T_w - T_{sat}(P_l)]}{h_{lv}} \right]^{1/r} \quad (2.42)$$

where

$$C_{sf} = \frac{\sqrt{2}C_b \theta}{A} \quad (2.43)$$

Eq. (2.42) is the well-known Rohsenow correlation [53] for pool boiling heat transfer. The values of $r = 0.33$ and $s = 1.7$ were recommended for this correlation. Subsequently, Rohsenow recommended that s should be changed to 1.0 for water. The values of C_{sf} were tabulated by Vachon et al. [56], Rohsenow et al. [57], Kreith et al. [58], Piret et al. [59], and Bergles et al. [60] as shown in Table 2.1 below:

Table 2.1 Values of C_{sf} in Eq. (2.42) from [56-60]

Liquid-surface combination	C_{sf}
Water on Teflon pitted stainless steel	0.0058
Water on scored copper	0.0068
Water on ground and polished stainless steel	0.0080
Water on emery polished copper	0.0128
Water on chemically etched stainless steel	0.0133
Water on mechanically polished stainless steel	0.0132
Water on emery polished, paraffin-treated copper	0.0147
Water on nickel (vertical tube)	0.0060
Water on stainless steel (horizontal tube)	0.0150
Water on stainless steel (horizontal tube)	0.0200

Water on copper (vertical tube)	0.0130
Carbon tetrachloride on copper (vertical tube)	0.0130
Isopropyl alcohol on copper (vertical tube)	0.0022
n-Butyl alcohol on copper (vertical tube)	0.0030
n-Pentane on lapped copper	0.0049
n-Pentane on emery polished nickel	0.0127
n-Pentane on emery polished copper	0.0154
Carbon tetrachloride on emery polished copper	0.0070

It is recommended that an experiment should be conducted to determine the value of C_{sf} . If it is not possible and the values of C_{sf} could not be found in the literature, a value of $C_{sf} = 0.013$ is recommended as a first approximation.

2.3.2 Microconvection Model

Forster and Zuber [55] also postulated that the heat transfer coefficient could be expressed as a form similar to Eq. (2.37):

$$Nu_b = \frac{hL_b}{k_l} = B Re_b^n Pr_l^m \quad (2.44)$$

Unlike Rohsenow [53], they made use of different length and velocity scales to evaluate the above equation. They showed that the bubble growth radius R and the velocity of the interface are given by

$$R = Ja(\pi\alpha_l t)^{1/2} \quad (2.45)$$

$$\dot{R} = Ja\left(\frac{\pi\alpha_l}{4t}\right)^{1/2} \quad (2.46)$$

where Ja is the Jacob number. The Jacob number indicates a ratio between sensible heat and latent heat, which is expressed as

$$Ja = \frac{[T_w - T_{sat}(P_w)]c_{pl}\rho_l}{\rho_v h_{lv}} \quad (2.47)$$

The Reynolds number and the Nusselt number are obtained by using $2R$ as the length scale and \dot{R} as the velocity scale:

$$Re_b = \frac{2R\rho_l\dot{R}}{\mu_l} = \pi Ja^2 Pr_l^{-1} \quad (2.48)$$

$$Nu_b = \frac{q''(2R)}{(T_w - T_l)k_l} \quad (2.49)$$

Direct determination of the length scale from Eq. (2.45) is not possible since the radius varies with time. Forster and Zuber [55] proposed the following relation for the length scale:

$$2R = R_c \left[\left(\frac{\rho_l \dot{R}^2}{2\sigma/R_c} \right) \left(\frac{R^2}{R_c^2} \right) \right]^{1/4} = Ja \left[\frac{4\pi^2 \alpha_l^2 \rho_l^2 \sigma^2}{(P_{sat}(T_w) - P_l)} \right]^{1/4} \quad (2.50)$$

$$R_c = \frac{2\sigma}{P_{sat}(T_w) - P_l} \quad (2.51)$$

Further, Forster and Zuber [55] found that the pool boiling heat transfer data could be correlated by using Eq. (2.44) with constants $A = 0.0015$, $n = 0.62$ and $m = 0.33$. It is noted that in this model the reference temperature difference of $T_w - T_l$ is used for boiling heat transfer (see Eq. (2.49)) instead of $T_w - T_{sat}(P_l)$. It indicates that the subcooling of liquid has a significant effect on the heat transfer coefficient. However, the available experimental data usually illustrates that the effect of subcooling is not important on the heat transfer coefficient of pool boiling.

2.3.3 Vapor-Liquid Exchange Model

Forster and Greif [54] provided a means to explain the contradictory trends noted above. They postulated that the bubbles act as multiple micro-pumps, which pump hot liquid away from the heating surface (see Fig. 2.9). The heat transfer rate per active nucleation site is

$$q_s = \rho_l \left(\frac{2\pi}{3} \right) R_{max}^3 f \times c_{pl} \left(\frac{T_w + T_l}{2} - T_l \right) \quad (2.52)$$

where $\left(\frac{2\pi}{3} \right) R_{max}^3$ is the volume of liquid being pumped away from each vapor bubble, f is the

bubble release frequency and the liquid temperature near the wall is assumed equal to $\frac{T_w + T_l}{2}$.

The total heat flux is equal to the product of the nucleation site density and the heat transfer rate per site as

$$q'' = \rho_l \left(\frac{2\pi}{3} \right) R_{max}^3 f \times c_{pl} \left(\frac{1}{2} \right) (T_w - T_l) n_a \quad (2.53)$$

Eq. (2.53) again appears to be strongly dependent on the liquid subcooling. However, it is noted by Forster and Greif [54] that as the subcooling increase, the maximum radius (R_{max}) decreases and release frequency (f) increases. The net result of these three effects compensates each other, given that the effect of subcooling on heat transfer coefficient is not obvious.

2.3.4 Comparison of Various Models

In addition to the aforementioned models, there are some other models based on thermodynamic similitude and dimensional analysis. Borishansky [61] proposed a correlation based on the thermodynamic similitude:

$$q'' = (A^*)^{0.33} [T_w - T_{sat}(P_l)]^{3.33} [F(P_r)]^{3.33} \quad (2.54)$$

$$A^* = 0.1011P_c^{0.69} \quad (\text{with } P_c \text{ in bar}) \quad (2.55)$$

$$F(P_r) = 1.8P_r^{0.17} + 4P_r^{1.2} + 10P_r^{10} \quad (2.56)$$

$$P_r = P_l / P_c \quad (2.57)$$

where q'' is in W/m^2 and the relationships of A^* and $F(P_r)$ are proposed by Mostinski [62].

Stephan and Abdelsalam [63] proposed a model based on a dimensional analysis and fits from experimental data:

For water:

$$q'' = \{C_1 [T_w - T_{sat}(P_l)]\}^{1/0.327} \quad (2.58)$$

For hydrocarbons:

$$q'' = \{C_2 [T_w - T_{sat}(P_l)]\}^{1/0.330} \quad (2.59)$$

For cryogenic fluids:

$$q'' = \left\{ C_3 (\rho c_p k)_c^{0.117} [T_w - T_{sat}(P_l)] \right\}^{1/0.376} \quad (2.60)$$

For refrigerants:

$$q'' = \{C_4 [T_w - T_{sat}(P_l)]\}^{1/0.255} \quad (2.61)$$

Values of the constants C_1 through C_4 can be found in [64]. The units to be used are kg/m^3 for ρ , $W/m^2 \cdot ^\circ C$ for c_p , $^\circ C$ for $T_w - T_{sat}(P_l)$, and W/m^2 for q'' .

The microconvection model [55] aforementioned can be further manipulated and the resultant correlation is expressed as

$$q'' = 0.00122 \left(\frac{k_l^{0.79} c_{pl}^{0.45} \rho_l^{0.49}}{\sigma^{0.5} \mu_l^{0.29} h_{lv}^{0.24} \rho_v^{0.24}} \right) [T_w - T_{sat}(P_l)]^{1.24} \Delta P_{sat}^{0.75} \quad (2.62)$$

where ΔP_{sat} is the difference in saturation pressure corresponding to the temperature difference $T_w - T_{sat}(P_l)$. The units in the above equation can be $k_l \sim \text{W/m}^\circ\text{C}$, $c_{pl} \sim \text{kJ/kg}^\circ\text{C}$, $\rho_l \sim \text{kg/m}^3$, $\rho_v \sim \text{kg/m}^3$, $T_w - T_{sat}(P_l) \sim ^\circ\text{C}$, $\Delta P_{sat} \sim \text{Pa}$, $\sigma \sim \text{N/m}$, $\mu_l \sim \text{Ns/m}^2$, $h_{lv} \sim \text{kJ/kg}$ and $q'' \sim \text{W/m}^2$. The theoretical predictions for water at one atmosphere from four models of Eq. (2.42), Eq. (2.54), Eq. (2.58) and Eq. (2.62) are plotted in Fig. 2.10 for comparison, where C_{sf} of 0.013 is used in Eq. (2.42).

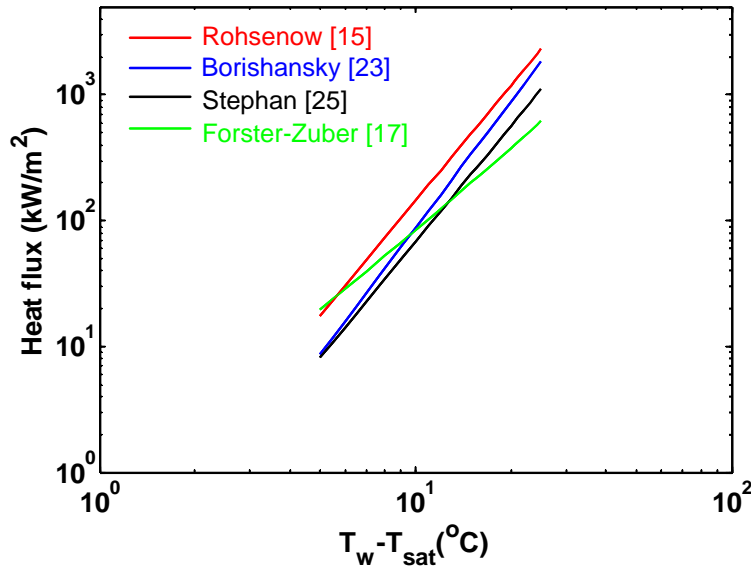


Fig. 2.10 Comparison of various heat transfer coefficient models in pool boiling

In summary, high heat transfer coefficient in boiling heat transfer can be generally explained by the forced convection models. As indicated by Eq. (2.53), the dominant factors affecting the heat transfer coefficient of boiling are nucleation site density, bubble releasing frequency and bubble departure diameter, etc. The four curves in Fig. 2.10 are about in the range of variation of data reported in boiling heat transfer. The heat flux has a large scattering whereas the wall superheat varies only few degrees.

2.4 Summary

In pool boiling, first, homogeneous nucleation and heterogeneous nucleation were introduced. As an effect of surface curvature, the equilibrium condition requires that liquid must be superheated for vapor bubble formation. Superheated liquid is in a thermodynamically metastable region. Homogeneous nucleation may need the superheat to be as high as that liquid temperature reaches the spinodal point, which distinguishes a metastable region from an unstable region. Since the equilibrium condition poses a maximum value of the change of Gibbs free energy, it is an

unstable equilibrium. As a result, only vapor bubbles having radii larger than the equilibrium radius at the given temperature could grow whereas vapor bubbles with radii smaller than the equilibrium radius will spontaneously disappear. In heterogeneous nucleation, because of the presence of the air/vapor trapped cavities, the superheat for heterogeneous nucleation is much less than it for homogeneous nucleation. Meanwhile, since the radii of the vapor bubbles are directly related to the sizes of the cavities and as a result of the unstable equilibrium, there is only a range of cavities could be activated at a given wall temperature. Further, the high heat transfer coefficient in pool boiling can be generally explained by the concept of single-phase forced convection given that vapor transport seems to be the dominant resistance in boiling heat transfer.

Chapter 3 Fundamentals of Heat Pipes

As mentioned in chapter one, the key component in a heat pipe is its wick structure. Fig. 3.1 compares three commonly used commercially available wick structures [9].

The screen wick is the simplest wick structure. It is consisted of metal fabric wrapped around the heat pipe wall. The capillary force is determined by the size of the pores on the layer of the metal fabric and the permeability is determined by the number of wraps and the spacing of the warps.

Sintered-metal wicks are made by sintering metal powder. This type of wick has a large capillary force due to a small spacing between sintering particles. Due to the same reason, its permeability could be small as well. Its effective thermal conductivity is much larger than the screen-type wick structure due to a better thermal contact between sintered particles. This type of wick is more difficult to fabricate compared to the screen-type wick.

Axial groove wicks are made by extrusion of grooves into the inner wall of the heat pipe. Since the size of the grooves is larger than the spacing between sintered particles in the sintered-particle wick and screen size in the screen-type wick, it has a large permeability and a correspondedly low capillary force. It also shows a high effective thermal conductivity. The drawback of this wick is that it is difficult to fabricate for long heat pipes.

	Sintered Copper	Grooves	Wrapped Screen
Capillary force	Large	Small	Large
Permeability	Small	Large	Large
Conductance	Large	Large	Small
Cost	High	Low	Low

Fig. 3.1 Three commonly used commercially available wick structures

3.1 Operation Limits

Although heat pipes have a very high thermal conductance, their operation is limited by a few factors. These limits are illustrated as follows.

3.1.1 Capillary Limit

For a heat pipe to function appropriately the capillary pressure provided by the wick structure at the evaporator section must be larger than the total pressure drop built up in the system,

consisting of liquid and vapor pressure drops as well as a pressure drop resulted from an orientation against gravity.

$$\Delta P_c \geq \Delta P_l + \Delta P_v + \Delta P_g \quad (3.1)$$

This condition sets up the capillary limit for a heat pipe. Fig. 3.2 displays a schematic showing the menisci profiles at the evaporator and condenser sections, respectively. The capillary pressure at the evaporator section is equal to:

$$\Delta P_c = P_1 - P_4 = \frac{\sigma}{r_e} \quad (3.2)$$

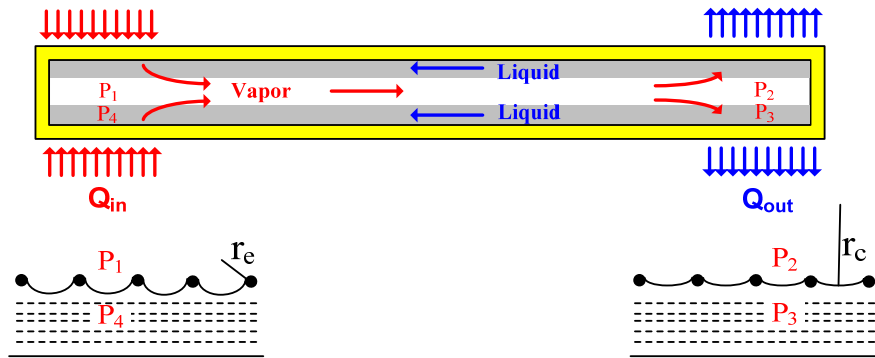


Fig. 3.2 A schematic showing meniscus profiles at the evaporator and condenser sections

where r_e is the equilibrium radius of curvature at the evaporator section.

The vapor pressure drop across the vapor-core region can be obtained from the analysis of a laminar flow through a circular cross-sectional tube with a diameter D_v :

$$\Delta P_v = P_1 - P_2 = \frac{64}{Re_v} \left(\frac{L_{eff}}{D_v} \right) \frac{\rho_v u_v^2}{2} \quad (3.3)$$

where L_{eff} is the effective length of fluid flow and Re_v is the Reynolds number of vapor. The effective length could be assumed as:

$$L_{eff} = L_a + \frac{L_e + L_c}{2} \quad (3.4)$$

where L_a , L_e and L_c are the lengths of adiabatic section, evaporator section and condenser section, respectively. The liquid pressure drop is obtained from Darcy's law for the liquid flowing through a porous wick structure as

$$\Delta P_l = P_3 - P_4 = \frac{\mu_l L_{eff} \dot{m}}{\kappa \rho_l A_w} \quad (3.5)$$

where κ is the porous medium permeability and A_w is the cross-sectional area of the wick structure. The value of the permeability is dependent on the morphology of the porous medium. A correlation of the permeability for micro pin-fin array is proposed by Fowler and Bejan [65] as:

$$\kappa = \frac{d^2 \phi^3}{125(1-\phi)^2} \quad (3.6)$$

where d is the diameter of the pin fin and ϕ is the porosity.

At the condenser section, the meniscus is relatively flat given that the vapor pressure is approximately equal to liquid pressure:

$$P_2 = P_3 \quad (3.7)$$

The maximum heat transfer rate (Q_{\max}) is equal to the product of mass flow rate (\dot{m}) in Eq. (3.5) and the latent heat h_{lv} . From Eq. (3.2) to Eq. (3.7), we obtain

$$Q_{\max} = \frac{\kappa \rho_l A_w h_{lv}}{\mu_l L_{eff}} \left[\frac{\sigma}{r_e} - \frac{64}{\text{Re}_v} \left(\frac{L_{eff}}{D_v} \right) \frac{\rho_v u_v^2}{2} \right] \quad (3.8)$$

Eq. (3.8) gives the maximum heat transfer rate corresponding to the capillary limit.

3.1.2 Boiling Limit

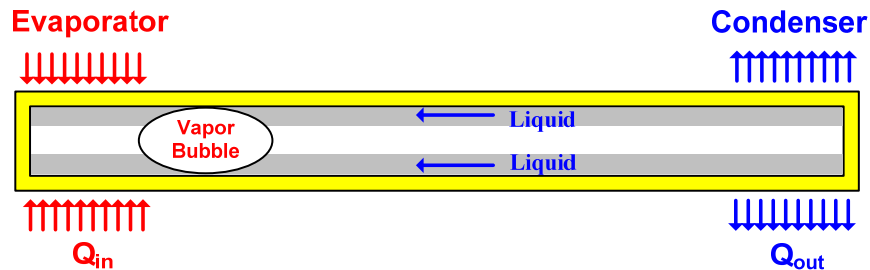


Fig. 3.3 A schematic of the boiling Limit of heat pipe operation

In conventional heat pipes, boiling in the wick has been considered as an operational limit. Boiling is detrimental because the formed vapor bubble could block the liquid flow and cause dry out of liquid inside the wick (see Fig. 3.3). Nucleate boiling in the heat pipe is initiated by heterogeneous nucleation where cavities on the surface trapping air/vapor are activated via superheating liquid. The required superheat for activating the cavities with certain sizes is shown in Fig. 2.8. As an example, giving a wall superheat of 30 °C, the sizes of the activated cavities are in the range between 1 μm to 6 μm .

3.1.3 Sonic Limit

Another limit for heat-pipe operation is the sonic limit: The vapor velocity reaches sonic or supersonic values which causes a choked working condition. The velocity of the vapor for a given heat flux can be calculated as

$$u_c = \frac{Q}{\rho_v h_{lv} \left(\frac{\pi D_v^2}{4} \right)} \quad (3.9)$$

where Q is the applied power. As an example, assuming $Q = 100$ W and $D_v = 1$ cm, from Eq. (3.9), one arrives at an $u_c = 0.95$ m/s, which is much less than the speed of sound. Hence, choking is not a generally encountered limit for current heat pipe operation.

3.1.4 Entrainment Limit

In a heat pipe, vapor is flowing to the condenser end whereas liquid is counter-flowing to the evaporator end. This counter-flowing of two fluids causes a velocity shear at the vapor/liquid interface at the top surface of the wick. The magnitude of the shear force is dependent on the relative velocity of the two fluids as well as fluid properties. This condition is referred to as Helmholtz instability [16, 66]. The result of the instability is to entrain water droplets into the vapor flow and transport them to the condenser end. The surface tension of liquid is to stabilize the interface. When the situation of entrainment is serious, there may not have enough amount of liquid to reach the evaporator end. This may cause an operational limit of heat pipes. The Weber number, We , is an measurement of the probability of entrainment, which is a ratio between the inertia vapor force to the surface tension of liquid:

$$We = \frac{\rho_v u^2}{2\pi \left(\frac{\sigma}{d} \right)} \quad (3.10)$$

where d is a characteristic length scale of the wick structure. It is assumed that the entrainment will be serious when the Weber number, We , is ~ 1 [67]. The critical velocity of entrainment is expressed by

$$u_c = \sqrt{\frac{2\pi\sigma}{\rho_v d}} \quad (3.11)$$

The maximum heat flux corresponding to the critical velocity is:

$$q'' = \rho_v h_{lv} u_c \quad (3.12)$$

Substituting Eq. (3.11) into Eq. (3.12), one obtains:

$$q'' = \sqrt{\frac{2\pi\rho_v h_{iv}^2 \sigma}{d}} \quad (3.13)$$

Eq. (3.13) is the maximum heat flux corresponding to the entrainment limit. As an example for water at one atmosphere, assuming d is $10 \mu\text{m}$, one reaches a maximum heat flux of $q'' = 3.3 \times 10^4 \text{ W/cm}^2$. This value is much higher than the current heat flux operated; therefore, the entrainment limit is not a generally encountered limit in heat pipe operation.

In summary, the operation limits of heat pipes are introduced in this section. Among these limits, capillary limit and boiling limit are most likely to occur in current heat pipe operation.

3.2 Thermal Resistances in Heat Pipes

Fig. 3.4 shows a schematic of a heat pipe and its corresponding thermal resistance network, where R_1 is the thermal resistance of the container wall, R_2 is the wick thermal resistance, R_3 is the liquid-vapor interfacial thermal resistance, R_4 is the vapor-core thermal resistance and R_5 , R_6 , and R_7 are corresponding thermal resistances at the condenser end.

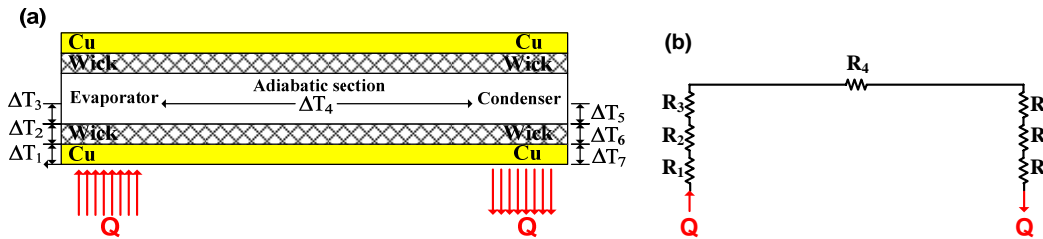


Fig. 3.4 (a) a schematic of a heat pipe and (b) its corresponding thermal resistance network

For a circular heat pipe, the thermal resistances (unit, for example, $^{\circ}\text{C/W}$) of the heat pipe are:

(1) Thermal resistance of the container wall:

$$R_{wall} = \frac{\ln(D_o / D_i)}{2\pi L_e k_{wall}} \quad (3.14)$$

where D_o , and D_i are the outer diameter and the inner diameter of the heat pipe and k_{wall} is the thermal conductivity of the container wall.

(2) The wick thermal resistance:

$$R_{wick} = \frac{\ln(D_i / D_v)}{2\pi L_e k_{wick}} \quad (3.15)$$

where D_v is the diameter of the vapor core and k_{wick} is the effective thermal conductivity of the wick structure. An approximated model of the effective thermal conductivity is:

$$k_{wick} = k_s(1-\phi) + k_l(\phi) \quad (3.16)$$

where k_s , k_l and ϕ are the thermal conductivities of solid and liquid and porosity of the porous medium, respectively. Note that this approximation of the effective thermal conductivity can only be applied at certain conditions where heat is transported parallelly.

(3) Interfacial thermal resistance:

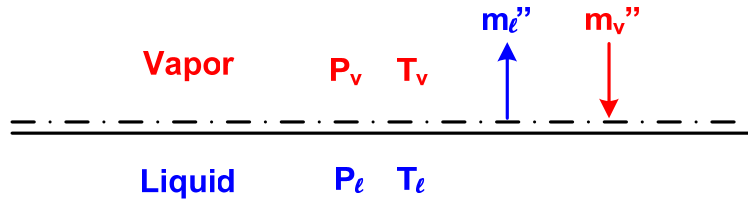


Fig. 3.5 Mass flux at a liquid-vapor interface

Fig. 3.5 shows a mass flux diagram at a liquid-vapor interface. From kinetic theory, the average speed of the vapor molecules which follow the Boltzmann distribution at temperature T_v is:

$$u_{av} = \sqrt{\frac{8k_B T_v}{\pi m}} \quad (3.17)$$

where m is the molecular mass. The molecular flux at a given direction is

$$\frac{nu_{av}}{4} \quad (3.18)$$

where n is the number density of the vapor. The mass flux at a given direction is equal to:

$$m_v'' = m \frac{nu_{av}}{4} \quad (3.19)$$

By using equations from (3.17) to (3.19) and the ideal gas law, $P_v = nk_B T_v$, one obtains the vapor mass flux at a given direction:

$$m_v'' = \frac{2\alpha}{2-\alpha} \left(\frac{1}{2\pi R} \right)^{1/2} \left(\frac{P_v}{\sqrt{T_v}} \right) \quad (3.20)$$

where α is the accommodation coefficient, which accounts the portion of the molecules crossing the interface without being reflected back. The concept of the accommodation coefficient is similar to the concept of the transmission coefficient in optics, which accounts the portion of light transmitted without being reflected back. Similar operation can be applied to liquid and one obtains the mass flux of liquid as

$$m_i'' = \frac{2\alpha}{2-\alpha} \left(\frac{1}{2\pi R} \right)^{1/2} \left(\frac{P_l}{\sqrt{T_l}} \right) \quad (3.21)$$

The net flux across the interface is the difference between Eq. (3.20) and Eq. (3.21):

$$m_i'' = \frac{2\alpha}{2-\alpha} \left(\frac{1}{2\pi R} \right)^{1/2} \left(\frac{P_l}{\sqrt{T_l}} - \frac{P_v}{\sqrt{T_v}} \right) \quad (3.22)$$

The net heat flux across the interface is obtained as:

$$q_i'' = h_{iv} \frac{2\alpha}{2-\alpha} \left(\frac{1}{2\pi R} \right)^{1/2} \left(\frac{P_l}{\sqrt{T_l}} - \frac{P_v}{\sqrt{T_v}} \right) \quad (3.23)$$

Eq. (3.23) can be simplified as:

$$q_i'' = h_{iv} \frac{2\alpha}{2-\alpha} \left(\frac{1}{2\pi RT_v} \right)^{1/2} (P_l - P_v) \quad (3.24)$$

By using the Clausius equation and the ideal gas law, one obtains:

$$\frac{\Delta P}{\Delta T} = \frac{P_v h_{iv}}{RT_v^2} \quad (3.25)$$

Replacing the pressure difference in Eq. (3.24) with temperature difference using Eq. (3.25) and dividing the temperature difference by the heat flux, one obtains the interfacial thermal conductance (unit, for example, W/m²K) as

$$h_i = h_{iv} \frac{2\alpha}{2-\alpha} \left(\frac{1}{2\pi RT_v} \right)^{1/2} \left(\frac{h_{iv} P_v}{RT_v^2} \right) \quad (3.26)$$

This interfacial thermal conductance is largely dependent on the value of the accommodation coefficient. However, the exact value of the accommodation coefficient relies on the experimental environment and has a large variation. Gumerov et al. [68] had showed that the accommodation coefficient can vary from 0.006 to 1 for water vapor, depending on the environmental conditions. As an example, the values of the interfacial thermal conductance for water under saturation condition at one atmosphere are 24 W/cm²K and 1500 W/cm²K for α equals 0.03 and 1, respectively.

(4) Vapor-core thermal resistance:

The pressure drop across the vapor-core adiabatic section is obtained from the analysis of a laminar flow through a circular tube:

$$\Delta P = \frac{8\mu_v \dot{m}}{\pi \rho_v} \left(\frac{L_a}{r_v^4} \right) \quad (3.27)$$

where r_v is the radius of the vapor core region. The thermal resistance at the vapor-core region (R_{vc} (unit, for example, °C/W)) is obtained from:

$$R_{vc} = \frac{\Delta T}{Q} \quad (3.28)$$

where Q is the applied power. From Eq. (3.27), Eq. (3.28), Eq. (3.25) and $Q = \dot{m}h_{lv}$, one obtains

$$R_{vc} = \frac{8RT_v^2 \mu_v L_a}{\pi \rho_v P_v h_{lv}^2 r_v^4} \quad (3.29)$$

The typical orders of magnitudes of the thermal resistances in a heat pipe are shown in Table 3.1. Note that the high thermal conductance of the heat pipe only happens in the vapor-core region. This is because that we make analogy of the large latent heat accompanied with the phase-change process in terms of a thermal resistance (see Eq. (3.29)). Moreover, the thermal resistance of the wick structure is the dominant thermal resistance in the heat pipe.

Table 3.1 Typical orders of magnitudes of thermal resistances in a heat pipe

Thermal Resistance	(°C/W)
R_{wall}	10^{-3}
R_{wick}	10^{-2}
R_i	10^{-4}
R_{vc}	10^{-5}

The parameters used: $D_o = 1$ cm, $D_i = 9$ mm, $D_v = 8$ mm, $L_e = 2$ cm, $L_a = 6$ cm, $L_c = 2$ cm, $k_{wall} = 300$ W/m-K, $k_{wick} = 60$ W/m-K, $T_v = 323$ K, $P_v = 12$ kPa, $h_{lv} = 2234$ kJ/kg and $\alpha = 1$.

3.3 Summary

Although heat pipes have a high thermal conductance, their operation is limited by a few factors such as capillary limit, boiling limit, sonic limit and entrainment limit. Among these limits, capillary limit and boiling limit are two mostly encountered operational limits. Second, the high thermal conductance of a heat pipe only happens in the vapor-core region and the wick structure causes the dominant thermal resistance. Third, the interfacial conductance is generally small

compared to other resistances in a heat pipe but its value is largely dependant on the environmental conditions.

Chapter 4 Enhancing Critical Heat Flux in Pool Boiling

4.1 Introduction

With the increasingly growing concerns on climate change, energy has become a critical issue. More than 90 % of the world's total energy is generated by heat engines and 40 % of the heat engines are based on the Rankine cycle. In the thermodynamic heat engines, boiling heat transfer plays an important role in several thermal devices such as boilers, heat exchangers, condensers etc. One of the most important parameters of boiling heat transfer is the critical heat flux, CHF, which determines the maximum power that could be handled by a boiling heat transfer device. Therefore, enhancing the CHF will have a great impact on many energy conversion and utilization systems. However, the exact mechanism leading to CHF in boiling remains elusive so far, because of the highly complex phenomena in boiling. In general, the mechanisms of CHF can be classified into two categories: (1) far-field and (2) near field.

4.1.1 Far-field CHF Mechanism

The most well-known CHF models are based on the hydrodynamic instability theory, first proposed by Zuber in 1959 [17] and later modified by Lienhard and Dhir in 1973 [18], which asserts that the occurrence of CHF is because of pool hydrodynamics. As the applied heat flux increases, the velocity of vapor columns increases, resulting in an increase of the velocity shear between up-flowing vapor and down-flowing liquid. Eventually, the vapor columns become unstable, causing a large retarding force on down-flowing liquid and prevent liquid from coming back to the heater surface. A vapor blanket is then formed on the heater surface, which manifests itself as the CHF. The model of CHF based on the hydrodynamics can be expressed as:

$$q_{CHF} = u_c \rho_v h_{lv} (A_v / A) \quad (4.1a)$$

$$u_c = \left(\frac{2\pi\sigma}{\rho_v \lambda_H} \right)^{1/2} \quad (4.1b)$$

where u_c , ρ_v , h_{lv} and A_v/A in Eq. (4.1a) represent critical vapor velocity, vapor density, latent heat and an area ratio of vapor columns and heater surface, respectively, and σ and λ_H in Eq. (4.1b) are the surface tension of liquid and the critical Helmholtz wavelength on vapor columns, respectively. The critical velocity in Eq. (4.1b) is obtained from a linearized instability analysis at an interface between two fluids with relative velocities [16, 66]. This type of instability is referred to as the Helmholtz instability [16, 66], in which the velocity shear between two fluids disrupts the interface and surface tension of liquid stabilizes it. The critical vapor velocity (u_c) in Eq. (4.1b) corresponding to the Helmholtz wavelength (λ_H) is a priority to obtain the hydrodynamic limit. Zuber assumed that the Helmholtz wavelength (λ_H) should be equal to the perimeter of the vapor column ($\lambda_H=2\pi R$), a condition of Plateau-Rayleigh instability of a liquid jet [69]. Meanwhile, in the transition boiling regime, an unstable vapor film forms underneath a liquid pool on the heater surface, a condition depicted by the Taylor instability [16, 66, 70]. By approaching the CHF point from the transition boiling regime, he postulated that the radius of

vapor columns (R) and the separation of vapor columns equal to $\lambda_C/4$ and λ_C , respectively, where $\lambda_C (=2\pi[\sigma/(g(\rho_l - \rho_v))]^{1/2})$ is the critical wavelength of Taylor instability [3, 6], resulting in an area ratio of vapor columns and a heater surface of $\pi/16$. The Helmholtz wavelength is then derived as $\lambda_H = \pi\lambda_C/2$. Zuber further approximated the numerical term of $3/\sqrt{2\pi}$ as one to obtain the model of CHF expressed as:

$$q_{CHF} = 0.131\sqrt{\rho_v}h_{lv}[\sigma g(\rho_l - \rho_v)]^{1/4} \quad (4.2)$$

where ρ_l is the liquid density and the area ratio (A_v/A) in Eq. (4.1a) is equal to $\pi/16$. Lienhard and Dhir [18] claimed that the Helmholtz wavelength (λ_H) should be equal to the most dangerous Taylor instability wavelength λ_D ($\lambda_D = \sqrt{3}\lambda_c$ [16, 70]) since this mode of disturbance will be the fastest growing mode once it appears in the system in the transition boiling regime. This results in a different proportionality constant as shown:

$$q_{CHF} = 0.149\sqrt{\rho_v}h_{lv}[\sigma g(\rho_l - \rho_v)]^{1/4} \quad (4.3)$$

It is worth noting that both Eq. (4.2) and (4.3) have the same functional form as the model proposed by Kutateladze [71] based on a dimensional analysis:

$$q_{CHF} = K\sqrt{\rho_v}h_{lv}[\sigma g(\rho_l - \rho_v)]^{1/4} \quad (4.4)$$

where K is found to be 0.16 from the experimental data. For the past few decades, although, the predictions of CHF values based on the hydrodynamic instability theories agree with some of the experimental results [19], they can not explain the dependence of CHFs on surface/material properties, for example, surface wettability [20, 22-27, 30, 39, 72], surface capillarity [27-29], nucleation site density and thermal fin effect [21, 32-34, 40], and substrate effusivity [35-37], etc.

4.1.2 Near-field CHF Mechanisms

Besides the hydrodynamic instability mechanism which deals with the flow dynamics far away from the heater surface, there are other proposed CHF mechanisms which primarily consider the flow and heat transfer close to the heater, so called near-field mechanism. The literature investigating the near-field effects on CHF is summarized as follows:

4.1.2.1 Macrolayer Dry-out Model

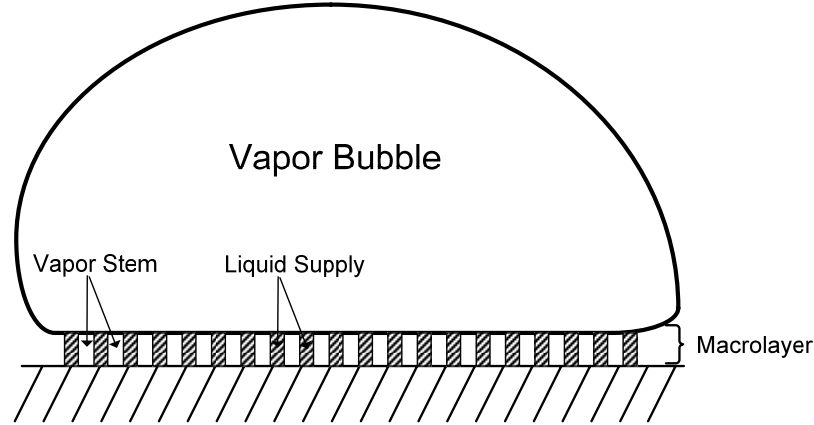


Fig. 4.1 A schematic of the macrolayer

Haramura and Katto in 1983 [73] proposed a macrolayer dry-out model of CHF. The macrolayer is defined as a layer consisting of an array of small vapor jets underneath a large vapor mushroom as showed in Fig. 4.1. It was argued that CHF occurs when the liquid film in the macrolayer dries out before the mushroom departs. The balance of heat flux during this hovering period yields:

$$q'' = \rho_l \delta_c (A - A_v) h_w / (A \tau_d) \quad (4.5)$$

where δ_c , A , A_v , τ_d are critical macrolayer thickness, heater area, area covered by vapor jets and mushroom hovering time, respectively. The critical macrolayer thickness is equal to one quarter of the Helmholtz wavelength ($\delta_c = \lambda_H/4$), which assumes that the dry-out of the macrolayer is due to the presence of the Helmholtz instability on the small vapor jets. The Helmholtz wavelength is associated to the applied heat flux as in Eq. (4.1). The hovering time is obtained by equaling the buoyant force to the upward acceleration of the fluid. The area ratio A_v/A for the condition of $\rho_v/\rho_l \ll 1$ is $A_v/A = 0.0584(\rho_v/\rho_l)^{0.2}$. The obtained final CHF model agrees well with Zuber's model.

4.1.2.2 Hot-spot Limitation

Unal et al. [74] proposed a hypothesis that relates the CHF to the quenches of a hot surface. It was argued that CHF occurs because of the temperature at the dry patches is too high for liquid rewetting. In other words, to reach CHF, the dry-spot temperature at the heater must exceed some critical temperature to preclude liquid-solid contact. When this condition is reached, the dry-spot is sustained and eventually vapor blanket forms on the heater surface.

4.1.2.3 Thermal Effusivity Effect

Thick substrate has a smaller spreading thermal resistance and a larger thermal mass; therefore, it can survive higher heat fluxes because the overheating due to small dry patch can be migrated by

heat conduction or stored through the substrate. It reveals that thermal energy conducted transiently by solid substrate can affect the CHF. Thermal effusivity is a measure of a material's transient conduction ability, which is defined as

$$e = (k\rho C_p)^{1/2} \quad (4.6)$$

where C_p is the specific heat. Saylor et al. in 1989 [37] further defined a parameter $S = \delta^* e$, where δ is the heater thickness, to account the effect of the thermal activity of a heater on CHF. Bar-Cohen and McNeil in 1989 [36] approximated the experimental data of CHF by the following relation:

$$\frac{CHF}{CHF_{max}} \propto \frac{S}{(S + 0.8)} \quad (4.7)$$

The CHF is a function of S for S approximately smaller than 8 [35], where CHF_{max} denotes the value of CHF without affected by S . For a heater with a small value of S , the transient conduction of solid substrate is not fast enough to dissipate the thermal energy during the vapor bubble formation period. Therefore, dry patch on the heater surface expands and leads to CHF.

4.1.2.4 Wettability and Capillarity

Dhir and Liaw in 1989 [20] presented a study investigating the contact angle effect on CHF. The void fraction in the macrolayer was measured experimentally to predict the CHF. Two conclusions were made: First, CHF occurs as a result of the hydrodynamic limit for fully wetting surfaces with a contact angle smaller than 20 degree. Second, for poorly wetting surfaces with a contact angle larger than 20 degree, the CHF is due to the merging of small vapor stems in the macrolayer, given that a higher CHF is observed for surfaces with a smaller contact angle.

Kandlikar in 2002 [39] proposed a theoretical model accounting for wettability effects on CHF. His model is based on a force balance applied on a vapor bubble approaching CHF, which also shows a similar trend, i.e., CHF increases when contact angle reduces.

$$q_{CHF} = \rho_v h_{fg} \left(\frac{1 + \cos \theta}{16} \right) \left[\frac{2}{\pi} + \frac{\pi}{4} (1 + \cos \theta) \cos \Omega \right]^{1/2} \left[\frac{\sigma (\rho_l - \rho_v) g}{\rho_v^2} \right]^{1/4} \quad (4.8)$$

The parameters θ and Ω are the contact angle and the angle relative to the horizontal. Wang and Dhir [21] had also found CHF to increase with wetting. Takata et al. [22] also showed an increase of CHF on a superhydrophilic surface of TiO_2 after ultraviolet (UV) light exposure. Recent studies in pool boiling of nanofluids have shown an improvement of CHF [23-27]. The CHF improvement is mainly because of a change in surface property due to nanoparticle deposition. A higher CHF is obtained for surfaces with a smaller contact angle [23-27]. These studies indicate the effect of surface wettability on CHF.

Meanwhile, for fully wetting surfaces with a zero contact angle, Kim et al. [27] has shown that a greater CHF is achieved for a surface with a larger capillary height. This suggests that capillary

force plays an important role in enhancing CHF. Li and Peterson [29] had conducted pool boiling using copper mesh. They also attributed the enhancement of CHF is due to the large capillary force provided by the porous mesh. Kaviany et al. [28] also illustrated an enhancement of CHF on a modulated porous layer coated surface as a result of a larger capillary limit.

The capillary limit is the limit of the maximum flow rate that can be provided by the surface geometry. For a porous material, at the CHF condition, the largest capillary pressure provided is balanced by a viscous pressure drag corresponding to the critical mass flow rate as shown:

$$\frac{\sigma}{r_c} = \frac{\mu_l \dot{m}_l l}{\rho_l \kappa A_c} \quad (4.9)$$

where σ , r_c , μ_l , \dot{m}_l , l , ρ_l , κ , and A_c are surface tension of liquid, minimum radius of curvature, liquid dynamic viscosity, liquid mass flow rate, liquid flow distance, liquid density, porous medium permeability and flow cross-sectional area, respectively. The minimum radius of curvature is equal to one-half of the interval between the characteristic features. The resultant CHF is equal to the product of the obtained maximum mass flow rate and the latent heat ($q_{CHF} = \dot{m}_l h_{lv}$). These studies suggest that the capillary force plays a significant role for enhancing CHF.

4.1.2.5 Effect of Nucleation Site Density and Thermal Fin on CHF

Chang and You [30] had shown a enhanced CHF on a surface coating of diamond particles with the sizes in the range of a few to tens of microns. The boiling enhancement is attributed to an increase of nucleation site density on the coated surface. Theofanous et al. [31] had conducted a study investigating the phenomena of boiling crisis. They concluded that the boiling heat transfer is not dependent on the hydrodynamics but rather on the surface condition. Meanwhile, the CHF is found to have a direct correlation with the nucleation site density. Honda and co-works [32-34] had shown that using micro pin-fins to enhance the CHF. The enhancement is attributed to an increase of nucleation site density and an increase of heat transfer area by the thermal fin effect.

4.1.3 Heater Size Effect

The effects of heater size on the pool boiling have also been studied. Park and Bergles in 1988 [75] have conducted pool boiling of vertical heaters with one side insulated. The height and width of the heaters were systematically varied. It was shown that an increase of CHF was obtained as the width decreases for heaters with small heights. Bar-Cohen and McNeil [36] have determined the transitional point where heater size starts affecting CHF. The CHF becomes a function of the non-dimensional heater size $L' (=L/L_c)$ for $L' < 20$, where L is the heater length and L_c is the capillary length ($L_c=(\sigma/g(\rho_l-\rho_v))^{0.5}$). On the other hand, Gogonin and Kutateladze [19] have shown that the heater size effect on CHF is absent as the length of the heater becomes larger than $2*L_c$ through a systematic experimental study. Lienhard and Dhir [18] argued that the variation of heater size can affect the CHF via reducing the number of vapor columns present on the heater surface. As the number of vapor columns is confined by the size of the heater, the area ratio (A_v/A) in Eq. (1.63a) is modified. Through a systematic study, it had been shown that

as the heater size smaller than three times of the most dangerous Taylor instability wavelength ($L < 3 * \lambda_D (L < 30L_c)$), the CHF is a function of heater size [18] as

$$q_{CHF} = 1.14 \times q_{CHF,z} \times \left(\frac{N_j \times \lambda_D^2}{A} \right) \quad (4.10)$$

where $q_{CHF,z}$ is the CHF obtained from Eq. (4.2) and N_j is the number of vapor columns present on the surface. It is noted that this equation applies only for certain conditions where heater size is larger than the most dangerous wavelength ($L > \lambda_D (L > 10L_c)$). You et al. [76] argued that for smaller heaters a significant portion of the heater is rewetted from the edges of the heater instead from above as in a infinite plate situation. This re-wetting flow resistance should be a function of heater size given that a higher CHF is observed on a heater with smaller area.

In summary, the mechanisms causing CHF can be broadly classified as far-field hydrodynamic instability-limited or near-field surface property-limited. Although much effort has been carried out to develop the mechanism of CHF for decades, it is still an open question what the exact mechanism causing CHF. General observations are that both the pool hydrodynamics and surface properties could affect the values of the CHF. In addition, it is agreed that the effect of heater size on CHF is to increase the value of the CHF. But the exact transition value of the size of the heater at which heater size start to appear is not conclusive. Moreover, the underlying physics of the heater size effect on the CHF is not conclusive either.

4.2 Nanowires for Enhancing Boiling Heat Transfer

Nanowires array-coated surfaces represent another class of materials that show properties which could potentially be exploited to promote CHF. First, unlike the random deposition of nanoparticles on a heater surface, this nanowire array-coated surface has a more control of surface morphology, which could be an advantage for exploring the CHF mechanism. Second, it has been observed that a surface coated with nanowires can be superhydrophilic [77]. Third, nanowire arrays contain many orders of magnitude more cavities and pores compared to any other treated surface using micro-fabrication or micromachining, thereby effectively increasing the nucleation site density and surface roughness. Furthermore, due to the thermal fin effect, the effective heat transfer area of nanowires may be dramatically higher than that of micro-fabricated surfaces such as those with micro pin-fins [32-34]. Finally, nanowire arrays may act as efficient wicking structures, since the small pores between nanowires provide a very large capillary force, which scales inversely proportionally to the pore size. Due to the above reasons, we hypothesized that CHF could be enhanced on nanowire arrays.

4.2.1 Experimental Approach

Two kinds of nanowires were fabricated to enhance boiling heat transfer: Copper nanowires and silicon nanowires. They exhibit a similar morphology but a large thermal conductivity difference given that the effect of material properties on boiling heat transfer could be examined. In addition, a heater that minimizes thermal contact resistance and enables operation at high heat flux has been developed.

4.2.1.1 Copper Nanowire Synthesis and Bonding

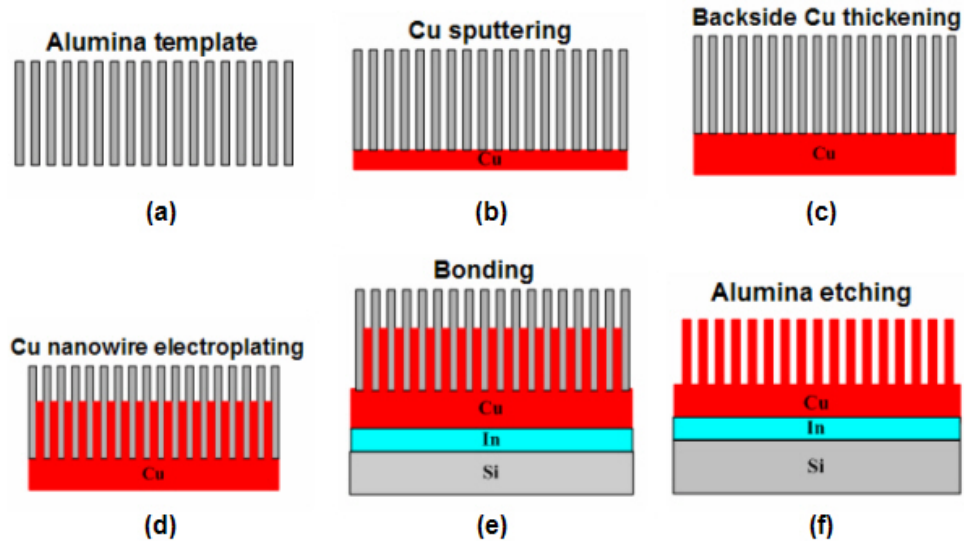


Fig. 4.2 Copper nanowire synthesis and bonding: (a) alumina membrane used as the template for Cu nanowire electroplating, (b) Cu deposition by sputtering on the backside of the membrane, (c) Thickening the backside Cu by electroplating, (d) Cu electroplating through the front side of the membrane to form nanowires, (e) Bonding the membrane onto a Si substrate, (f) Removing alumina by etching in NaOH.

Fig. 4.2 shows the procedure of Cu nanowires synthesis and the subsequent bonding with a Si substrate. The backside of the alumina membrane was first coated with a 500 nm Cu layer by sputtering to serve as the seeding layer for electroplating, and was subsequently thickened to approximately 2.5 μm by electroplating using an acid Cu electroplating solution (Cu Plating Acid Type, Transene Company, Inc.), in order to enhance the mechanical strength of the membrane for handling and the subsequent bonding with a substrate. Cu nanowires were then synthesized by Cu electroplating into the nano-sized pores through the front side of the membrane using a solution specialized for high aspect ratio deposition of Cu (CU2300, Technic Inc.). The membrane with the Cu deposited in the nano-pores was then bonded to a Si substrate coated with a 1 μm Cu layer using a thin foil of indium (50 μm) as a solder material. Freestanding Cu nanowire array on the Si substrate with diameter around 200 nm and length around 40-50 μm was then obtained (Fig. 4.3 (a-b)) by etching the alumina membrane using 0.5 M NaOH solution for 3 hours.

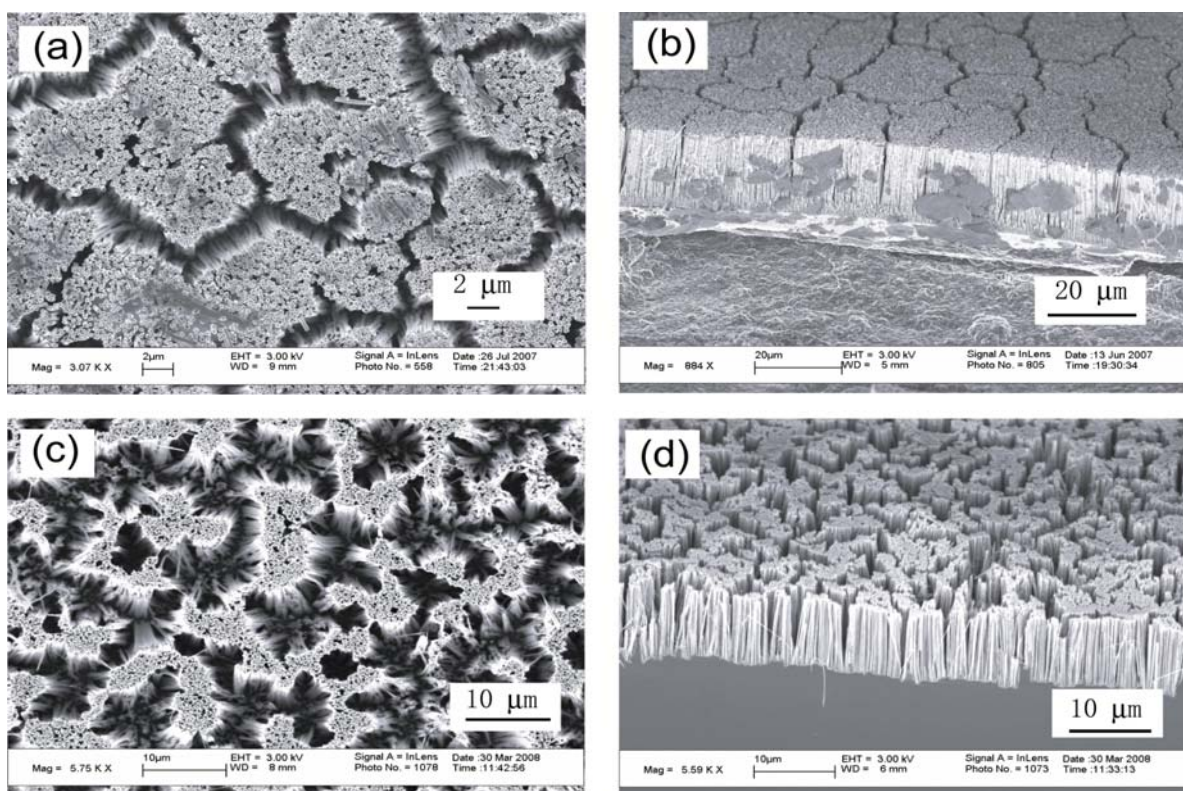


Fig. 4.3 Scanning Electron Microscopy (SEM) graphs of: (a) top view of Cu Nanowires; (b) Cross-section of Cu Nanowires (c) top view of Si Nanowires; (d) Cross-section of Si Nanowires

4.2.1.2 Si Nanowire Synthesis

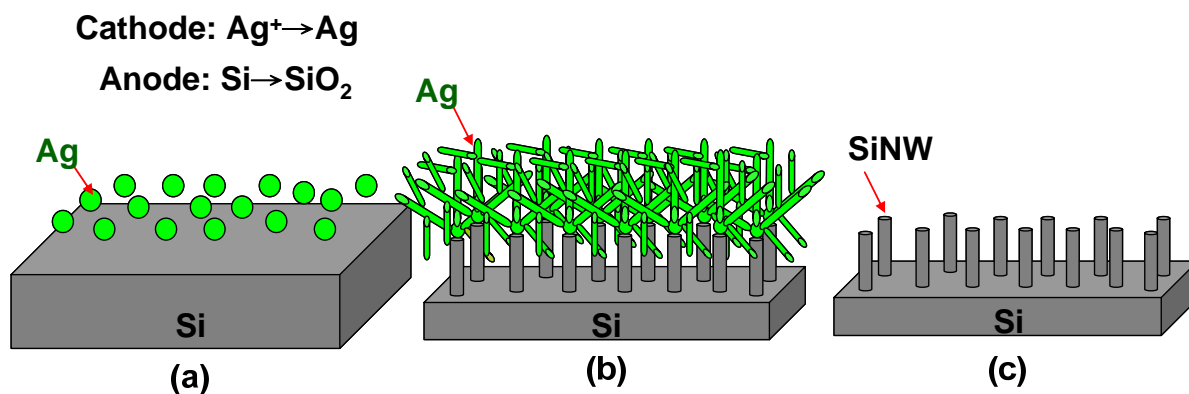


Fig. 4.4 Si nanowire synthesis (a) a redox reaction happens on the surface of Si substrate where Si is oxidized to SiO_2 and Ag^+ is reduced to Ag, (b) HF solution continuous etches the SiO_2 area surrounding by the Ag particles-deposited sites and a dendrite structure of

Ag formed on the surface, (c) the dendrite structure is removed by HNO₃ solution and a free standing Si nanowire array forms on the surface.

Si nanowires were synthesized by a wafer scale aqueous electroless etching (EE) technique [78] as shown in Fig. 4.4. These nanowires were prepared by immersing a Si wafer into an aqueous solution of AgNO₃ and HF acid. On the wafer surface, Ag⁺ reduces to Ag by oxidizing the surrounding Si lattice (Fig. 4.4 (a)), which is subsequently etched by HF. Initial reduction of Ag⁺ forms Ag nanoparticles, which define the spatial region of the following oxidation and etching process. After continuous process of oxidation and etching, the unetched region forms nanowire arrays and the dendrite structure of Ag form on the top the nanowires (Fig. 4.4 (b)). The dendrite structure is removed by HNO₃ etching and a free standing Si nanowire array form on the surface (Fig. 4.4 (c)). Si nanowires synthesized by this technique are vertically aligned, and have diameters in the range of 20-300 nm. In the present study, nanowires of approximately 40-50 μm long were synthesized for the boiling experiments. Fig. 4.3(c) and Fig. 4.3(d) show scanning electron microscopy (SEM) micrographs of the top view and cross-section of Si nanowire arrays used in the present study, respectively.

4.2.1.3 Heater Fabrication

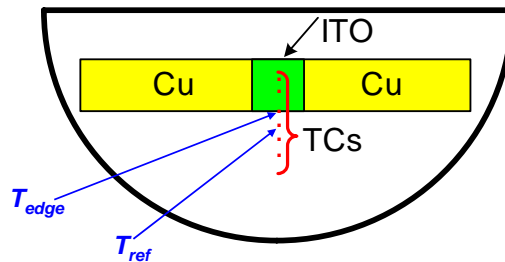


Fig. 4.5 A schematic consisting of ITO heater, two Cu electrodes and thermocouples (TCs)

In order to reach CHF for boiling with water, a heater with heat flux up to several hundred W/cm² is required. The heater used in this study is a thin layer of Indium Tin Oxide (ITO), deposited on the back side of a Si substrate, on which either the Si nanowires were synthesized, or the Cu nanowire arrays were bonded. Heat flux up to 300 W/cm² can be produced on the 1 cm x 1 cm ITO film by Joule heating of direct current supplied via two patterned Cu electrodes (as shown in Fig. 4.5). Since the heater is chemically bonded to the Si wafer that served as the substrate for nanowire arrays, the thermal resistance between the heater and the heating surface is minimized, compared to the interface resistance if thermal epoxy were used.

4.2.2 Test Section and Experimental Setup

The test sample including a Si substrate with nanowires and a heater was mounted to a Teflon block (thermal conductivity 0.2 W/m-K) to ensure thermal insulation (Fig. 4.6). To perform the boiling experiment, the whole test assembly was immersed into a pool of de-ionized (DI) water, which was then heated up to its saturation temperature (100 °C) at 1 atm by a hotplate.

Throughout the whole experiment, the temperature of the ambient water was continuously monitored by a T type thermocouple to ensure it was at 100 °C. After the pool of water is maintained at 100 °C for at least 30 minutes to degas water, power was supplied by a power supply (Agilent N5750A) to the ITO heater incrementally to heat up the Si substrate. The temperature of the heater was measured by two T type thermocouples attached to it and the data was recorded through a data acquisition system (Agilent 34970A). The critical heat flux (CHF) was postulated to be equal to the heating power corresponding to the last observed stable temperature, beyond which a sudden dramatic jump in heater temperature was observed.

The heat flux was calculated as $q'' = \frac{VI}{A}$, where V and I are measured voltage and current across the ITO heater, respectively, and A is the area of the heater. Due to the thermal resistance of the Si substrate between the heater and nanowire array, the temperature reading from the thermocouples has to be corrected in order to obtain the actual wall temperature T_w , which is the temperature at the top surface of the Si substrate. T_w is given by $T_w = T_{TC} - \frac{q''\delta}{k}$, where T_{TC} is the temperature measured by the thermocouples, δ is the thickness of the Si substrate and k is the thermal conductivity of Si (130 W/m-K). The uncertainties of the measured heat fluxes, wall temperatures and the derived heat transfer coefficient are from the accuracies of the power supply and the data acquisition system and the resolution of the thermocouples. This part of uncertainties is attributed to as the systematic uncertainty. In addition to the systematic uncertainty, there are uncertainties of the data repeatability for each data point. The overall uncertainty of each data point is the root mean square (RMS) value of the systematic uncertainty and the data repeatability uncertainty (stand deviation of the multiple data points from different samples). A detailed uncertainty analysis of the data is shown in the Appendix. The relative systematic uncertainty of the CHF and HTC are both about 2 %, which is small compared with the stand deviation of the multiple data points. Thus, the error bars shown in next section of results and discussion only include the stand deviation of multiple data points.

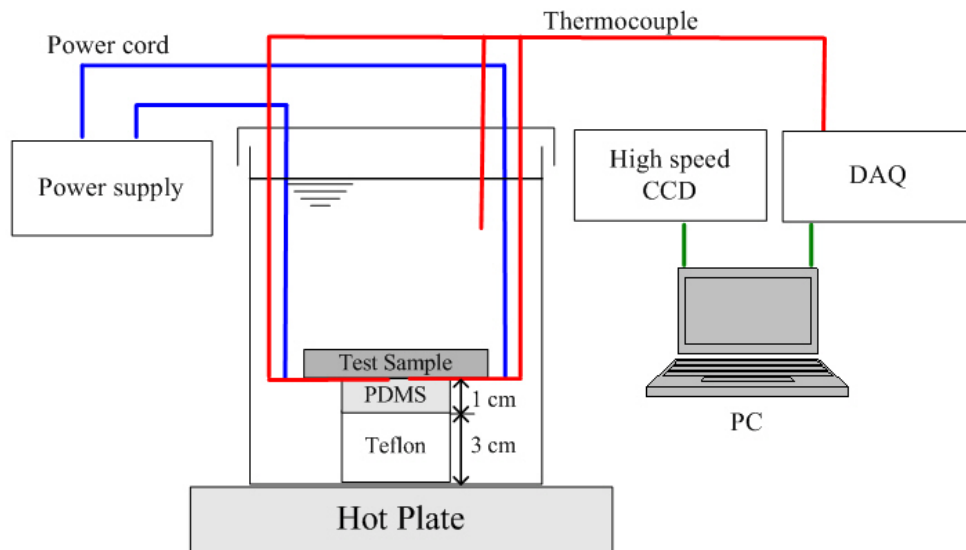


Fig. 4.6 A schematic of the boiling experimental setup, including the test sample, PDMS and Teflon thermal insulators, data acquisition and visualization systems.

4.2.3 Results and Discussion

The boiling curves of plain Si surface, Si and Cu nanowires are shown in Fig. 4.7. Boiling on plain Si surface served as the primary control for the boiling performance comparisons. The error bar shown in the boiling curve for plain Si boiling curve represents the range of CHF and wall superheat at CHF on multiple samples. CHF and HTC for plain Si were found to be 84.13 ± 5.16 W/cm² and 2.46 ± 0.15 W/cm²K, respectively. The boiling results on Si surface presented here are consistent with experimental results reported in the literature for a plain surface, e.g., by Theofanous et al. [40]. Boiling curves of Si and Cu nanowires appear to be similar to each other, although the thermal conductivities for Cu and Si nanowires are dramatically different (400 W/m-K for Cu and ~ 10 W/m-K for EE Si nanowires [78]). This is reasonable as heat transfer in boiling is dominated by bubble dynamics [15, 16, 53-55] rather than heat conduction (see Section 2.3), and the similar boiling behavior is a result of similar morphologies of Si and Cu nanowire arrays. For Si and Cu nanowires, the CHF is 192.26 ± 2.63 W/cm² and 193.66 ± 21.13 W/cm², respectively, while HTC is 6.24 ± 1.24 W/cm²-K and 6.39 ± 0.42 W/cm²-K, respectively, in the wall superheat range of 10-30 K. Both CHF and HTC of nanowires are more than doubled compared to plain Si. The CHF reported here (~ 200 W/cm²) is among the highest reported CHF values.

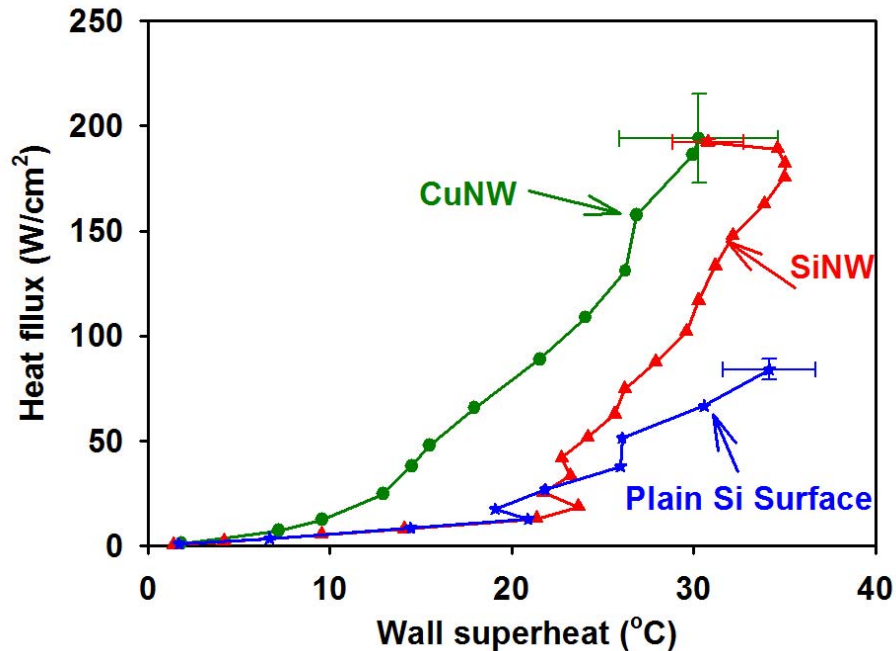


Fig. 4.7 boiling curves for Plain Si surface, Si nanowires and Cu nanowires

The significant enhancement of HTC of nanowires compared to plain surface could be attributed to the following reasons, as we initially anticipated. As shown in Fig. 4.3 (a-d), there are numerous naturally formed defects of several microns in between the Cu or Si nanowires. The size range of active cavities can be calculated (see Section 2.2.1). Based on the incipient wall superheat in the present study (15 K), δ_i is calculated to be 14 μm . Fig. 2.8 shows the predicted $r_{c,\text{min}}$ and $r_{c,\text{max}}$. The sizes of active nucleation cavities are from 1 μm to 6 μm for wall superheat below 30 K, while sub-micron cavities can be activated for wall superheat above 35 K.

Therefore, these cavities are likely to be active cavity sites for heterogeneous nucleation, and more nucleation sites formed between nanowires could result in a higher HTC. This can be further demonstrated by the bubble images as shown in Fig. 4.8, which exhibits that more bubbles were produced for Si nanowires compared to plain Si surface under both moderate heat flux ($\sim 20 \text{ W/cm}^2$) and heat flux close to CHF ($\sim 177 \text{ W/cm}^2$ for Si nanowires and $\sim 93 \text{ W/cm}^2$ for plain Si).

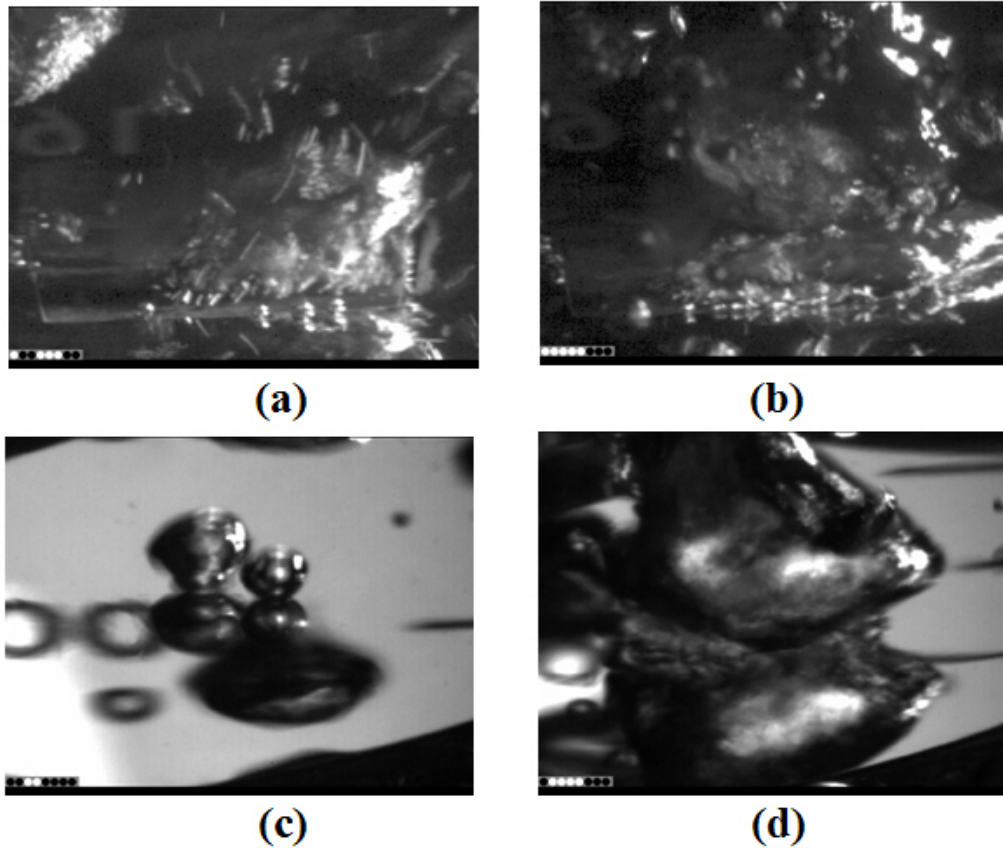


Fig. 4.8 Bubble images: (a) Si Nanowires: 18 W/cm² (b) Si Nanowires: 177 W/cm² (c) Si: 20 W/cm² (d) Si: 93 W/cm²

The enhanced CHF could also be attributed to some unique properties of nanowires. One plausible mechanism is the increased surface wettability. The nearly zero apparent contact angle of water on the nanowire arrays suggests that the nanowire arrays are superhydrophilic (see Fig.

4.9), which is expected to result in a higher CHF. Fig. 4.10 presents the contact angle dependence of CHF. In general, CHF increases as contact angle decreases [20, 39]. To confirm the effect of surface wettability, CHF of pool boiling on a Si substrate coated with a SiO₂ layer was measured and compared against the native Si surface. The contact angles for Si and SiO₂ surfaces are 40° and 15°, respectively (Fig. 4.9). The SiO₂ surface shows a higher CHF (106.71 ± 1.36 W/cm²) compared to plain Si, as shown in Fig. 4.10, which is consistent with Dhir and Liaw's model and experimental data [20] as well as Kandlikar's model [39].

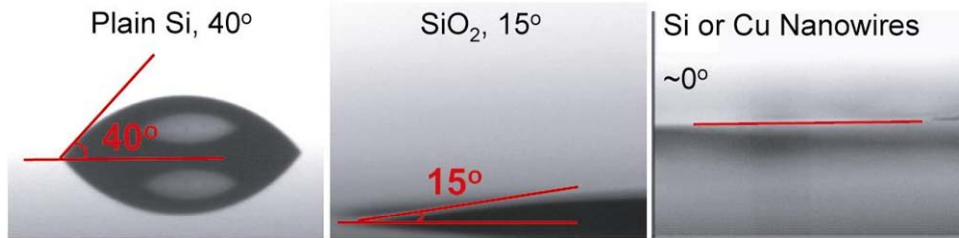


Fig. 4.9 Static contact angles of a water droplet on surfaces of Si, SiO₂, and Si and Cu nanowires.

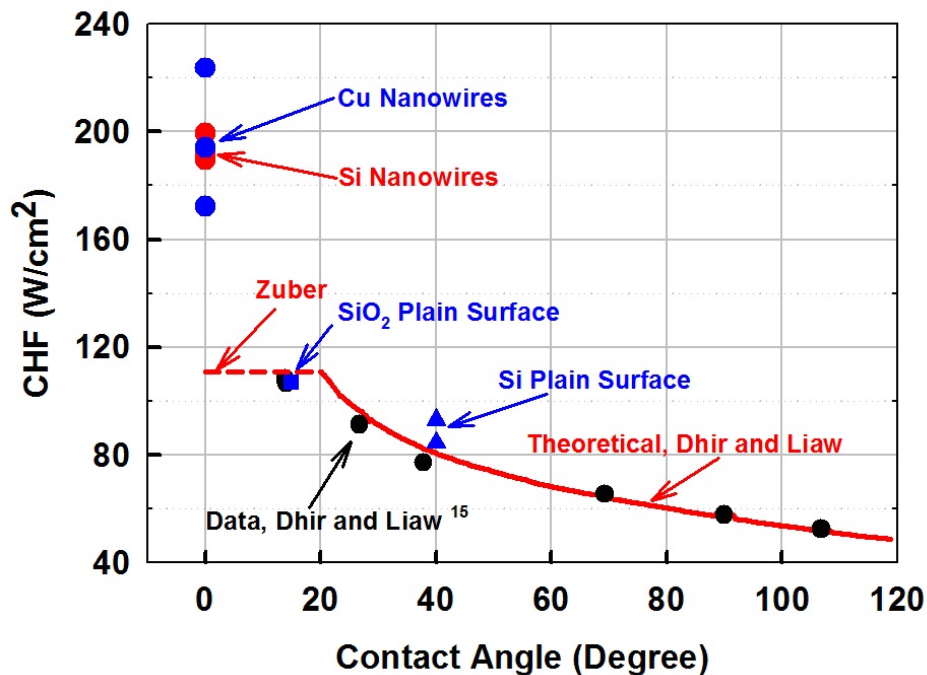


Fig. 4.10 Dependence of CHF on contact angle. CHF of plain Si (blue triangle) and SiO₂ (blue rectangle) observed in the present study follows the theoretical models given by Dhir and Liaw [20] (red solid line) and Zuber [17] (red dashed line) and experimental data of Dhir and Liaw [20] (black circles). However, CHF for Cu and Si nanowires (blue and red circles, respectively) are significantly higher than the theoretical prediction, indicating mechanism besides contact angle dependence is also involved.

An interesting phenomenon was observed in the boiling curves of Si nanowires (see Fig. 4.7), where the wall superheat decreased when heat flux was approaching CHF. This phenomenon can be attributed to the activation of sub-micron cavities in the Si nanowire arrays. The superheat needed to activate these cavities as nucleation sites is higher than 30 K (See Fig. 2.8). When the heat flux approached CHF, the wall superheat is 30 K or higher. Therefore, a large amount of sub-micron cavities can be activated and more bubbles are produced, resulting in a sudden increase in HTC and, consequently, decrease in wall superheat near the CHF. The phenomenon was not observed in Cu nanowires, presumably due to the fact that there are less sub-micron cavities formed in Cu nanowires, as evident in SEM images in Fig. 4.3. This phenomenon may suggest that HTC for pool boiling could be further increased by artificially creating cavity sites of different length scales corresponding to various wall superheats.

4.3 CHF Mechanisms on Si Nanowire Array-coated and Plain Si Surfaces

4.3.1 Test Section

To verify the CHF mechanisms on these nanowire array-coated surfaces and plain Si surfaces, the test section is first modified to reduce thermal spreading. As a result, a more accurate CHF based on the heater area could be obtained. The thermal spreading is referred to the lateral heat conduction within the wafer leading to an area of boiling larger than the heater. The original test section and modified test section are compared in Fig. 4.11. The reduction of thermal spreading is accomplished by a precisely defined heater area via backside lithography and a coating of low-conductivity photoresist (SU8, $\sim 50 \mu\text{m}$) over all areas not covered by the heater on the surface. The area covered by SiNW is thus precisely aligned to the area on the wafer backside where the thin film heater of Indium Tin Oxide (ITO) is deposited. The resulting difference in thermal resistance and surface morphology between the area covered by the SU8 and the area covered by the SiNW array reduces bubbling at the edge of the heaters and a more accurate CHF based on the area of the heater can be obtained. In addition to the edge effect mentioned above, heat can still conduct through the substrate and this conduction heat loss is quantized as

$$q_{cond} = kA_c \frac{T_{edge} - T_{ref}}{x} \quad (4.11)$$

where k is the thermal conductivity of Si substrate, T_{edge} and T_{ref} , are temperatures at the edge of the heater and temperature at distance of x away from the edge (as shown in Fig. 4.5), respectively, whereas A_c is the cross-sectional area of heater which equals to the perimeter of the heater times the thickness of the wafer and x is equal to 2 mm.

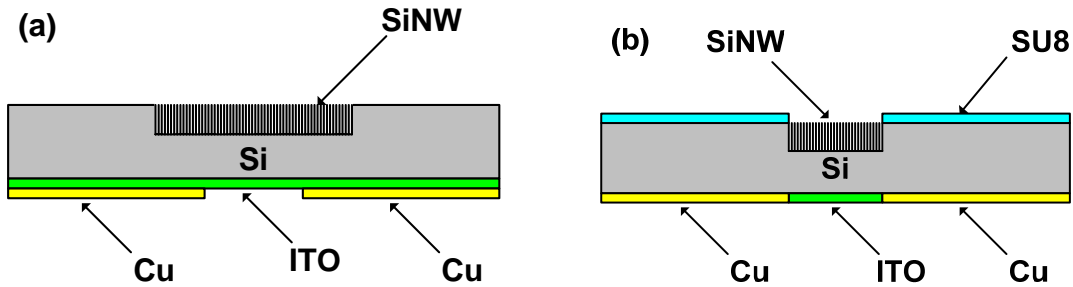


Fig. 4.11 Schematics of (a) original test section and (b) modified test section for minimizing thermal spreading

4.3.2 Results and Discussion

The high obtained CHF_s on nanowire array-coated surfaces could not be explained by the wettability [20] and hydrodynamic limit [17, 18] as shown in Fig. 4.10. The most probably limiting mechanism causing CHF on the nanowire array-coated surfaces is likely the capillary limit. To verify the capillary limit, pool boiling on the SiNWs coated surfaces with four different NW lengths (~ 16 , ~ 32 , ~ 59 and ~ 122 μm as shown in SEM images of Fig. 4.12) with a heater area of 1 cm^2 has been carried out to investigate the capillary limit of CHF. The boiling curves are shown in Fig. 4.13.

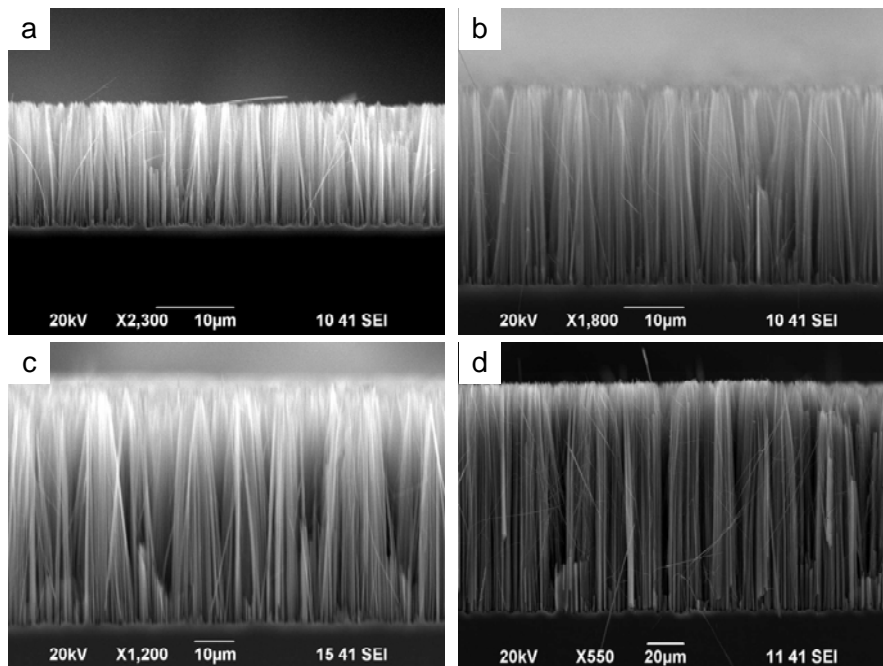


Fig. 4.12 SEM images of a SiNW array with different heights: (a) 16 μm (b) 32 μm (c) 59 μm (d) 122 μm

The values of CHF and heat transfer coefficient, HTC (defined as the CHF divided by the superheat) for NW lengths of ~ 16 , ~ 32 , ~ 59 and ~ 122 μm are 161.59, 156.24, 160.31 ± 12.57 and 164.50 W/cm^2 , respectively, and 5.53, 4.38, 4.39 ± 0.25 and 4.56 $\text{W}/\text{cm}^2\text{K}$, respectively. The CHF values for these four lengths of NW array display a similar value of 159.44 ± 9.71 W/cm^2 .

The condition of the capillary limit is depicted by Eq. (4.9) at which the maximum flow rate is obtained corresponding to a minimum radius of curvature (r_c). Since these nanowire arrays create the dominant flow resistance in the system, the maximum flow rate (the capillary limit) should be inversely proportional to the length of the nanowire provided that the maximum capillary pressure (σ/r_c) is the same for the different heights of nanowires. The fact that the CHF values are independent of nanowire heights suggests that the CHF values of the NW array-coated surfaces are not due to the capillary limit. Meanwhile, the obtained CHF of 159.44 ± 9.71 W/cm^2 is superior to ~ 126 W/cm^2 as predicted by the hydrodynamic limit of saturated water (Eq. (4.3)), which seems to suggest that the hydrodynamic limit does not apply to this case as well.

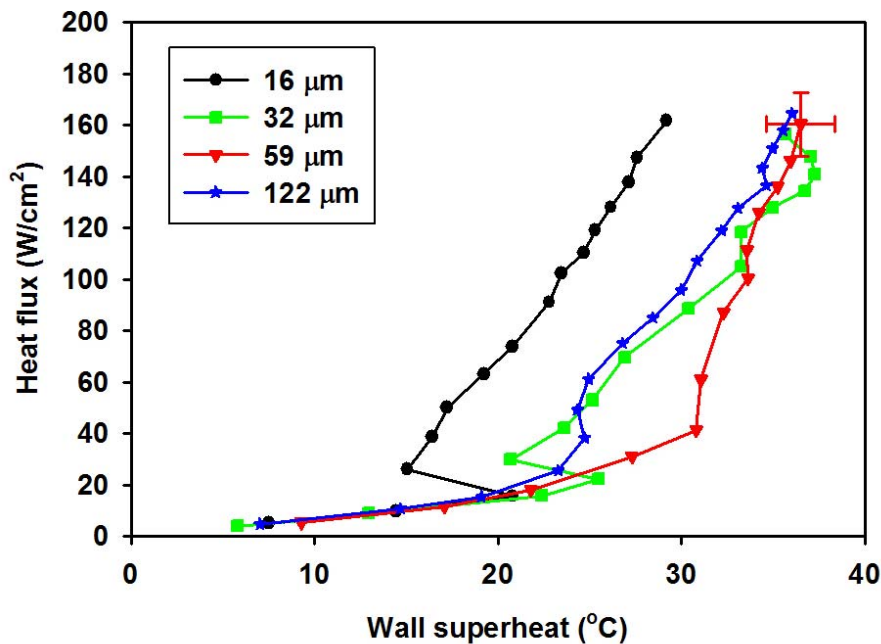


Fig. 4.13 Boiling curves on SiNW array-coated surfaces for different heights of NWs

However, it is noted that the model is applied to an infinite heater surface in which the Helmholtz wavelength was assumed to be equal to the most dangerous Taylor wavelength ($\lambda_H = \lambda_D$) and the diameter of the vapor column and the spacing of vapor columns are $\lambda_D/2$ and λ_D , respectively, resulting in an area ratio of vapor columns and heater surface (A_v/A in Eq. (4.1)) of $\pi/16$. This Taylor wavelength (λ_D) for saturated water (2.5 cm) is larger than the heater size adopted here of 1 cm^2 given that only one vapor column can be present on the heater surface. Therefore, there is no ground to assume that the Helmholtz wavelength is equal to the most

dangerous Taylor instability wavelength (the spacing between vapor columns) for this size of the heater. The fundamental question arises: What will be the Helmholtz wavelength if the hydrodynamic instability still applies? To address this, pool boiling experiments on SiNW array-coated surfaces with various heater sizes have been carried out.

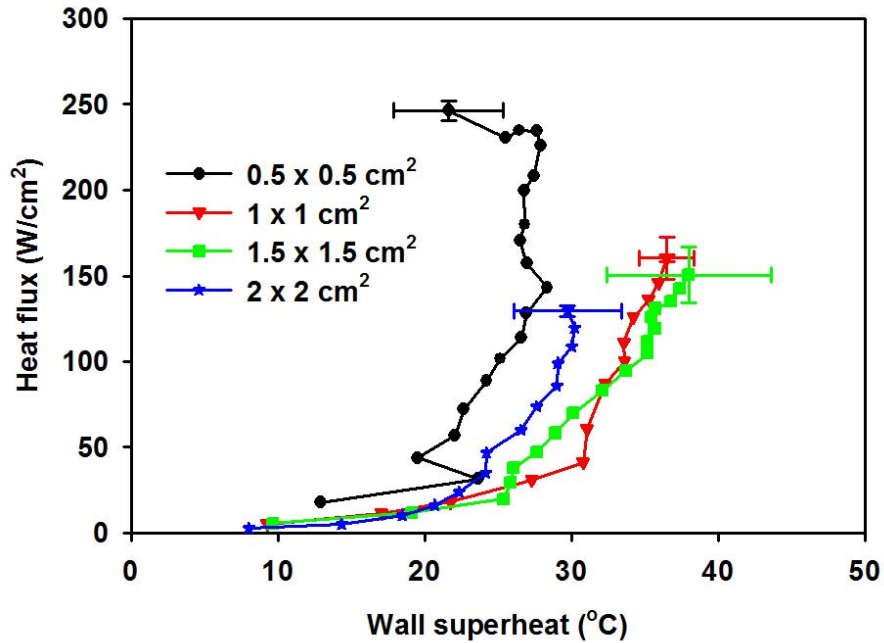


Fig. 4.14 Boiling curves on SiNW array coated-surfaces for different sizes of the heaters

The boiling curves of $\sim 60 \mu\text{m}$ height SiNW array-coated surfaces with four different sizes of heaters are shown in Fig. 4.14. The bubbling images of these heaters at CHF condition are shown in Fig. 4.15.

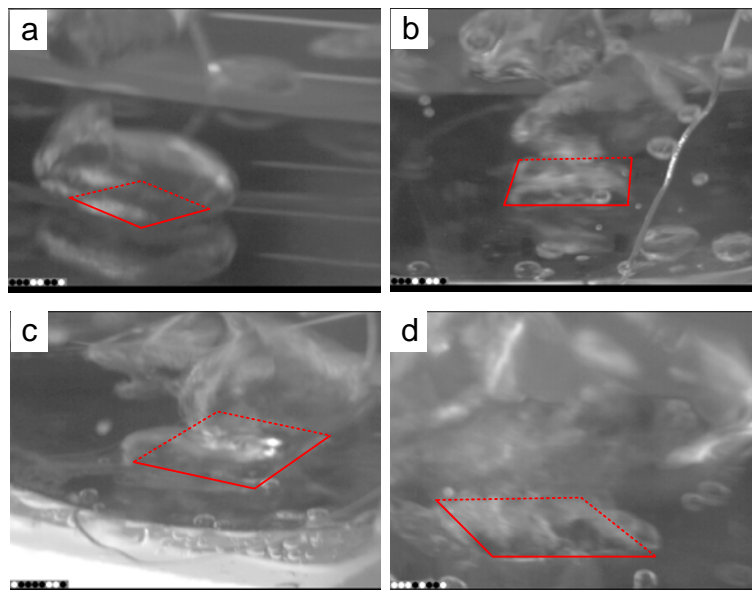


Fig. 4.15 Boiling images at CHF condition for different sizes of heaters (a) 0.5 x 0.5 cm² (b) 1 x 1 cm² (c) 1.5 x 1.5 cm² and (d) 2 x 2 cm². Note that the edges of heaters are outlined.

Note that only one vapor column/mushroom is present for all the sizes of the heaters at CHF condition. The CHF and HTC for heater sizes of 0.5 x 0.5, 1 x 1, 1.5 x 1.5 and 2 x 2 cm² after subtracting heat conduction losses (Eq. (4.11)) are shown in Table 4.1. The CHF increases as heater size reduces. The obtained highest CHF and HTC of 223.90 ± 6.60 W/cm² and 9.99 ± 1.62 W/cm²K, respectively, on a heater size of 0.5 x 0.5 cm² are among the peak values reported in boiling heat transfer.

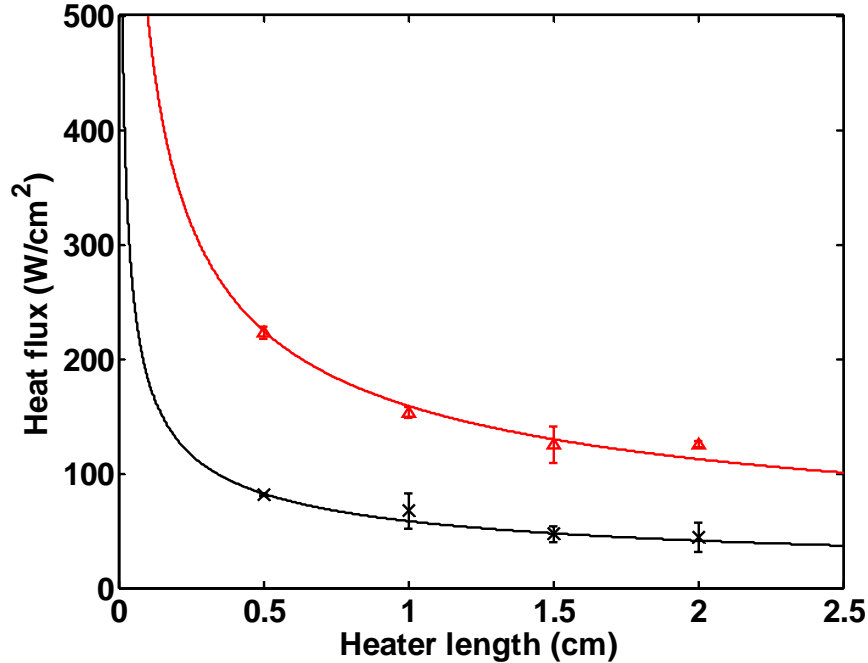


Fig. 4.16 CHF versus heater length where the red open triangle marks are experiment results of SiNW array-coated surfaces of four different sizes of heaters and the red solid curve is the theoretical prediction of Eq. (4.1) using the Helmholtz wavelength as a control variable assuming an area ratio (A_v/A) of 0.15 and the dark cross points and are the results of plain Si surface and the dark solid curve is the theoretical prediction of Eq. (4.1) assuming an area ratio (A_v/A) of 0.0055.

The corresponded percentage of the heat conduction losses of the CHF for various sizes of the heaters are also shown in Table 4.1. The conduction losses for various sizes of heaters are about 6.26 ± 1.60 % of the CHF. The CHF versus heater size along with a theoretical prediction is shown in Fig. 4.16. The red open triangle marks are experimental results of SiNW array-coated surfaces of four different sizes of heaters. The red solid curve is the theoretical prediction of Eq. (4.1) using the Helmholtz wavelength as a control variable assuming an area ratio (A_v/A) of 0.15. For a heater that only accommodates one vapor column/mushroom, the area ratio (A_v/A in Eq. (4.1)) is not a constant ($\pi/16$) as in the original hydrodynamic models proposed by Zuber [17] and Lienhard and Dhir [18]. The value of area ratio should be dependent on the number of vapor stems in the macrolayer (see Fig. 4.1). As a result, the area ratio should be related to the

nucleation site density on the heater surface, which is unknown and adopted here as a fitting factor of prediction. It can be seen that the experimental results can qualitatively match the theory via assuming the Helmholtz wavelength equal to the corresponded heater size. It is therefore postulated that for heaters with only one vapor column presents on the surface, the size of the heater poses a critical wavelength resulting in the instability of vapor columns.

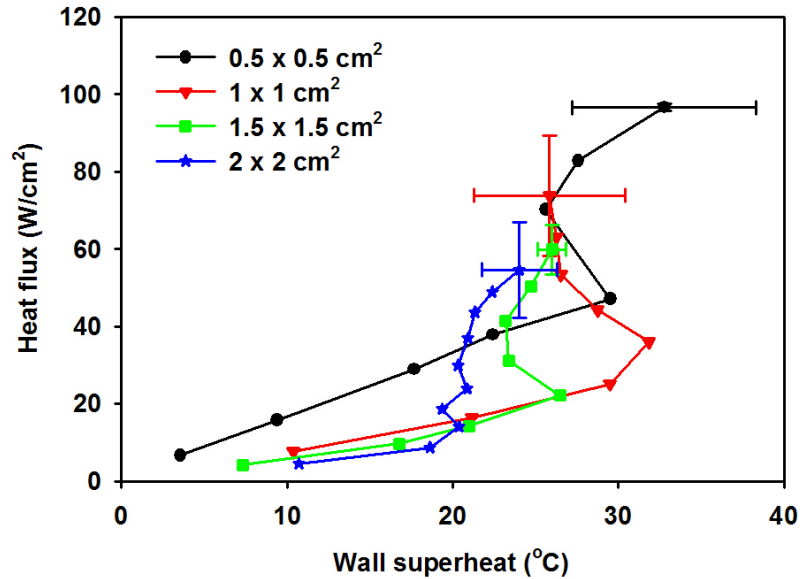


Fig. 4.17 Boiling curves on plain Si surfaces for different sizes of heaters

As a control experiment, the boiling curves for plain Si surfaces with corresponded heater sizes are shown in Fig. 4.17. The CHF and HTC for the heater sizes after subtracting heat conduction losses (Eq. (4.11)) are shown in Table 4.1. The obtained highest CHF and HTC are $81.48 \pm 1.71 \text{ W/cm}^2$ and $2.43 \pm 1.01 \text{ W/cm}^2\text{K}$, respectively, on a heater size of $0.5 \times 0.5 \text{ cm}^2$. The percentages of the heat conduction losses of the CHF are also shown in Table 4.1. The conduction losses for various sizes of heaters are about $14.40 \pm 3.41 \%$ of the CHF. Since the HTCs on the plain Si surfaces are smaller than that on the nanowire array-coated surfaces, the correspondingly higher conduction losses are observed on the plain Si surfaces. These values of CHF along with the theoretical prediction of Eq. (4.1) having an area ratio (A_v/A) of 0.055 for plain Si surfaces are also shown in Fig. 4.16 (dark cross points and dark solid curve, respectively). The CHF on the plain Si surface could also be matched by the hydrodynamic theory by assuming the Helmholtz wavelength equal to the heater length with a smaller area ratio of 0.055 as compared to the nanowire array-coated surfaces (see Fig. 4.16). The using of a higher area ratio for the nanowire array-coated surface is supported by that a larger nucleation site density is observed on the nanowire array-coated surfaces as compared to the plain Si surfaces. Since both the CHF on nanowire array-coated surface and plain Si surface could be matched by the hydrodynamic theory whereas higher CHF are obtained on the nanowire array-coated

surfaces, it indicates that the surface properties could affect the values of the resultant hydrodynamic limits presumably via the nucleation site density on the heater surface.

Based on the experimental results and their good agreement with the theoretical predictions of the hydrodynamic theory, we proposed a modified hydrodynamic model: For a heater which only accommodates one vapor column ($L < 2$ cm ($L < 8 L_c$)), the Helmholtz wavelength should be governed by the heater length and the area ratio (A_v/A) in Eq. (4.1) should be dependant on the nucleation site density on the heater surface. On the other hand, the models proposed by Zuber [17] and Lienhard and Dhir [18] are only applied for a surface where heater size effect on CHF is absent ($L > 8 L_c$).

Table 4.1 Summary of Experimental Results

Heater Size		0.5 x 0.5 (cm ²)	1 x 1 (cm ²)	1.5 x 1.5 (cm ²)	2 x 2 (cm ²)
SiNW	CHF (W/cm ²)	223.90 ± 6.60	150.67 ± 12.57	124.85 ± 16.27	125.52 ± 3.49
	HTC (W/cm ² K)	9.99 ± 1.62	4.10 ± 0.25	3.21 ± 0.64	4.18 ± 0.73
	Cond. Loss (%)	7.03	7.96	5.80	4.26
Plain Si	CHF (W/cm ²)	81.48 ± 1.71	67.40 ± 15.55	46.82 ± 6.49	44.22 ± 12.35
	HTC (W/cm ² K)	2.43 ± 1.01	2.58 ± 0.47	1.77 ± 0.29	1.80 ± 0.73
	Cond. Loss (%)	16.21	13.46	17.88	10.08

4.4 Conclusion

By studying pool boiling on the nanowire array-coated surfaces and plain Si surfaces, we have been able to identify the mechanism causing CHF on these two different kinds of surfaces. While the capillary force provided by the nanowire array greatly enhances the CHF's on the nanowire array-coated surface as compared to the plain Si surface, the resultant CHF is due to the hydrodynamic limit rather than the capillary limit. The CHF could be matched by the hydrodynamic theory via assuming the Helmholtz wavelength equals to the heater length with an area ratio of 0.15. For a surface that only accommodates one vapor column, the area ratio is not a constant as in the original hydrodynamic models [17, 18] but should be related to the nucleation site density on the heater surface. The obtained CHF of 224 ± 6.60 W/cm² on the nanowire array-coated surface of a heater size of 0.5 x 0.5 cm² is among the highest values reported in boiling heat transfer. The effect of heater size on CHF has been observed on the heater with a heater length smaller than 8 times of the capillary length (~ 2 cm). The effect of heater size is to increase the CHF as heater size reduces, which is similar to the phenomena observed in previous studies [18, 19, 36, 75, 76]. Nevertheless, the underlying physics of the heater size effect is because of the modification of the Helmholtz wavelength as a result of changing the heater size,

instead of edge effect [76] or the confinement effect [18] induced from the reduction of heater size.

Therefore, when applying the hydrodynamic theory on a heater that can only accommodate one vapor column, the Helmholtz wavelength is governed by the heater size as opposed to the intrinsic Taylor wavelength as in the hydrodynamic models for a infinite heater proposed by Zuber [17] and Lienhard and Dier [18].

Corresponding studies on the plain Si surface also exhibits a similar trend on the heater size dependence of CHF. The CHF on the plain Si surface could also be matched by the model based on the hydrodynamic theory assuming the Helmholtz wavelength equal to the heater length with a smaller area ratio of 0.0055 as compared to the nanowire array-coated surfaces. This suggests that the CHF on the plain Si surface are also due to the hydrodynamic limit instead of the wettability limit as argued by Dhir and Liaw [20] and Kandlikar [39] for a poor wetting surface. The higher nucleation site density on the nanowire array-coated surface is indirectly supported by the video observation on the nanowire array-coated surfaces.

Since both the CHF on nanowire array-coated surface and plain Si surface could be matched by the hydrodynamic theory whereas higher CHF are obtained on the nanowire array-coated surfaces, it indicates that the surface properties could affect the values of the resultant hydrodynamic limits possibly through the nucleate site density.

Based on the experimental results and their good agreement with the theoretical predictions of the hydrodynamic theory, a modified hydrodynamic model is proposed: For a heater which only accommodates one vapor column ($L < 8 L_c$), the Helmholtz wavelength should be governed by the heater length and the area ratio (A_v/A) in Eq. (1) should be dependant on the nucleation site density on the heater surface. On the other hand, the models proposed by Zuber [17] and Lienhard and Dhir [18] are only applied for a surface where heater size effect on CHF is absent ($L > 8 L_c$).

This hypothesis seems to resolve the current controversy on the leading mechanisms of CHF on various surface conditions. More experiments on different kinds of surfaces need to be conducted to verify the hypothesis.

Chapter 5 Enhancing Thermal Conductance in Heat Pipes

5.1 Introduction

Heat pipe performance is evaluated mainly on the basis of two parameters: the maximum heat dissipation and the thermal conductance. Both these parameters are strongly dependent on the performance of the evaporator section. Evaporator wicks in state-of-the-art heat pipes are made of sintered copper particles yielding a bi-porous structure. Heat pipe performance at room temperature is limited mainly by two phenomena: capillary limit and boiling limit. In sintered copper wicks, the twin goals of increasing heat flux and increasing thermal conductance are in conflict. The increase of capillary suction-driven mass flow rate by having higher wick structure also increases the point-point contact between particles, which reduces thermal conductance. The current understanding of the performance of particle structures [79] is that at low applied heat fluxes, the wick is saturated with fluid, and evaporation occurs at the liquid-vapor interface at the top of the wick, leading to a low observed thermal conductance. The dominant resistance is due to the small area of liquid film of thickness of the order of a few microns, where the majority of heat transport towards the interface occurs [80-82]. For thick wicks (> 1 mm), the effective conductivity of the porous medium may dominate at low applied heat flux. At higher applied heat fluxes, there is increased flow drag associated with increased mass flux through the porous medium. In order to supply the increased capillary pressure necessary to sustain the flow, the liquid recedes into the smaller pores of the matrix. Thermal resistance through the porous matrix is reduced due to the recession of the liquid to a lower level in the wick structure. Recession of the liquid level to smaller pores also exposes a larger area of thin liquid film, thus increasing the thermal conductance; neglecting this effect leads to an under prediction of the effective conductance of the wick [11]. Liquid supply to the evaporating film occurs through large pores which offer lower flow resistance. The capillary limit occurs when liquid drag exceeds the capillary suction generated by the small pores. For a given particle size, there is likely an optimum wick thickness beyond which the particle-particle contact dominates the resistance [43].

While particle structures have been extensively studied, alternative morphologies, such as micro pin-fin arrays can be fabricated with great control to create a perfectly bimodal pore size distribution using standard microfabrication techniques. Pore size can be much smaller than currently achieved with copper powder, and is controllable with micron-scale resolution. Cylinder arrays also have the advantage of creating a parallel resistance with the low-conductivity liquid, enabling estimation of thermal conductivity of the solid matrix with high accuracy through knowledge of the porosity.

The primary feature of the wicks investigated is shown in Fig. 5.1. The large number of menisci formed in-between the micro pin-fins provide a large surface area for liquid film, enhancing thermal conductance. At the same time, these menisci provide a large capillary pressure which generates high liquid mass flow rate, with reduced drag due to the presence of large microchannels.

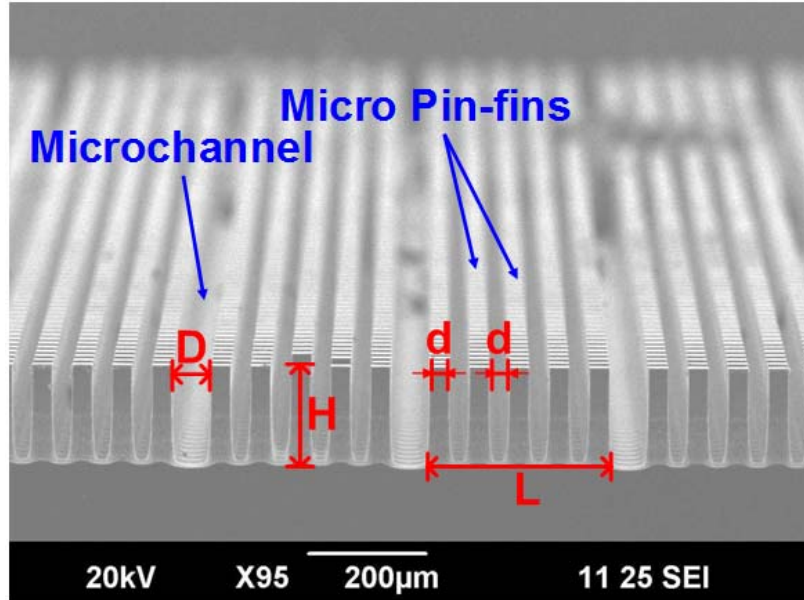


Fig. 5.1 SEM image of cross-section of the evaporator geometry, showing array of pin-fins with periodic microchannels.

Fig. 5.2 shows a schematic of the micro pin-fin wick structure and its corresponding thermal resistance network. In operation, heat is applied at the bottom of the solid wall and goes through two passages. The passage consisting of a bulk liquid has a much larger thermal resistance than that of the passage consisting of a solid and a thin liquid film. Therefore, the majority of the heat travels through the passage consisting of the solid and the thin liquid film. As a result, the wick thermal resistance can be approximated as

$$R_{wick} \approx R_s + R_{film} + R_i \quad (5.1)$$

where R_s , R_{film} and R_i are thermal resistance of the solid pin-fin, thermal resistance of the thin liquid film near the solid wall and interfacial thermal resistance, respectively.

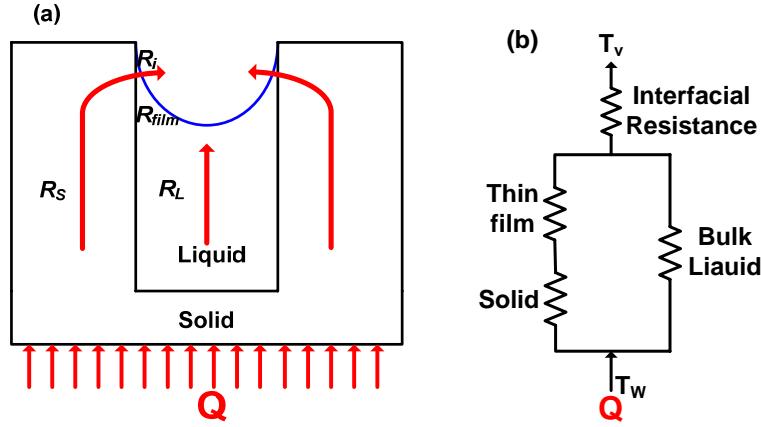


Fig. 5.2 (a) The micro pin-fin wick structure and (b) its corresponding resistance network.

The thermal resistance of the solid part is equal to:

$$R_s = \frac{H}{k_s(1-\phi)A} \quad (5.2)$$

where H is the wick height, ϕ is the porosity, k_s is the solid wall thermal conductivity and A is the total area of the wick structure.

A schematic of a thin liquid film near the wall of the micro pin-fin is shown in Fig. 5.3. The resistance of the thin liquid film is approximated as:

$$R_{film} = \frac{\delta}{k_l N(4dL_{film})} \quad (5.3)$$

where δ is the film thickness, N is the total number of the pin-fins, d is the edge length of the pin-fin and L_{film} is the extension of the thin liquid film. The total number of the pin-fins (N) is related to the porosity and the total area as

$$Nd^2 = (1-\phi)A \quad (5.4)$$

Substituting Eq. (5.4) into Eq. (5.3), one obtains

$$R_{film} = \frac{d^2}{(1-\phi)A} \frac{\delta}{k_l(4dL_{film})} \quad (5.6)$$

Meanwhile, the interfacial thermal conductance has been derived (see Eq. (3.26)). In general, this interfacial thermal resistance is much smaller than the thin film thermal resistance (R_{film}) and the solid thermal resistance (R_s) and could be neglected. Therefore, the dominant resistance in the wick is due to the small area of the liquid film of thickness of the order of a few microns, where the majority of heat transport towards the interface occurs.

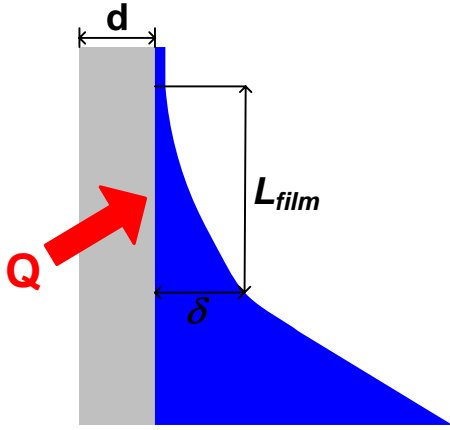


Fig. 5.3 A schematic of a thin liquid film near a wall

The thin liquid film near the solid wall can be divided into three regions: (1) Non-evaporating thin film (2) Transition region and (3) Intrinsic meniscus as shown in Fig. 5.4. In the non-evaporating thin film region, vapor pressure is higher than liquid pressure due to the presence of the disjoining pressure (P_d):

$$P_v = P_l + P_d \quad (5.7)$$

The disjoining pressure is a result of the long range attraction-dispersion force between solid and liquid molecules. For a non-polar molecule, the disjoining pressure can be modeled as [16, 83]

$$P_d = \frac{A}{\delta^3} \quad (5.8)$$

where A is the Harmaker constant and δ is the film thickness. The effect of disjoining pressure becomes significant as the film is thinned down to tens of nanometers, which causes a large pressure difference between liquid and vapor given that a thin liquid film is absorbed on the solid wall without evaporation. In the transition region, both the capillary pressure and disjoining pressure contribute to the difference between vapor and liquid pressure:

$$P_v = P_l + P_c + P_d \quad (5.9)$$

Meanwhile, in the intrinsic region, the effect of disjoining pressure becomes insignificant and the vapor pressure is higher than the liquid pressure primarily due to the curvature effect:

$$P_v = P_l + P_c \quad (5.10)$$

As mentioned in the previous section, the thin film near the solid wall is the dominant thermal resistance in the wick structure. Besides considering the effect of the steady state thermal resistance on the energy transport, we also need to consider the consequence of evaporation suppression due to the presence of the disjoining pressure and the capillary pressure on the

transient energy transport. It follows a similar analysis in Section 2.1, the Kelvin's equation due to the presence of the capillary and disjoining pressures becomes:

$$P_{ve} = P_{sat}(T_l) \exp\left[\frac{-(\sigma/r_e + A/\delta^3)}{\rho_l RT_l}\right] \quad (5.11)$$

Eq. (5.11) indicates that the equilibrium vapor pressure at the meniscus is smaller than its saturation pressure due to the effect of the capillary pressure and the disjoining pressure. Therefore, under a constant pressure condition, liquid must be superheated.

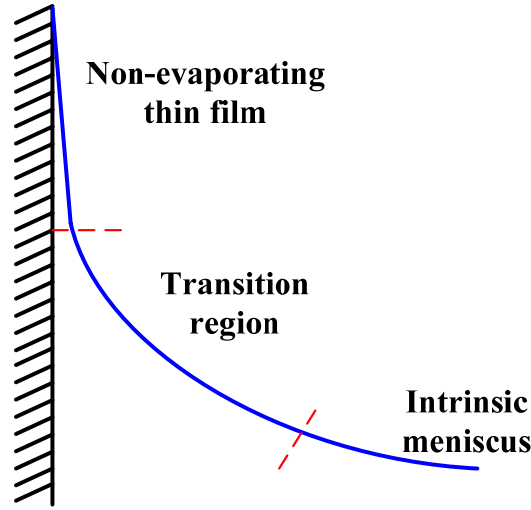


Fig. 5.4 The meniscus at the interline region

The amount of superheat could be again obtained by the Clausius equation (see Section 2.1) as

$$T_{le} - T_{sat}(P_l) = \frac{T_{sat}(P_l)}{\rho_v h_{lv}} \left(\frac{\sigma}{r_e} + \frac{A}{\delta^3} \right) \quad (5.12)$$

Eq. (5.12) indicates that a superheat is required for liquid-vapor evaporation due to the result of curvature and dispersion force. The range where the disjoining pressure (the extension of the transition region away from the wall) is important is seldom beyond one hundred nanometers [83]. For a wick structure having a characteristic length scale on the order of tens of microns, the effect of the disjoining pressure on evaporation suppression is not significant. Under this condition, the above equation can be further simplified as

$$T_{le} - T_{sat}(P_l) = \frac{\sigma T_{sat}(P_l)}{\rho_v h_{lv} r_e} \quad (5.13)$$

Therefore, a similar equation is obtained as the one describing the superheat required for vapor bubble formation inside a liquid pool (Eq. (2.10)). The effect of evaporation suppression can be

further clarified by relating the equilibrium radius of curvature to the viscous pressure drop of fluid flow through a porous medium:

$$\frac{\sigma}{r_e} = \frac{\mu_l \dot{m}_l l}{\rho_l \kappa A_c} \quad (5.14)$$

Substituting the value of r_e in Eq. (5.14) and the correlation of permeability (κ) in Eq. (3.6) into Eq. (5.13), one obtains

$$T_{le} - T_{sat}(P_l) = \frac{T_{sat}(P_l)}{\rho_v h_{lv}} \left(\frac{\mu_l \dot{m}_l l}{\rho_l A_c} \right) \left(\frac{125(1-\phi)^2}{d^2 \phi^3} \right) \quad (5.15)$$

where $\dot{m}_l = Q/h_{lv}$. Therefore, for a given power and a constant porosity (ϕ), the required superheat is inversely proportional to the square of the pore size ($\Delta T \propto 1/d^2$). Fig. 5.5 shows a variation of superheat corresponding to various pore sizes for applied powers of 100 W and 30 W, respectively. As can be seen from Fig. 5.5, the effect of evaporation suppression is significant, especially at the condition with a large applied power. This indicates that there must have certain amount of power being used to superheat the liquid transiently before its temperature reaches the required superheat at the equilibrium condition. As a result, the total effective thermal resistance to heat flow has significant components due to suppression of evaporation and conduction in the thin liquid film.

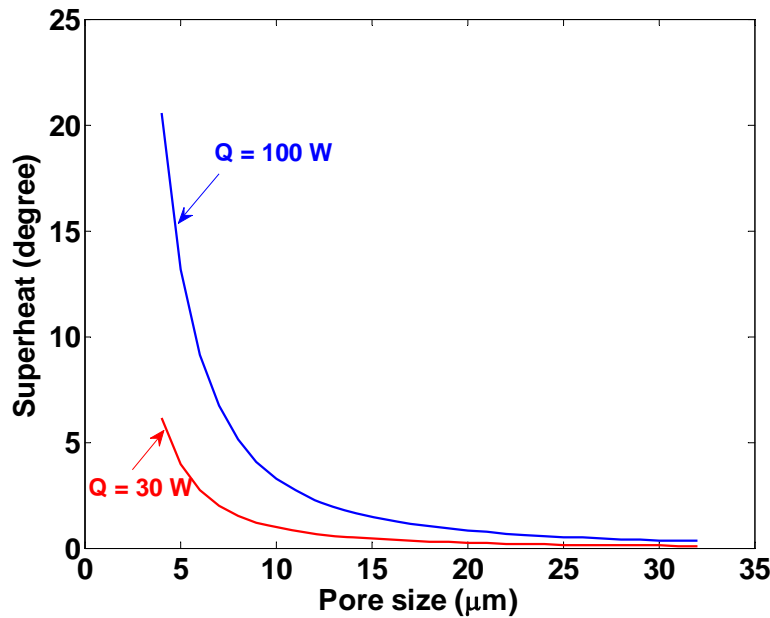


Fig. 5.5 Superheat versus pore size according to Eq. (5.15) for water at one atmosphere under saturation condition with $A_c = 2 \times 10^{-6} \text{ m}^2$, $l = 1 \text{ cm}$, $\phi = 0.75$.

Wayner and co-workers [84-86] have evaluated the evolution of the thin liquid film set up by the combined effects of disjoining pressure and surface tension. The formation of an extended meniscus by a completely wetting liquid in contact with a bulk liquid reservoir and a vertical surface is shown in Fig. 5.6. The gradient in the dispersion force and the surface curvature create a hydrodynamic pressure gradient that sucks liquid from the bulk reservoir towards the interline region, where evaporation occurs. The results of numerical [87, 88] and experimental work [89] indicate that the curvature attains a peak value in the interline region before attaining a nearly constant value in the intrinsic meniscus region. The dispersion force decreases as film extends from the transition region to the intrinsic meniscus region. The majority of heat transfer occurs at the thinnest part of the liquid film at the intersection of transition and intrinsic meniscus regions. It is noted by Potash and Wayner [84] that as the heat flux increases, the increased flow rate causes curvature which results in an increase of contact angle. This is contradictory to what happened in a confined channel where contact angle reduces as heat flux increases. This contradiction could be clarified as follows: First, due to the transition of the curvature of the meniscus at the interline region, two contact angles can be defined: (a) microscopic contact angle (θ_μ) at the transition region and (b) apparent contact angle (θ_a) at the intrinsic region. Fig. 5.7 shows schematically the variation of the contact angles corresponding to two different applied powers of 30 W and 100 W, respectively. Second, as the applied power increases, the balance between capillary pressure and viscous pressure drop (Eq. (5.14)) dictates that equilibrium radius of curvature must reduce to accommodate a higher flow rate. Therefore, the microscopic contact angle increases as heat load rises due to a larger curvature, which is similar to the argument of Potash and Wayner [84].

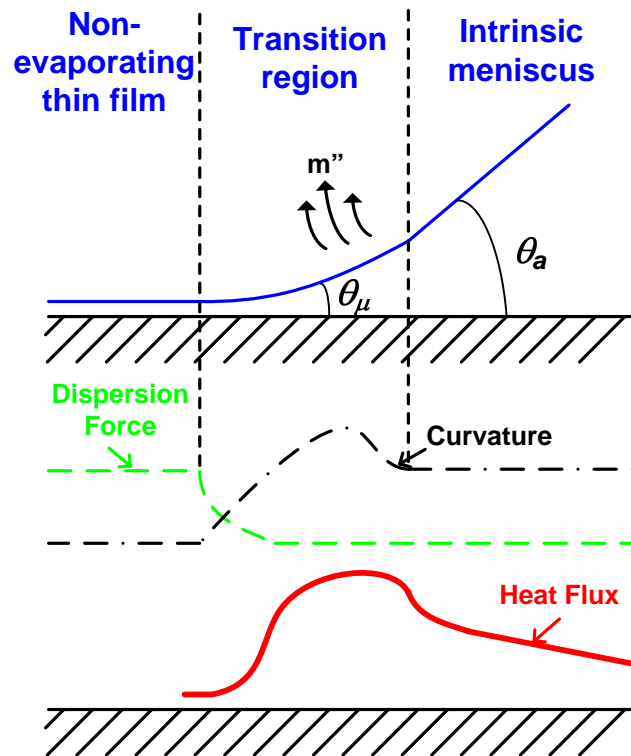


Fig. 5.6 The extended meniscus on a flat surface

On the other hand, the apparent contact angle is confined by the geometry (see Fig. 5.8), which follows

$$r_e = \frac{W}{2 \cos \theta_a} \quad (5.16)$$

Following the same line of reasoning, equilibrium radius of curvature must reduce to accommodate a higher flow rate, which results in a reduction of the apparent contact angle due to the geometry confinement. Therefore, as the applied power increases, it will display an increase of the microscopic contact angle (θ_μ) and a reduction of the apparent contact angle (θ_a) as shown in Fig. 5.7 for a confined channel.

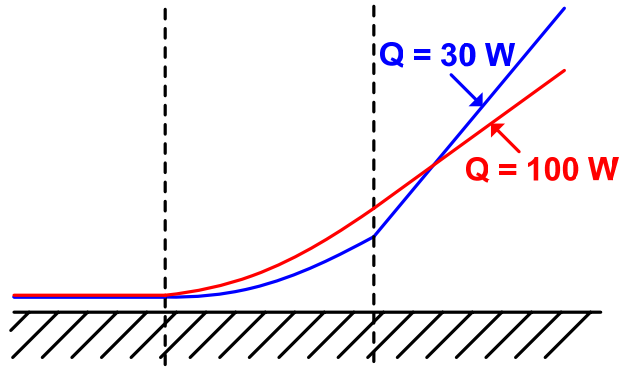


Fig. 5.7 Variation of contact angles corresponds to two different heat loads.

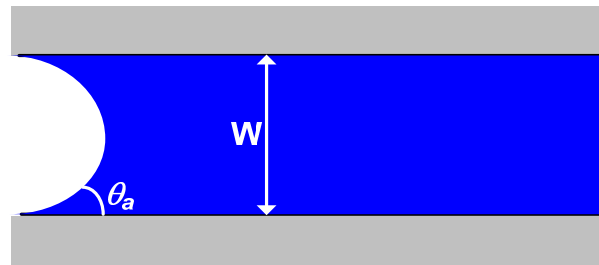


Fig. 5.8 Confinement of the apparent contact angle by the walls of micro pin-fins

5.2 Experimental Approach

The primary feature of the wicks investigated is shown in Fig. 5.1. The wicks are fabricated in the form of parallel microchannels of width D and depth H separating arrays of micro pin-fins. The wick has pin-fins of diameter d and pore sizes of d are arranged in an inline array of width L and porosity ϕ .

Wicks of area $2 \times 4 \text{ cm}^2$ are generated by lithographically defining features on a 4" diameter silicon wafer using a photomask on a GCA wafer stepper lithography system. The exposed and developed wafer is then etched via deep reactive-ion etching (DRIE) to generate deep trenches in the range 100-200 μm , depending on etching time (see Fig. 5.9 (a-c)). The geometrical

parameters of the wick such as pore size are well-defined down to a resolution of 1 μm and can be uniformly varied without requiring recourse to estimation based on particle size etc. The exact dimensions formed after etching are measured using a Scanning Electron Microscope.

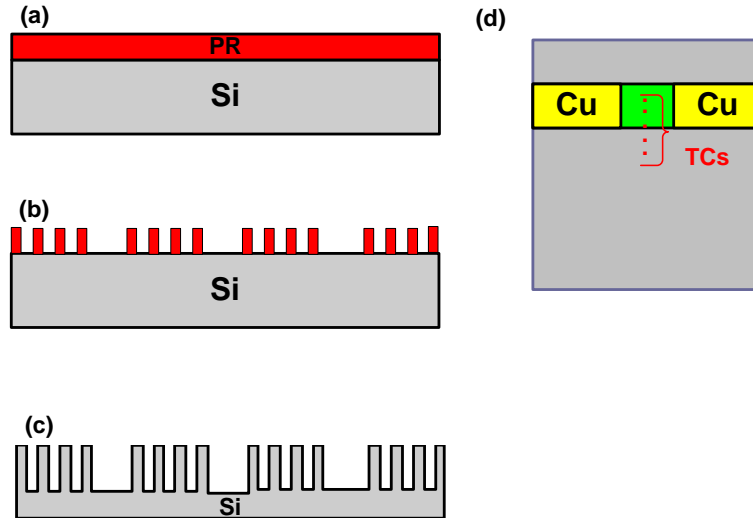


Fig. 5.9 Sketch of fabrication process used to generate the wick with microchannels and micro pin fins.

A similar heater as the one in pool boiling is used to study the wick performance (Fig. 5.9 (d)). An array of T-type thermocouples spaced 2 mm apart are affixed to the heater using high conductivity epoxy ($k \sim 2.02 \text{ W/m-K}$).

In addition, a wick structure with cavities in the pin-fin arrays was generated to initiate boiling at a lower wall temperature. The fabrication procedure is shown schematically in Fig. 5.10: (a) A PR layer is coated and patterned on a Si substrate. (b) Trenches in Si substrate are etched by DRIE. (c) Another layer of PR is coated and patterned on the substrate. (d) The microchannels and micro pin-fin arrays are etched by DRIE etching (e) Removes the PR layer. A wick structure with cavities in-between the micro pin-fin arrays can be obtained accordingly. Fig. 5.11 shows the images of the wick with cavities and pin-fins (Fig. 5.11 (a & b)) compared to the wick with only pin-fins (Fig. 5.11 (c & d)). The cavities have a diameter of $\sim 60 \mu\text{m}$ and a depth of $\sim 100 \mu\text{m}$. The height of the pin-fins is $\sim 150 \mu\text{m}$.

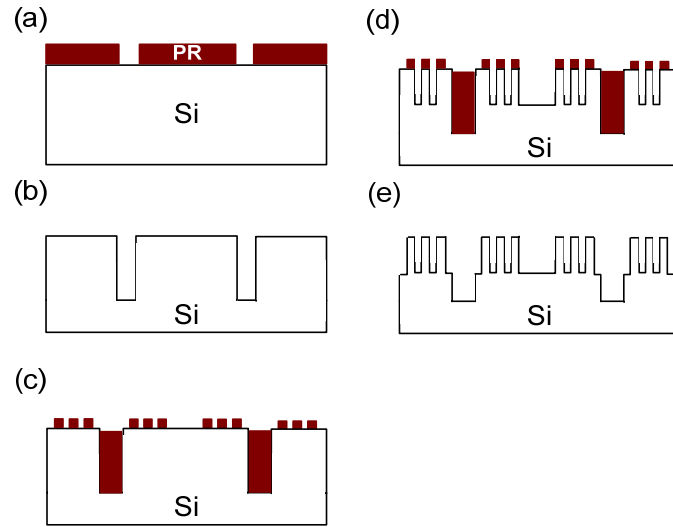


Fig. 5.10 A schematic of fabrication process used to generate a wick with pin fins and cavities

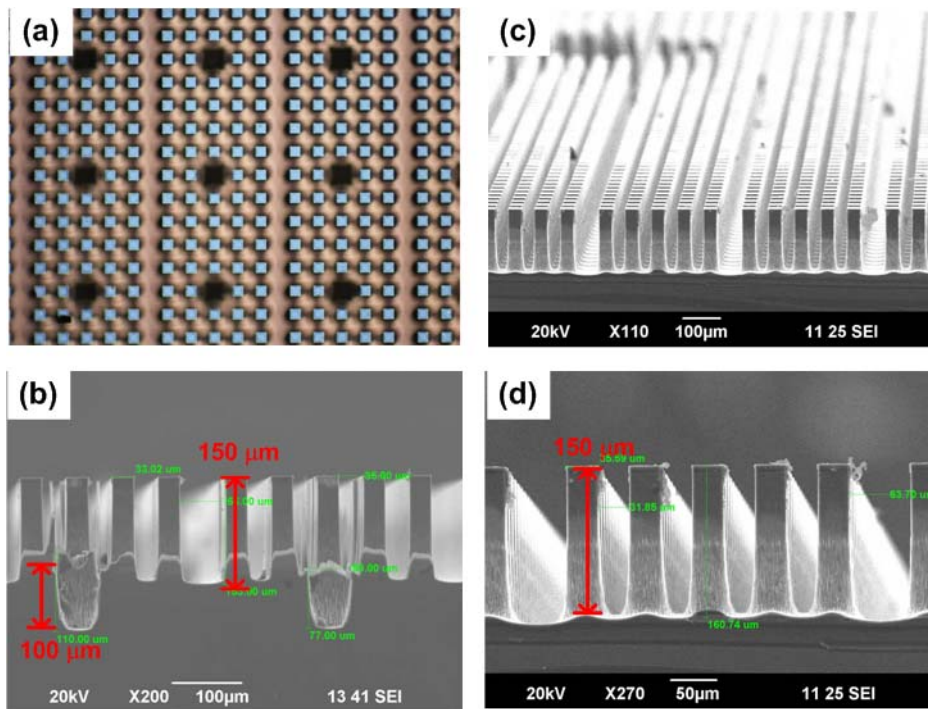


Fig. 5.11 Comparison of a wick having cavities and pin fins (a) top view (b) cross-sectional view, and a wick with only pin fins (c) top view (d) cross-sectional view

5.3 Experimental Setup

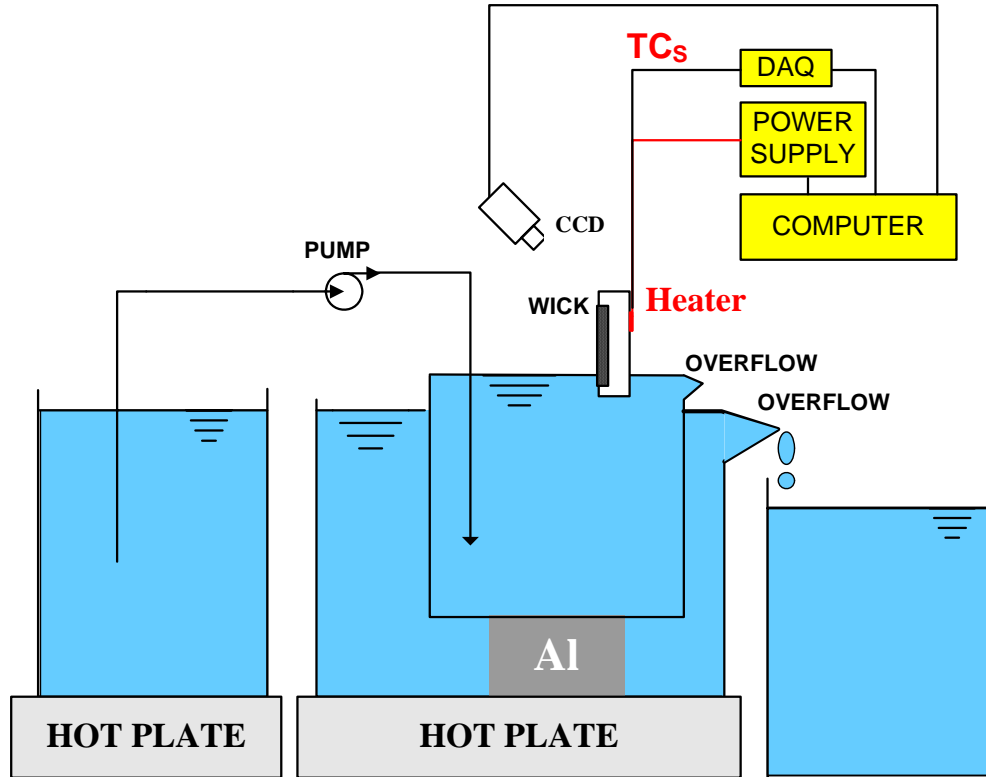


Fig. 5.12 Experimental apparatus used to measure evaporative heat transfer

The experimental system for evaluating the performance of the wick is shown in Fig. 5.12. It consists of a reservoir for liquid supply, a fluid pump (L/S Brushless Digital Drives, Masterflex), an data acquisition system (Agilent 34970A), a power supply (Agilent N5750A), a high speed CCD for recording images (Fastec Inline Model 1000, Fastec Imaging) and the test sample suspended at known height from the liquid pool. The temperature of the reservoir is kept constant against heat losses by immersing the reservoir in an external tank maintained at 100 °C. Thermocouples (T type, Omega Engineering Inc.) monitor the temperatures of the sample surface and water reservoirs. The experiments are performed with the wick in a vertical orientation. This represents the most severe operating condition, and also ensures that the wick is not flooded with liquid, but sucks up as much liquid as is necessary. The liquid level in the pool is maintained by using two overflow systems. Thus, the distance traveled by liquid from the pool surface to the heater remains constant during the experiment ($L_{wicking} \sim 0.5$ cm). After degassing the water via boiling the water for at least 15 minutes, power is applied in regular increments while simultaneously measuring temperatures at the center of the heater. The dominant mode of heat loss is by conduction from the heater through the silicon substrate to the liquid reservoir. To estimate this, the temperatures along the substrate were record. The conduction loss was quantized using Eq. (4.11)

$$q_{cond} = kA_c \frac{T_{edge} - T_{ref}}{x} \quad (4.11)$$

where T_{edge} is the temperature at the edge of the heater and T_{ref} is the measured temperature at a distance x (~ 2 mm) away from the heater, k is the thermal conductivity of Si (130 W/m-K) and A_c is the cross-sectional area of the substrate (~ 2 cm \times 500 μ m). The result of the conduction loss for the sample having parameters ($d = 32$ μ m, $D = 60$ μ m, $H = 150$ μ m, $L = 308$ μ m, see Table 5.1) under various applied heat fluxes is shown in the Appendix. At the peak heat flux for the sample, the conduction loss is about 10 % of the applied heat flux. The real wall temperature (T_w) is derived as $T_w = T_{TC} - \frac{q''\delta}{k}$ as in section 4.2.2, where T_{TC} is the temperature measured by the thermocouples and δ is the thickness of the Si substrate. The uncertainties of the measured heat fluxes, wall temperatures and the thermal conductances (defined by the slopes of the curves) are resulted from the accuracies of the power supply, the data acquisition system and the resolution of the thermocouples. A detailed uncertainty analysis for the evaporation experiments is also shown in the Appendix.

5.4 Results and Discussion

Table 5.1 shows the parameter space over which the experiments were performed. The microchannel widths were 30 μ m and 60 μ m, respectively, while the pin-fin diameter values of 4, 8, 16 and 32 μ m were studied. Multiple samples used for a given pore size are denoted by the pore size and an alphabet (Sample A, B, etc). In all cases, the porosity of the pin fin array was fixed at $\phi = 0.75$, thus ensuring that the effective thermal conductivity of the solid matrix, as approximated by a parallel resistance model (see Eq. (3.16)), remained nearly constant.

Table 5.1 Various dimensions defining the wick geometry

Pin fin diameter d (μ m)	Microchannel Width D (μ m)	Microchannel depth H (μ m)	Pin fin array width L (μ m)
4	30	150	156
8	30	100,150,200	152
16	30	150	154
32	60	150	308

Fig. 5.13 shows the repeatability of the evaporation curve for the case of $d = 16$ μ m, $H = 150$ μ m for two different samples (sample A & B) with a wicking height ($L_{wicking} = 0.5$ cm). The data are repeatable for multiple experimental runs across and within samples, and show a linear variation

of temperature with applied heat flux, indicating a constant thermal conductance due to evaporation. For a given pin-fin diameter, conduction through the thin liquid film near the meniscus is the dominant resistance, and is responsible for the constant slope of the evaporation curve. Dry-out eventually occurs as the heat flux is increased to about 140 W/cm^2 , with the appearance of a visibly dry patch near the top of the heater, where liquid supply is first affected.

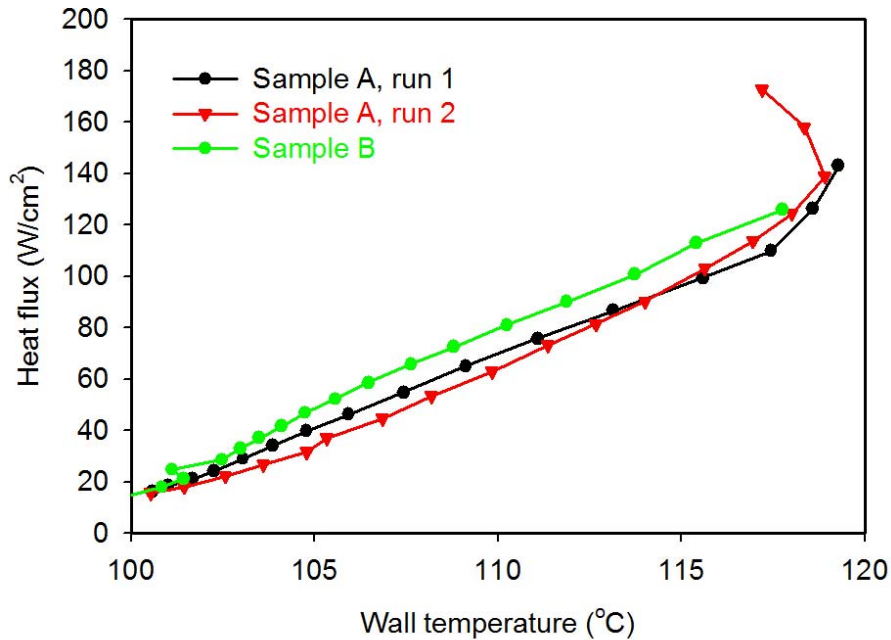


Fig. 5.13 Repeatability of data for two samples for $d = 16 \mu\text{m}$, $H = 150 \mu\text{m}$, $L_{wicking} = 0.5 \text{ cm}$.

As the liquid level in the microchannels recedes with increased heat flux, there is an additional area of thin liquid film on the bottom of the channels and between the pin-fins, which contributes to an increased heat transfer coefficient. As a result, as the heat flux is increased beyond the onset of dry-out, the temperature of the sample reduces over a finite range of heat flux. However, once the liquid supply in capillary limit is reached, i.e. the frictional drag in liquid flow through the microchannels is greater than the capillary pressure generated by the liquid menisci in the corners of the pin-fin base, complete dry-out occurs. The temperature of the wick starts rising significantly with applied heat flux, and the wick structure is no longer operational.

Fig. 5.14 presents data for the case where the height of the heater above the liquid pool ($L_{wicking}$) is varied from 0.5 to 2 cm. The results show that as drag is increased, the dry-out flux is reduced, with no apparent effect on the conductance. These results clearly demonstrate that bi-porous media, when designed suitably, can be used to increase the dry-out flux while maintaining high heat transfer coefficients.

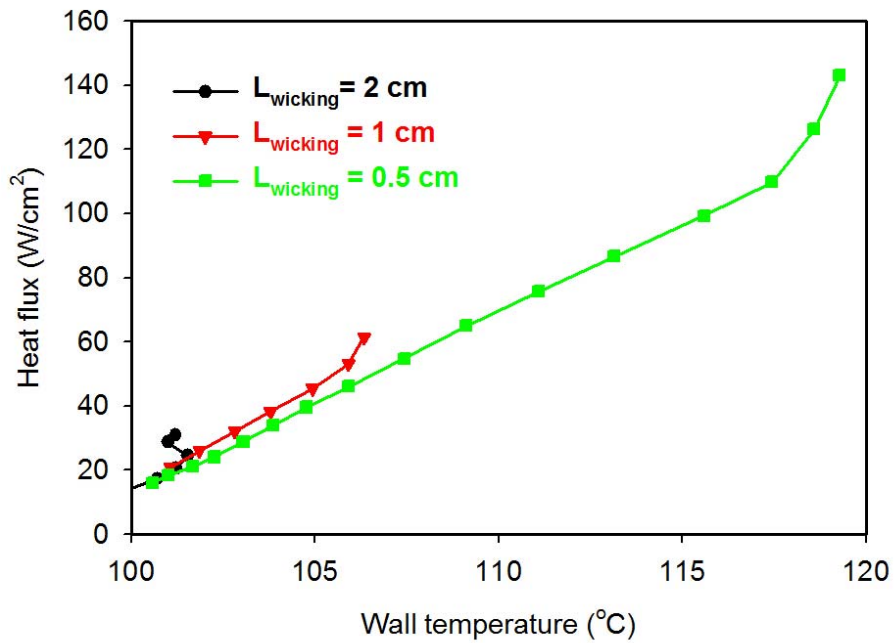


Fig. 5.14 Variation of dryout flux as a result of increase in wicking height ($d = 16 \mu\text{m}$, $H = 150 \mu\text{m}$).

The effect of increasing mass flow rate by increasing the height of the supply microchannels is illustrated in Fig. 5.15 for the case of the $8 \mu\text{m}$ pin-fin array. For microchannel depths of $H = 100$, 150 , and $200 \mu\text{m}$, the dry-out flux varies from $50.17 \pm 2.62 \text{ W/cm}^2$ to $110.66 \pm 5.62 \text{ W/cm}^2$; however, the slope of the curves remains the same until the onset of dryout. This is in agreement with the understanding that the overall thermal conductance is governed mainly by the extent of thin film around the menisci between pin-fins.

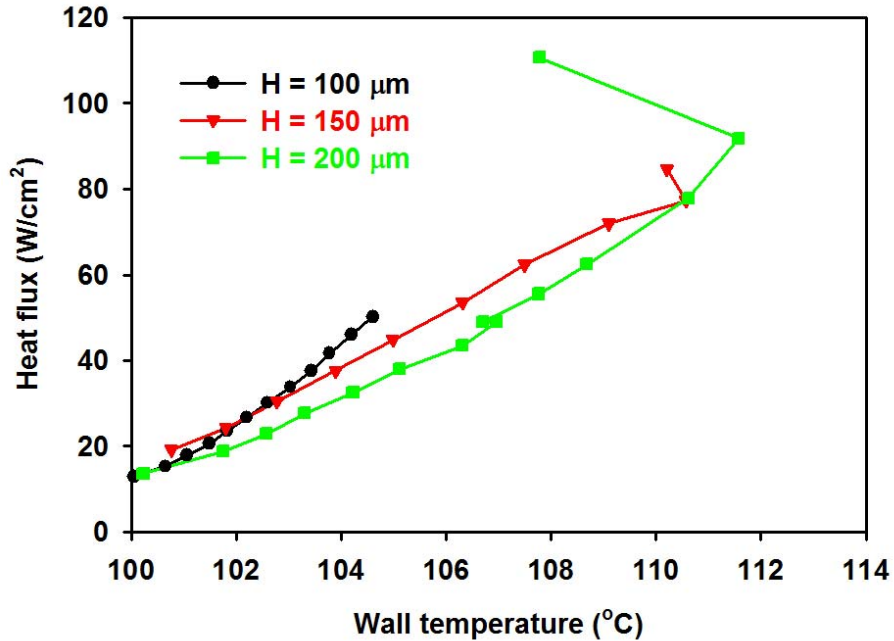


Fig. 5.15 Comparison of performance of evaporator geometries of different microchannel depths ($d = 8 \mu\text{m}$, $L_{wicking} = 0.5 \text{ cm}$).

Fig. 5.16 shows the effect of varying the pin fin diameter on the evaporation curve for channel depths of $150 \mu\text{m}$, and wicking height ($L_{wicking}$) of 0.5 cm . Four different pore sizes ($32 \mu\text{m}$, $16 \mu\text{m}$, $8 \mu\text{m}$ and $4 \mu\text{m}$) were studied. The thermal conductance (defined by the slope of the curve) and dry-out heat flux are shown in

Table 5.2. As the pore size is reduced from $32 \mu\text{m}$ to $16 \mu\text{m}$, an increase of conductance from 3.54 ± 0.01 to $5.42 \pm 0.03 \text{ W/cm}^2\text{K}$ is observed (see

Table 5.2). The enhancement of conductance is mainly due to the increase of thin area via a reduction of pore size and pin size (see Eq. 5.6). However, a reduction of conductance is observed when the pin and pore size are further reduced from $16 \mu\text{m}$ to $4 \mu\text{m}$ (see

Table 5.2 and Fig. 5.16). This reduction of thermal conductance as pore size reduces is mainly due to the effect of evaporation suppression discussed in Section 5.1. For the pore size scale in the range $4\text{-}32 \mu\text{m}$ at a given power of 40 W , Eq. (5.16) predicts the required superheat to be of the order of $8.2\text{-}0.1 \text{ K}$. In a situation at a larger heat flux, the required superheat may be considerably significant. As a result, as pore size decreases, in order to initiate evaporation, a larger fraction of the heat flux from the pin fin is used to superheat the liquid. Due to these two competing effect of increasing surface area via a reduction of the pore size and evaporation

suppression for small pores, there is an optimized pore size for the thermal conductance in evaporation heat transfer. The optimized pore size in the wick structure studied here is in-between 16 μm to 32 μm . Meanwhile, the dry out heat flux dissipated increases as the pore size increases ($d = 4 - 16 \mu\text{m}$). It indicates that the pressure drop due to liquid flow remains dominated by the permeability of the porous pin fin array.

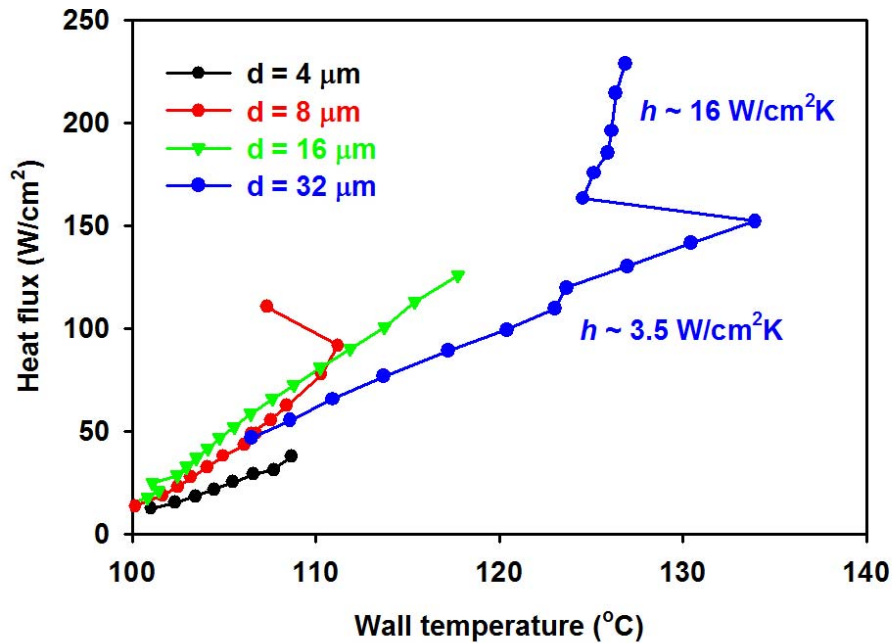


Fig. 5.16 Effect of pore size on evaporation curves ($H = 150 \mu\text{m}$, $L_{wicking} = 0.5 \text{ cm}$).

Table 5.2 Performance of evaporator geometries as a function of pore size (for $H = 150 \mu\text{m}$, $L_{wicking} = 0.5\text{cm}$)

d (μm)	Dryout flux (W/cm^2)	h ($\text{W}/\text{cm}^2\text{K}$)
4	37.9 ± 1.98	3.01 ± 0.01
8	110.7 ± 5.62	4.88 ± 0.01
16	125.8 ± 6.39	5.42 ± 0.03
32	228.8 ± 10.73	3.54 ± 0.01

For wick structure having small flow resistance ($D = 60$, $d = 32 \mu\text{m}$), operation at high heat flux corresponding to high wall temperature is observed (see blue line in Fig. 5.16). Thin film boiling is initiated at a wall temperature about $140 \text{ }^\circ\text{C}$. The onset of thin film boiling drastically enhances the conductance (defined by the slope of the curve), from an evaporative mode of $3.54 \pm 0.01 \text{ W/cm}^2\text{K}$ to a boiling mode of $16.28 \pm 1.33 \text{ W/cm}^2\text{K}$. The enhancement of conductance can be attributed to the following reasons: (1) Boiling in the pores of the pin fin array creates vapor bubbles that are constrained in the lateral direction, and are elongated vertically. The process of escape of constrained vapor bubbles from the pores of the pin fin array creates a thin liquid film through the entire height of the pin fin, instead of only in the region near the meniscus (see Fig. 5.17). As a result, the thin film area near the wall is greatly enlarged in the boiling regime compared to the evaporative regime given that a higher thermal conductance is observed in boiling regime. (2) Boiling is similar to a forced convection process (see Section 2.3). Vapor bubbles act as micro-pumps, which push hot liquid away from the heating surface and draw cold liquid to it. This agitation process could in principle significantly enhance thermal conductance. Consequently, a higher conductance is observed in the boiling regime. While the onset of nucleate boiling in wick structures is deprecated by heat pipe designers, since large bubbles may block liquid supply in sintered-particle wicks, presumably due to a large vapor transport resistance, the geometry considered in this study is such that liquid supply occurs in micro-channels while boiling would occur in the pin-fin array given that vapor and liquid transport paths are separated. As a result, boiling is not an operational limit in current study. In our experiments, the applied heat flux could be increased by 100 W/cm^2 beyond the onset of nucleate boiling, while having a temperature increase within 5 K . To use the advantage of the high heat transfer coefficient of boiling and reduce the superheat for a given heat flux, a wick structure with artificial cavities are created (see Fig. 5.11). The fabrication procedure of the wick structure was illustrated in Fig. 5.10. These cavities could in principle trap air/vapor inside them and initiate heterogeneous nucleation at a lower superheat. The experimental results comparing the wicks with and without cavities are shown in Fig. 5.18. For the micro pin-fin wick, in the evaporative regime, a conductance of $3.54 \pm 0.01 \text{ W/cm}^2\text{K}$ is observed while boiling occurs at $\sim 140 \text{ }^\circ\text{C}$, which enhances conductance to $16.28 \pm 1.33 \text{ W/cm}^2\text{K}$. For the wick with cavities, heterogeneous nucleation is observed at lower superheat resulted in a conductance of $9.02 \pm 0.04 \text{ W/cm}^2\text{K}$. For a given heat flux of $\sim 130 \text{ W/cm}^2$, a wall temperature of $\sim 120 \text{ }^\circ\text{C}$ is observed on the wick having cavities compared to a temperature of $\sim 130 \text{ }^\circ\text{C}$ on the wick with only pin fins. Consequently, artificial cavities created could successfully trigger heterogeneous nucleation and reduce wall temperature at a given heat flux.

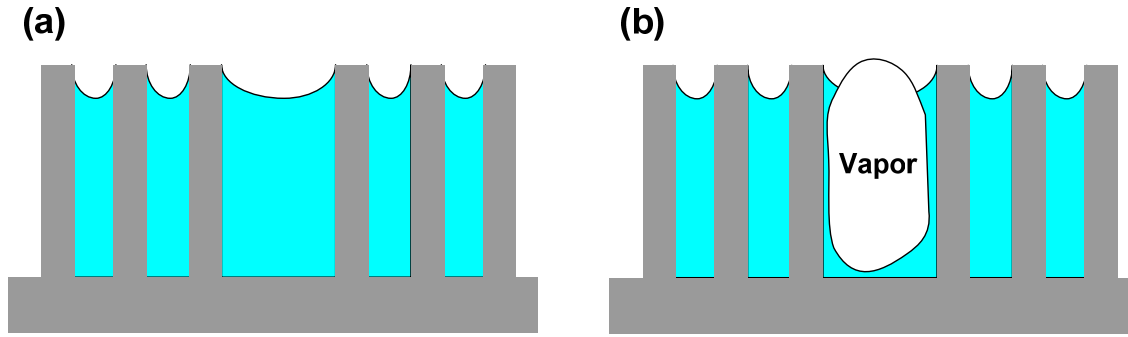


Fig. 5.17 Comparison of (a) evaporative and (b) boiling heat transfer in a micro pin fin array wick

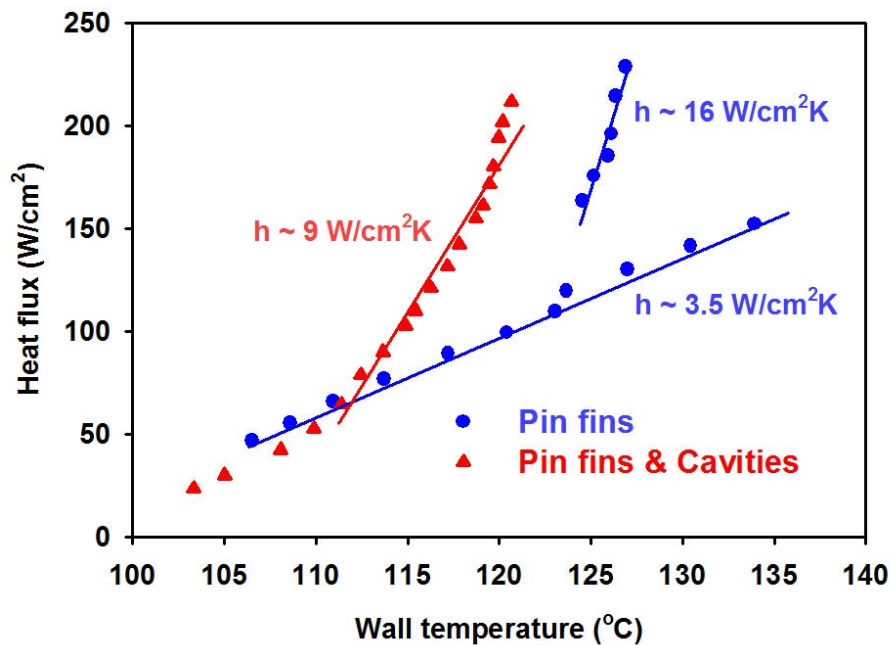


Fig. 5.18 Experimental results of a wick with pin-fins along (blue solid circle) and a wick with pin-fins and cavities (red solid triangle)

5.5 Conclusion

Experimental data are presented from a bi-porous wick consisting of pin-fin arrays and microchannels. A Heat flux of up to $228.8 \pm 10.73 \text{ W/cm}^2$ and a thermal conductance of up to $16.28 \pm 1.33 \text{ W/cm}^2\text{K}$ (defined by the slope of the curve) can be dissipated in the wick. To the best of our knowledge, this is the highest values reported in the evaporative heat transfer. As a

result of the competing effect of increasing surface area via reducing pore size and suppression of evaporation at small pore sizes, there is an optimized pore size for the evaporation heat transfer. The optimized pore size for the wick studied is in-between 16 μm and 32 μm . For wicks having small flow resistance, thin film boiling is observed at high wall temperature, which greatly enhance thermal conductance from it in evaporation regime. To use the advantage of high heat transfer coefficient of boiling, artificial cavities are created in the wick, which effectively trigger heterogeneous nucleation at a lower wall temperature. For a given heat flux, the wick with cavities successfully reduces wall temperature compared to a wick with only pin-fins.

Chapter 6 Conclusion and Future Work

6.1 Conclusion

In pool boiling, I report the enhancement of CHF and HTC using Si and Cu nanowire array-coated surfaces. The obtained CHF of $224 \pm 6.60 \text{ W/cm}^2$ on the Si nanowire array-coated surface is one of the highest reported values in boiling heat transfer. The enhancement of CHF is mainly contributed by a modification of surface properties by coating of these nanowire arrays on the surfaces. The technique employed for boiling enhancement is inexpensive and scalable, which could be practically applied in industries, such as, power plants and electronic cooling etc. Second, the mechanism causing CHFs on Si nanowire array-coated surfaces and plain Si surfaces has been identified. The CHFs on Si nanowire array-coated surfaces and plain Si surfaces are consistent with the predictions of hydrodynamic theory assuming corresponded nucleation site densities on each kind of surface. This suggests that the CHFs are eventually resulted from the pool hydrodynamics while the surface properties modify the corresponding hydrodynamic limits.

In the study of enhancing evaporative heat transfer in heat pipes, a hierarchical wick structure with multiple length scales that enhances dry-out heat flux and thermal conductance simultaneously has been demonstrated. This hierarchical wick structure is composed of a large microchannel array to reduce flow resistance and small pin-fin arrays to provide large capillary force. The enhancement of thermal conductance is achieved by the large number of menisci formed in-between the micro pin-fins. A thermal conductance of $16.28 \pm 1.33 \text{ W/cm}^2\text{K}$ and a dry out heat flux of $\sim 228.8 \pm 10.73 \text{ W/cm}^2$ were achieved by this design. While the onset of nucleate boiling in wick structures is deprecated by heat pipe designers, since large bubbles may block liquid supply in sintered-particle wicks, presumably due to a large vapor transport resistance, the geometry considered in this study is such that liquid supply occurs in microchannels while boiling would occur in the pin-fin array, thus separating vapor and liquid transport paths. As a result, boiling is not an operational limit in the wick. Artificial cavities are created to take the advantage of the large heat transfer coefficient of boiling. These artificial cavities successfully trigger heterogeneous nucleation, which results in a thermal conductance of $9.02 \pm 0.04 \text{ W/cm}^2\text{K}$ compared to an evaporation mode of $3.54 \pm 0.01 \text{ W/cm}^2\text{K}$ on a wick without cavities. At a given heat flux, the wick with cavities effectively reduce wall temperature compared to a wick with only pin-fin arrays.

Although, both the obtained CHFs in pool boiling and thermal conductances in heat pipes are still far below the predicted limits according to kinetic theory, I have able to identify the mechanisms causing the limits in boiling heat transfer and heat pipes. Such understandings could guide a new direction for further improving performance in boiling and evaporative heat transfer.

6.2 Future Work

6.2.1 Enhancing Thermal Conductance in Heat Pipes

Current heat pipes using evaporation as the dominant heat transfer mechanism unavoidably encounter a contradiction between increasing thermal conductance and increasing dry-out heat

flux simultaneously because one favors a shorter wick to reduce thermal resistance whereas the other favors a taller wick to accommodate a larger flow rate. In addition, with the thin liquid film surrounding the solid structure in a wick as the dominant thermal resistance, enhancing thermal conductance by increasing thin film area resulted from reducing pore size is again contradictory to the effect of suppression of evaporation for small pores. While the experimental results display an enhancement of thermal conductance using boiling heat transfer, it opens up a new direction for further improving the performance in heat pipes via circumventing all the aforementioned contradictions. The experimental result shows that a properly designed wick with a small vapor transport resistance could use boiling to enhance thermal conductance instead of causing dry-out in heat pipes. Heat transfer coefficient in boiling is mainly dependent on the bubble dynamics given that the active nucleation site density, the bubble releasing frequency and the bubble departure diameter are the three most important factors. With boiling as the dominant heat transfer mechanism, both the thermal conductance and dry-out heat flux could be manipulated independently in heat pipes by manipulating bubble dynamics to enhance thermal conductance while maintaining a moderate flow rate at the same time. Furthermore, once vapor bubbles formed in the wick, the thin film area is govern by the contact area between vapor bubbles and wick structure. This circumvents the dilemma of increasing thermal conductance via reducing pore size and evaporation suppression for small pores as well.

Therefore, to further enhance thermal conductance of heat pipe, one wish to use the advantage of high heat transfer coefficient of boiling. A wick structure having re-entrant cavities is proposed accordingly (see Fig. 6.1). The advantages of this re-entrant cavities wick are: (1) Because of the shape of these re-entrant cavities, hydrophilic liquid could not wet all the way through the cavities given that there must have air/vapor being trapped inside the cavities. These cavities trapped with air/vapor in principle could initiate heterogeneous nucleation at a low wall temperature. (2) The curvature at the interfaces between liquid and vapor is reversed at the months of the re-entrant cavities. From the Kelvin's equation, one obtains:

$$P_{ve} = P_{v,sat}(T_l) \exp\left(\frac{\sigma/r_e}{\rho_l RT_l}\right) \quad (6.1)$$

It indicates that the vapor pressure at equilibrium is larger than its saturation pressure at a given temperature. Following the same analysis in Section 2.1, one obtains:

$$T_l - T_{sat}(P_l) = -\frac{2\sigma T_{sat}(P_l)}{\rho_v h_{lv} r_e} \quad (6.2)$$

It indicates that the equilibrium temperature at the interface is smaller than the saturation temperature given that liquid must be sub-cooled to condense the vapor inside the re-entrant cavities. As a result, the trapped air/vapor in the re-entrant cavities could sustain longer without being condensed.

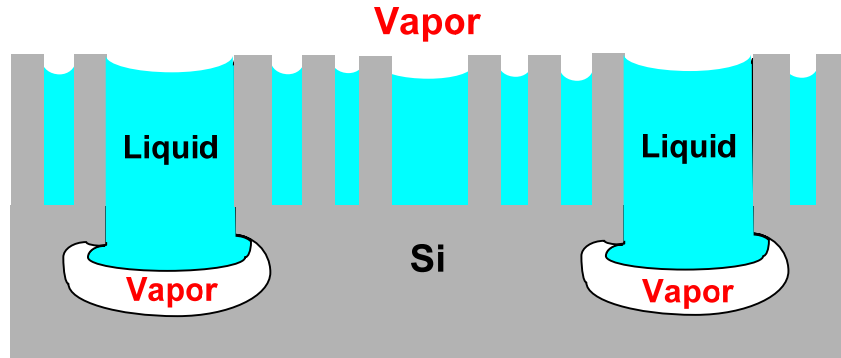


Fig. 6.1 A schematic of a wick with re-entrant cavities

The proposed fabrication procedure of this re-entrant cavities wick is illustrated in Fig. 6.2. The fabrication process is described as follows: (a) Coating a $\sim 1 \mu\text{m}$ thickness layer of thermal oxide on the Si substrate and patterning a layer of PR on top of it (b) Directional etching the oxide layer by plasma etching (c) DRIE the Si substrate to form trenches in the substrate (d) Removing the PR layer (e) Coating another layer of oxide on the substrate for side-wall protecting (f) Directional etching the oxide to expose the bottom layer of oxide (g) Isotropic etching the Si substrate to form re-entrant cavities (h) Removing the oxide layer (i) Coating and patterning another layer of PR (j) DRIE micro pin-fins and microchannels (k) Removing the PR layer. A wick with the re-entrant cavities could be obtained accordingly.

The preliminary result of the fabrication is shown in Fig. 6.3 (a & b) of a top view (Fig. 6.3a) and a cross-sectional view (Fig. 6.3b). The current status of fabrication is at step (h) in Fig. 6.2. As can be seen in Fig. 6.3, we were able to make a perfect re-entrant cavity array with a diameter about $120 \mu\text{m}$. This re-entrant cavity array could be used in pool boiling for enhancing heat transfer coefficient as well.

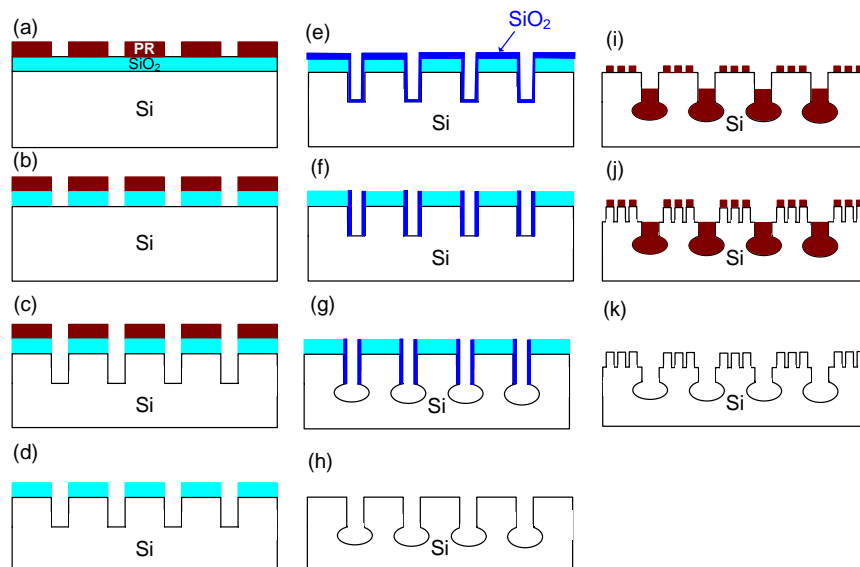


Fig. 6.2 Fabrication procedure for a re-entrant cavity array wick

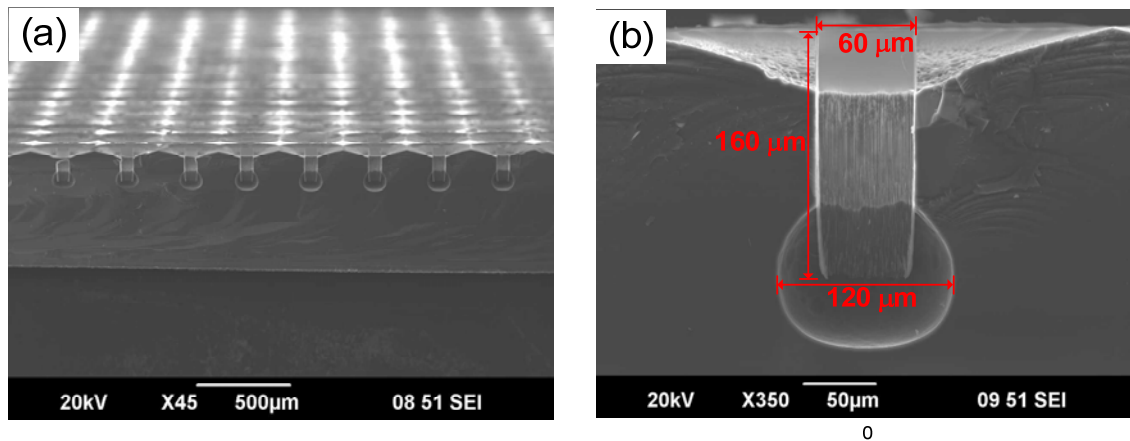


Fig. 6.3 Preliminary result of the fabrication of a re-entrant cavity array wick

6.2.2 Verify the Hydrodynamic Theory

We have studied pool boiling on NW array-coated surfaces and plain Si surfaces. These two kinds of surfaces represent two extremes: The NW array surface exhibits a large capillary force whereas the plain Si surface exhibits no capillary force at all. CHF on SiNW array-coated surfaces and plain Si surfaces are consistent with the predictions of the hydrodynamic theory with a higher nucleation site density is assumed for the SiNW array-coated surfaces. The insight from this study indicates that the CHF is a result of pool hydrodynamics while the surface properties modify the corresponding hydrodynamic limits. This hypothesis can also be supported by that heat transfer coefficient in pool boiling can be generally correlated with a single-phase forced convection process. The extension of the concept of single-phase forced convection to boiling heat transfer suggests that bubble dynamics is the dominant thermal resistance. If the transportation of vapor is not fast enough, thermal energy is accumulated on the substrate. It eventually causes dry-out on the surface, which manifests itself as CHF. To further verify the hypothesis, pool boiling on a microwire array-coated surface, which has a more control of surface morphology compared to NW array-coated surface and a moderate capillary force, will be conducted.

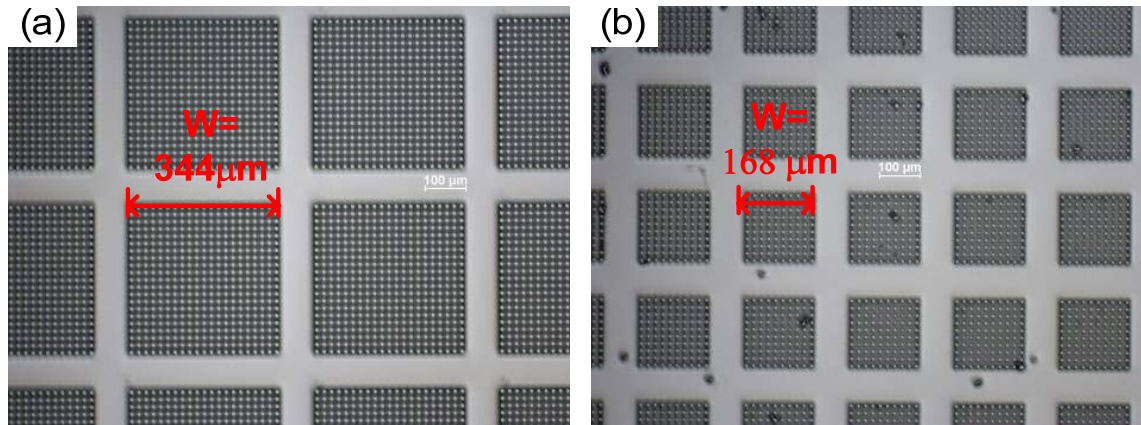


Fig. 6.4 Microwire array with different patch sizes

The SEM images of the microwire array surfaces with two different patch sizes are shown in Fig. 6.4 (a & b). The capillary limit will be first verified by manipulating the patch size and the height of the microwire array. In addition, heater size effect on CHF on the surface will be studied. Fig. 6.5 shows the CHF values of SiNW array-coated surfaces and plain Si surfaces along with the predictions of the hydrodynamic theory on these two kinds of surfaces as well as an expected curve for the values of CHF on microwire array surface. If the CHF data on the microwire array-coated surface could also be matched by the prediction of hydrodynamic theory with an assumed nucleation-site density, it suggests that the proposed CHF model based on the hydrodynamic theory is universally applied and surface properties modify the corresponding hydrodynamic limits.

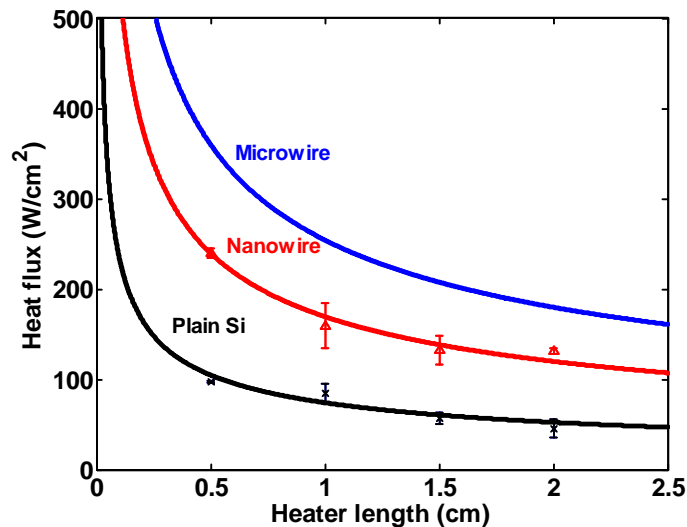


Fig. 6.5 CHF vs. heater size on microwire, nanowire and plain Si surfaces

6.2.3 Comparison of Pool Boiling and Thin Film Boiling

A schematic comparing pool boiling and thin film boiling is shown in Fig. 6.6. In pool boiling the occurrence of CHF could be resulted from pool hydrodynamics whereas there is no such a liquid pool present in a thin film boiling system given that the dry-out is due to the capillary limit in the case of thin film boiling. Comparison of these two could clarify the effect of liquid pool in pool boiling. The values of thermal conductance and dry-out heat flux of pool boiling and thin film boiling, respectively, conducted on the same surface should suggest the effect of liquid pool on CHF and thermal conductance, respectively, in pool boiling.

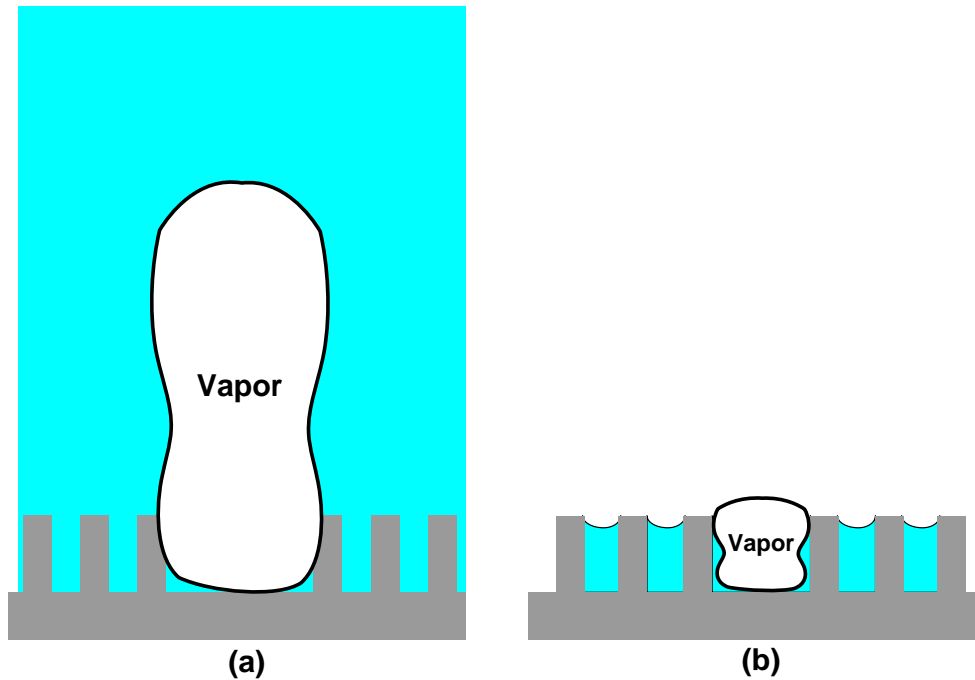


Fig. 6.6 A schematic comparing (a) pool boiling versus (b) thin film boiling

References

- [1] R.E. Smalley, Future global energy prosperity: The terawatt challenge, *Mrs Bull*, 30(6) (2005) 412-417.
- [2] M.G. Kang, Experimental investigation of tube length effect on nucleate pool boiling heat transfer *Annals of Nuclear Energy*, 25(4) (1998) 295-304.
- [3] M. Naitoh, T. Ikeda, K. Nishida, T. Okawa, I. Kataoka, Critical power analysis with mechanistic models for nuclear fuel bundles, (I) Models and verifications for boiling water reactor application, *J Nucl Sci Technol*, 39(1) (2002) 40-52.
- [4] B. Watel, Review of saturated flow boiling in small passages of compact heat-exchangers, *Int J Therm Sci*, 42(2) (2003) 107-140.
- [5] J.R. Thome, Enhanced boiling heat transfer, Hemisphere Pub. Corp., New York, 1990.
- [6] I. Mudawar, Assessment of high-heat-flux thermal management schemes, *Ieee Transactions on Components and Packaging Technologies*, 24(2) (2001) 122-141.
- [7] S.V. Garimella, A.S. Fleischer, J.Y. Murthy, A. Keshavarzi, R. Prasher, C. Patel, S.H. Bhavnani, R. Venkatasubramanian, R. Mahajan, Y. Joshi, B. Sammakia, B.A. Myers, L. Chorosinski, M. Baelmans, P. Sathyamurthy, P.E. Raad, Thermal Challenges in Next-Generation Electronic Systems, *Ieee Transactions on Components and Packaging Technologies*, 31(4) (2008) 801-815.
- [8] R. Mahajan, C.P. Chiu, G. Chrysler, Cooling a microprocessor chip, *P Ieee*, 94(8) (2006) 1476-1486.
- [9] A. Faghri, Heat pipe science and technology, Taylor & Francis, Washington, DC, 1995.
- [10] C.B. Sobhan, R.L. Rag, G.P. Peterson, A review and comparative study of the investigations on micro heat pipes, *Int J Energ Res*, 31(6-7) (2007) 664-688.
- [11] H.B. Ma, K.P. Lofgreen, G.P. Peterson, An experimental investigation of a high flux heat pipe heat sink, *J Electron Packaging*, 128(1) (2006) 18-22.
- [12] A.J. Jiao, H.B. Ma, J.K. Critser, Heat transport characteristics in a miniature flat heat pipe with wire core wicks, *Journal of Heat Transfer*, 130(5) (2008) -.
- [13] A. Gupta, G. Upadhya, Optimization of heat pipe wick structures for low wattage electronics cooling applications, *Advances in Electronic Packaging*, 26 (1999) 2129.
- [14] R.W. Schrage, A theoretical study of interphase mass transfer, Thesis--Columbia University, Columbia University Press, New York, 1953.
- [15] V.K. Dhir, Boiling heat transfer, *Annu Rev Fluid Mech*, 30 (1998) 365-401.

- [16] V.P. Carey, Liquid-vapor phase-change phenomena: an introduction to the thermophysics of vaporization and condensation processes in heat transfer equipment, 2nd ed., Taylor and Francis, New York, 2008.
- [17] N. Zuber, Hydrodynamic Aspects of Boiling Heat Transfer, AECU-4439, 1959.
- [18] J.H. Lienhard, V.K. Dhir, Hydrodynamic Theory of The Peak and Minimum Pool Boiling Heat Fluxes, CR-2270, 1973.
- [19] I.I. Gogonin, S.S. Kutateladze, Critical Heat Flux as a Function of Heater Size for a Liquid Boiling in a Large Enclosure, Journal of Engineering Physics, 33 (1977) 1286-1289.
- [20] V.K. Dhir, S.P. Liaw, Framework for a Unified Model for Nucleate and Transition Pool Boiling, Journal of Heat Transfer, 111 (1989) 739-747.
- [21] C.H. Wang, V.K. Dhir, Effect of Surface Wettability on Active Nucleation Site Density during Pool Boiling of Water on a Vertical Surface, Journal of Heat Transfer, 115(3) (1993) 659-669.
- [22] Y. Takata, S. Hidaka, M. Masuda, T. Ito, Pool boiling on a superhydrophilic surface, Int J Energ Res, 27(2) (2003) 111-119.
- [23] S.M. You, J.H. Kim, K.H. Kim, Effect of nanoparticles on critical heat flux of water in pool boiling heat transfer, Applied Physics Letters, 83(16) (2003) 3374-3376.
- [24] S.J. Kim, I.C. Bang, J. Buongiorno, L.W. Hu, Effects of nanoparticle deposition on surface wettability influencing boiling heat transfer in nanofluids, Applied Physics Letters, 89(15) (2006) 014104-014101~014104-014103.
- [25] S.J. Kim, I.C. Bang, J. Buongiorno, L.W. Hu, Surface wettability change during pool boiling of nanofluids and its effect on critical heat flux, International Journal of Heat and Mass Transfer, 50(19-20) (2007) 4105-4116.
- [26] S.J. Kim, I.C. Bang, J. Buongiorno, L.W. Hu, Study of pool boiling and critical heat flux enhancement in nanofluids, Bulletin of the Polish Academy of Sciences-Technical Sciences, 55(2) (2007) 211-216.
- [27] H.D. Kim, M.H. Kim, Effect of nanoparticle deposition on capillary wicking that influences the critical heat flux in nanofluids, Applied Physics Letters, 91(1) (2007) 014104-014101~014104-014103.
- [28] S.G. Liter, M. Kaviany, Pool-boiling CHF enhancement by modulated porous-layer coating: theory and experiment, International Journal of Heat and Mass Transfer, 44(22) (2001) 4287-4311.
- [29] C. Li, G.P. Peterson, Parametric study of pool boiling on horizontal highly conductive microporous coated surfaces, Journal of Heat Transfer, 129(11) (2007) 1465-1475.

- [30] J.Y. Chang, S.M. You, Boiling heat transfer phenomena from microporous and porous surfaces in saturated FC-72, *International Journal of Heat and Mass Transfer*, 40(18) (1997) 4437-4447.
- [31] T.G. Theofanous, T.N. Dinh, J.P. Tu, A.T. Dinh, The boiling crisis phenomenon - Part II: dryout dynamics and burnout, *Experimental Thermal and Fluid Science*, 26(6-7) (2002) 793-810.
- [32] H. Honda, H. Takamastu, J.J. Wei, Enhanced boiling of FC-72 on silicon chips with micro-pin-fins and submicron-scale roughness, *Journal of Heat Transfer*, 124(2) (2002) 383-390.
- [33] J.J. Wei, H. Honda, Effects of fin geometry on boiling heat transfer from silicon chips with micro-pin-fins immersed in FC-72, *International Journal of Heat and Mass Transfer*, 46(21) (2003) 4059-4070.
- [34] H. Honda, J.J. Wei, Enhanced boiling heat transfer from electronic components by use of surface microstructures, *Experimental Thermal and Fluid Science*, 28(2-3) (2004) 159-169.
- [35] M. Arik, A. Bar-Cohen, Effusivity-based correlation of surface property effects in pool boiling CHF of dielectric liquids, *International Journal of Heat and Mass Transfer*, 46(20) (2003) 3755-3764.
- [36] A. Bar-Cohen, A. McNeil, Parametric Effects of Pool Boiling Critical Heat Flux in Dielectric Liquids, in: *ASME Pool and External Flow Boiling*, 1992, pp. 171-175.
- [37] J.R. Saylor, An experimental study of the size effect in pool boiling CHF on square surfaces, University of Minnesota, Minneapolis, 1989.
- [38] I.L. Pioro, W. Rohsenow, S.S. Doerffer, Nucleate pool-boiling heat transfer. I: review of parametric effects of boiling surface, *International Journal of Heat and Mass Transfer*, 47(23) (2004) 5033-5044.
- [39] S.G. Kandlikar, A theoretical model to predict pool boiling CHF incorporating effects of contact angle and orientation, *Journal of Heat Transfer*, 123(6) (2001) 1071-1079.
- [40] T.G. Theofanous, J.P. Tu, A.T. Dinh, T.N. Dinh, The boiling crisis phenomenon - Part I: nucleation and nucleate boiling heat transfer, *Experimental Thermal and Fluid Science*, 26(6-7) (2002) 775-792.
- [41] C. Li, Z. Wang, P.I. Wang, Y. Peles, N. Koratkar, G.P. Peterson, Nanostructured copper interfaces for enhanced boiling, *Small*, 4(8) (2008) 1084-1088.
- [42] International technology roadmap of semiconductor 2008 in.
- [43] R.S. Prasher, A simplified conduction based modeling scheme for design sensitivity study of thermal solution utilizing heat pipe and vapor chamber technology, *J Electron Packaging*, 125(3) (2003) 378-385.

- [44] R.K. Kirschman, Low-Temperature Electronics, *Ieee Circuit Devic*, 6(2) (1990) 12-24.
- [45] T.W. Davis, S.V. Garimella, Thermal resistance measurement across a wick structure using a novel thermosyphon test chamber, *Exp Heat Transfer*, 21(2) (2008) 143-154.
- [46] C. Li, G.P. Peterson, Y.X. Wang, Evaporation/boiling in thin capillary wicks (I) - Wick thickness effects, *Journal of Heat Transfer*, 128(12) (2006) 1312-1319.
- [47] X.L. Cao, P. Cheng, T.S. Zhao, Experimental study of evaporative heat transfer in sintered copper bidispersed wick structures, *J Thermophys Heat Tr*, 16(4) (2002) 547-552.
- [48] T. Semenic, Y.Y. Lin, I. Catton, D.B. Sarraf, Use of biporous wicks to remove high heat fluxes, *Appl Therm Eng*, 28(4) (2008) 278-283.
- [49] T. Semenic, Y.Y. Lin, I. Catton, Thermophysical properties of biporous heat pipe evaporators, *Journal of Heat Transfer*, 130(2) (2008) -.
- [50] Y. Zhao, C. Chen, Vaporization heat transfer in sintered copper wicks with micro-grooves in heat pipe evaporators, in: *THERMES: Thermal Challenges in Next Generation Electronic Systems*, S.V. Garimella and A.S. Fleischer (eds), Millpress, Rotterdam, 2007, pp. 241-247.
- [51] W. Thomson, LX. On the equilibrium of vapour at a curved surface of liquid, *Philosophical Magazine Series*, 4(42) (1871) 448-452.
- [52] Y.Y. Hsu, On the size range of active nucleation cavities on a heating surface, *Journal of Heat Transfer*, 84 (1962) 207-216.
- [53] W.M. Rohsenow, A method of correlating heat transfer data for surface boiling of liquids, *Trans. ASME*, 74 (1952) 969-975.
- [54] H.K. Forster, R. Greif, Heat Transfer to a Boiling-liquid Mechanism and Correlation, *Journal of Heat Transfer*, 81 (1959) 45.
- [55] H.K. Forster, N. Zuber, Dynamics of Vapor Bubbles and Boiling Heat Transfer, *Aiche J*, 1(4) (1955) 531-535.
- [56] R.I. Vachon, G.H. Nix, G.E. Tanger, Evaluation of Constants for Rohsenow Pool-Boiling Correlation, *Journal of Heat Transfer*, 90(2) (1968) 239-&.
- [57] W.M. Rohsenow, J.A. Clarke, Heat Transfer and Pressure Drop Data for High Heat Flux Densities to Water at High Subcritical Pressures, in: *Heat Transfer and Fluid Mechanics Institute*, Stanford University Press, Stanford, 1951, pp. 193.
- [58] F. Kreith, M. Sommerfield, Heat Transfer to Water at High Flux Densities With and Without Surface Boiling, *Trans. ASME*, 71 (1949) 805-815.
- [59] E.L. Piret, H.S. Isbin, Two-phase Heat Transfer in Natural Circulation Evaporators, *Chemical Engineering Progress Symposium Series*, 50(6) (1953) 305.

- [60] A.E. Bergles, W.M. Rohsenow, The determination of forced-convection surface-boiling heat transfer, *Journal of Heat Transfer*, 86 (1964) 365-372.
- [61] V.M. Borishansky, Correlation of the effect of pressure on critical heat flux and heat transfer rates using theory of thermodynamic similarity, in: *Problems of Heat Transfer and Hydraulics of Two-Phase Media*, Pergamon Press, 1969, pp. 16-37.
- [62] I.L. Mostinski, Application of the Rule of Corresponding States for the Calculation of Heat Transfer and Critical Heat Flux, *Teploenergetika*, 4 (1963) 66.
- [63] K. Stephan, M. Abdelsalam, Heat-Transfer Correlations for Natural-Convection Boiling, *International Journal of Heat and Mass Transfer*, 23(1) (1980) 73-87.
- [64] V.P. Carey, Liquid-vapor phase-change phenomena: an introduction to the thermophysics of vaporization and condensation processes in heat transfer equipment, in, Taylor and Francis, New York, 2008, pp. 280-281.
- [65] A.J. Fowler, A. Bejan, Forced-Convection in Banks of Inclined Cylinders at Low Reynolds-Numbers, *Int J Heat Fluid Fl*, 15(2) (1994) 90-99.
- [66] G. Birkhoff, Helmholtz and Taylor Instability, in: *Proceedings of Symposia in Applied Mathematics*, 1962, pp. 55-76.
- [67] B.H. Kim, G.P. Peterson, Analysis of the Critical Weber Number at the Onset of Liquid Entrainment in Capillary-Driven Heat Pipes, *International Journal of Heat and Mass Transfer*, 38(8) (1995) 1427-1442.
- [68] N.A. Gumerov, C.-T. Hsiao, A.G. Goumilevski, Determination of the Accommodation Coefficient Using Vapor/Gas Bubble Dynamics in an Acoustic Field, NASA/CR—2001-210572, 2001.
- [69] J.W.S. Rayleigh, On the instability of jets, in: *Proceedings of the London Mathematical Society*, 1879, pp. 4–13.
- [70] D.H. Sharp, An Overview of Rayleigh-Taylor Instability, *Physica D*, 12 (1984) 3-10.
- [71] S.S. Kutateladze, A Hydrodynamic Theory of Changes in a Boiling Process Under Free Convection, in: *Izvestia Akademia Nauk, S.S.S.R., Otdelenie Tekhnicheskii Nauk*, , 1951, pp. 529.
- [72] H.M. Kurihara, J.E. Myers, The Effects of Superheat and Surface Roughness on Boiling Coefficients, *Aiche J*, 6(1) (1960) 83-91.
- [73] Y. Haramura, Y. Katto, A New Hydrodynamic Model of Critical Heat-Flux, Applicable Widely to Both Pool and Forced-Convection Boiling on Submerged Bodies in Saturated Liquids, *International Journal of Heat and Mass Transfer*, 26(3) (1983) 389-399.

- [74] C. Unal, V. Daw, R.A. Nelson, Unifying the Controlling Mechanisms for the Critical Heat-Flux and Quenching - the Ability of Liquid to Contact the Hot Surface, *Journal of Heat Transfer*, 114(4) (1992) 972-982.
- [75] K.A. Park, A.E. Bergles, Effects of Size of Simulated Microelectronic Chips on Boiling and Critical Heat-Flux, *Journal of Heat Transfer*, 110(3) (1988) 728-734.
- [76] K.N. Rainey, S.M. You, Effects of heater size and orientation on pool boiling heat transfer from microporous coated surfaces, *International Journal of Heat and Mass Transfer*, 44(14) (2001) 2589-2599.
- [77] J.K. Yuan, X.G. Liu, O. Akbulut, J.Q. Hu, S.L. Suib, J. Kong, F. Stellacci, Superwetting nanowire membranes for selective absorption, *Nat Nanotechnol*, 3(6) (2008) 332-336.
- [78] A.I. Hochbaum, R.K. Chen, R.D. Delgado, W.J. Liang, E.C. Garnett, M. Najarian, A. Majumdar, P.D. Yang, Enhanced thermoelectric performance of rough silicon nanowires, *Nature*, 451(7175) (2008) 163-U165.
- [79] M.A. Hanlon, H.B. Ma, Evaporation heat transfer in sintered porous media, *Journal of Heat Transfer*, 125(4) (2003) 644-652.
- [80] D. Khrustalev, A. Faghri, Heat-Transfer during Evaporation on Capillary-Grooved Structures of Heat Pipes, *Journal of Heat Transfer*, 117(3) (1995) 740-747.
- [81] P.C. Stephan, C.A. Busse, Analysis of the Heat-Transfer Coefficient of Grooved Heat Pipe Evaporator Walls, *International Journal of Heat and Mass Transfer*, 35(2) (1992) 383-391.
- [82] X. Xu, V.P. Carey, Film evaporation from a micro-grooved surface — An approximate heat transfer model and its comparison with experimental data, *J Thermophys Heat Tr*, 4(4) (1990) 512.
- [83] J.N. Israelachvili, *Intermolecular and surface forces*, 2nd ed., Academic Press, San Diego, 1992.
- [84] M. Potash, P.C. Wayner, Evaporation from a 2-Dimensional Extended Meniscus, *International Journal of Heat and Mass Transfer*, 15(10) (1972) 1851-&.
- [85] P.C. Wayner, The Effect of Interfacial Mass-Transport on Flow in Thin Liquid-Films, *Colloid Surface*, 52(1-2) (1991) 71-84.
- [86] P.C. Wayner, Intermolecular forces in phase-change heat transfer: 1998 Kern award review, *Aiche J*, 45(10) (1999) 2055-2068.
- [87] H. Wang, S.V. Garimella, J.Y. Murthy, Characteristics of an evaporating thin film in a microchannel, *International Journal of Heat and Mass Transfer*, 50(19-20) (2007) 3933-3942.
- [88] S.J.S. Morris, The evaporating meniscus in a channel, *J Fluid Mech*, 494 (2003) 297-317.

[89] S.S. Panchamgam, J.L. Plawsky, P.C. Wayner, Spreading characteristics and microscale evaporative heat transfer in an ultrathin film containing a binary mixture, *Journal of Heat Transfer*, 128(12) (2006) 1266-1275.

[90] H.W. Coleman, W.G. Steele, *Experimentation and uncertainty analysis for engineers*, Wiley, New York, 1989.

Appendix: Heat Loss Estimate for the Evaporation Experiment

Table A.1 Conduction Loss of the Evaporation Experiment

Heat Flux (W/cm ²)	Heat Loss (W)	Cond. Loss (%)
55.3	5.13	9.3
76.8	6.3	8.2
99.4	7.75	7.8
130.3	9.86	7.6
152.3	11.41	7.5
175.6	10.22	5.8
196.1	10.94	9.2
228.9	12.02	5.3

The conduction loss of the applied heat fluxes was estimated by Eq. (4.11). The result of the conduction loss for the sample having the parameters ($d = 32 \mu\text{m}$, $D = 60 \mu\text{m}$, $H = 150 \mu\text{m}$, $L = 308 \mu\text{m}$, see Table 5.1) is shown in the Table A.1. At a peak heat flux of about 200 W/cm^2 , the conduction loss is about 10 % of the applied heat flux.

Appendix: Uncertainty Analysis

Uncertainty estimates of various quantities derived in the data reduction process are obtained using the idea of relative error [90]. If a quantity F depends on other quantities A , B , C in the following way:

$$F = F(A, B, C) \tag{A.1}$$

then the uncertainty δF is related to the uncertainties $\delta A/A$, $\delta B/B$, $\delta C/C$ by

$$\delta F = \sqrt{\left(\frac{\partial F}{\partial A} \delta A\right)^2 + \left(\frac{\partial F}{\partial B} \delta B\right)^2 + \left(\frac{\partial F}{\partial C} \delta C\right)^2} \tag{A.2}$$

For the particular case where the relation is assumed to be a power law, such as

$$F = AB^2 / C^m \quad (\text{A.3})$$

then the relative uncertainty $\delta F/F$ is given by

$$\frac{\delta F}{F} = \sqrt{\left(\frac{\delta A}{A}\right)^2 + \left(\frac{2\delta B}{B}\right)^2 + \left(\frac{m\delta C}{C}\right)^2} \quad (\text{A.4})$$

Using this idea, the uncertainty in the heat flux and heat transfer coefficient can be obtained.

Uncertainty in Heat Flux Measurement

In Chapter 4 and Chapter 5, the heat flux was calculated as $q'' = \frac{VI}{A}$, where V and I are measured voltage and current across the ITO heater, respectively, and A is the area of the heater. The measured accuracy of the voltage and current of the power supply (Agilent N5750A) are $0.1\% \pm 150$ mV and $0.1\% \pm 15$ mA, respectively. The uncertainties of the area measurement in the thin film evaporation/boiling are assumed as 5%. As an example, the uncertainty of the dry-out heat flux of 228.85 W/cm² of the wick having the parameters ($d = 32$ μ m, $D = 60$ μ m, $H = 150$ μ m, $L = 308$ μ m, see Table 5.1) with an applied voltage of 45 V, an applied current of 2.2 A and a heater area of 1 cm² is

$$\frac{\delta q''}{q''} = \sqrt{\left(\frac{\delta V}{V}\right)^2 + \left(\frac{\delta I}{I}\right)^2 + \left(\frac{\delta A}{A}\right)^2} = 5.1\% \quad (\text{A.5})$$

On the other hand, since the heater area of the modified test section of the pool boiling experiments is defined by photo-lithography, a correspondingly lower uncertainty of the heater area of 1% is assumed. As an example, the relative uncertainty ($\delta q''/q''$) of the CHF of 224 W/cm² of the heater with an area of 0.5 x 0.5 cm² (see Fig. 4.14) having an applied voltage of 40.8 V, an applied current of 1.51 A due to the system uncertainty (Eq. (A.5)) is 1.6%. The overall relative uncertainty of the CHF is the RMS value of the system uncertainty and the uncertainty of data repeatability as shown:

$$\frac{\delta q''}{q''} \Big|_{\text{overall}} = \sqrt{\left(\frac{\delta q''}{q''} \Big|_{\text{system}}\right)^2 + \left(\frac{\delta q''}{q''} \Big|_{\text{repeatability}}\right)^2} = 2.9\% \quad (\text{A.6})$$

where $\frac{\delta q''}{q''} \Big|_{\text{repeatability}}$ is equal to 2.5%.

Uncertainty in Temperature Measurement

The actual wall temperature is derived as $T_w = T_{TC} - q''/(k_{si}/\delta)$, where q'' , T_{TC} , k_{si} and δ are the applied heat flux, temperature measured by the thermocouple, thermal conductivity of Si substrate and the thickness of the substrate, respectively. The uncertainty of the temperature measured by the thermocouple (T_{TC}) was equal to the summation of the uncertainties due to the estimated thickness of the epoxy layer, the uncertainty of the T type thermocouple (Omega Engineering Inc.) and the accuracy of the data acquisition system (Agilent 34970A). Assuming an uncertainty of the thickness of the epoxy layer of 5 μm , the uncertainty of the temperature measured by the thermocouple due to the estimated thickness of the epoxy layer under 224 W/cm^2 heat flux (as in the case of CHF in pool boiling with a heater size of 0.5 x 0.5 cm^2 and assuming a 1.5 % of the applied power is lost through the back side of the test section) is equal to 0.084 $^\circ\text{C}$ ($k = 2.02 \text{ W}/\text{m}\cdot\text{K}$). The uncertainty in the absolute temperature measurement of the thermocouple is 0.5 $^\circ\text{C}$. In addition, the accuracy of the thermocouple reading of the data acquisition system (Agilent 34970A) is 1 $^\circ\text{C}$. Therefore, the overall uncertainty of the temperature measurement by the thermocouple (T_{TC}) is about 1.584 $^\circ\text{C}$. The relative uncertainty of actual wall temperature ($\delta T_w/T_w$) is then obtained as:

$$\frac{\delta T_w}{T_w} = \sqrt{\left(\frac{\delta q''}{q''}\right)^2 + \left(\frac{\delta T_{TC}}{T_{TC}}\right)^2} = 2.0 \% \quad (\text{A.7})$$

Uncertainty in the Heat Transfer Coefficients of Pool Boiling

The heat transfer coefficient in pool boiling was defined as $h = q''/(T_w - T_{sat})$, where $T_w = T_{TC} - q''/(k_{si}/\delta)$ is the actual wall temperature. The relative uncertainty of the heat transfer coefficient ($\delta h/h$) for the CHF of 224 W/cm^2 is obtained as:

$$\frac{\delta h}{h} = \sqrt{\left(\frac{\delta q''}{q''}\right)^2 + \left(\frac{\delta T_w}{T_w}\right)^2} = 2.5 \% \quad (\text{A.8})$$

Uncertainty in the Thermal Conductances of Evaporative Heat Transfer

The thermal conductance of a wick (Chapter 5) is defined by the slopes of the curves. The linear least-square curve fits have been made for the experimental data to estimate the thermal conductance of the evaporative heat transfer. The standard error (standard deviation) for a slope of a linear least square curve fit is [90]:

$$S_m = \left(\frac{S_y^2}{S_{xx}}\right)^{1/2} \quad (\text{A.9})$$

where

$$S_Y = \left[\frac{\sum_{i=1}^N (Y_i - mX_i - c)^2}{N - 2} \right]^{1/2} \quad (\text{A.10})$$

$$S_{XX} = \sum_{i=1}^N X_i^2 - \frac{\left(\sum_{i=1}^N X_i \right)^2}{N} \quad (\text{A.11})$$

The m and c in Eq. (A.9) are the slope and the constant of the linear square fit curve. N is the number of points and X_i and Y_i are the actual data of temperature and heat flux, respectively. As an example, the stand error (S_m) of the conductance of 16.28 W/cm²-K (defined by the slope, see Fig. 5.16 and Table 5.2) of the sample having the parameters ($d = 32 \mu\text{m}$, $D = 60 \mu\text{m}$, $H = 150 \mu\text{m}$, $L = 308 \mu\text{m}$, see Table 5.1) is estimated as $S_m = 1.33$ using Eqs. (A.9 – A.11).